UNIVERSITY OF SOUTHAMPTON

An Observational Study of Cataclysmic Variable Evolution

Sofía Araujo-Betancor

Submitted for the degree of Doctor of Philosophy

SCHOOL OF PHYSICS AND ASTRONOMY
FACULTY OF SCIENCE

March 15, 2004

UNIVERSITY OF SOUTHAMPTON

ABSTRACT

FACULTY OF SCIENCE

SCHOOL OF PHYSICS AND ASTRONOMY

Doctor of Philosophy

An Observational Study of Cataclysmic Variable Evolution

by Sofía Araujo-Betancor

In this thesis I present an observational study of the evolution of Cataclysmic Variables (CVs). Disrupted magnetic braking has been the standard paradigm of CV evolution for the past twenty years. Unfortunately, some of its predictions are in strong disagreement with the observations. In recent years, a number of additions/alternatives to the standard model have been proposed. Yet, none have been able to explain all of the features observed in the currently known CV population. The work presented in this thesis is based mainly on a large-scale search for CVs. The primary aim of this project is to resolve the disagreement between theory and observations by eliminating the observational biases of the present CV sample. Here I use two complementary approaches to search for CVs: (1) from the spectroscopic appearance in the Hamburg Quasar Survey (HQS) and (2) by using a combination of X-ray emission and multi-colour selection criteria in the ROSAT and 2MASS archival data. So far, we have discovered 52 new CVs in the HQS and 11 new CVs (the majority of them magnetic) and one pre-CV in the ROSAT/2MASS. Follow-up observations of two newly discovered HQS CVs, 1RXS J062518.2+733433 and HS 2331+3905, resulted in the classification of the first as an Intermediate Polar, with $P_{\rm orb} = 283.0\,{\rm min}$ and $P_{\rm spin} = 19.8\,{\rm min}$, and the second as a short orbital period system, $P_{\rm orb} = 81.0\,{\rm min}$, harboring a white dwarf pulsator. In addition, we found that the dominant $\sim 3.5\,{\rm h}$ radial velocity variation of HS 2331+3905, does not correspond to the orbital period of the system, contrary to all other CVs. Despite its novel selection criterion, the HQS does not provide many short-period CVs – even though tests with the known CVs included in the survey have shown that it is very sensitive to those objects. The biggest surprise in the new HQS CV sample is the discovery of many new SW Sex stars. The clustering of SW Sex stars in the 3-4 h period range is probably an important feature in

the evolution of CVs that we currently do not understand at all. To improve our chances of understanding what is going on in that period range, we need accurate system parameters for these stars, which is difficult mainly because of their defining characteristics. I have used HST data of one of the sporadic low states of the SW Sex star, DW UMa, to derive its systems parameters. The success of this study is the first step towards the otherwise impossible task of compiling reliable system parameters for the SW Sex stars.

Contents

List of Figures

List of Tables

Declaration

I, Sofía Araujo-Betancor, declare that this thesis consists of work carried out by myself at the University of Southampton whilst in registered postgraduate candidature. None of the content has been previously submitted to the board for the candidature.

Acknowledgments

I first of all want to thank my two supervisors, Christian Knigge and Boris Gänsicke for the great job they have done in guiding me throughout my PhD. I appreciate their patience and their willingness to answer even the most stupid questions. I am especially in debt for the extra-effort they both made in quickly reading and commenting a progress draft of this thesis in spite of their tight schedules. I am forever grateful to Boris Gänsicke for introducing me to the world of CV evolution, getting me motivated by stimulating discussions. His unconditional help has made all the difference.

The list of people who has contributed one way or another to the work presented in this thesis is very long, so I apologize in advance to those whose names I do not mention in what follows. Special gratitude goes to Pablo Rodríguez-Gil, Luisa Morales and Tom Marsh for helping out with all sort of astrophysical related problems. I also like to thank Tom Marsh for providing the ULTRACAM data of HS 2331, and his set of data reduction/analysis software. Deep thanks goes to Rob Hynes and Danny Steeghs for putting out with me during the long observing nights at La Palma. I particularly enjoyed the ROSAT/2MASS observing campaign for finding new CVs, that was great fun and hard-core astronomy. I am grateful to John Thorstensen for providing the last set of spectra of HS 2331, and Robert Fried for all the photometry obtained from the Braeside observatory. I would like to thank Dimitris Mislis and Christos Papadimitriou for helping out during my observations at the Kryoneri Observatory in Greece. I have Phil Uttley to thank for bringing discussions about philosophy and politics to the office which made my PhD that bit more interesting.

On the personal note I would like to thank my best friend and companion in life Carlos. His way of seeing life inspires me even today, after so many years together. I would like to thank my family and friends for supporting this mad idea of being an astronomer.

I finally like to dedicate this thesis to the memory of my parents and my uncle.

Chapter 1

Introduction

1.1 Motivation

Accretion is an extremely common phenomenon occurring throughout the Universe, from giving birth to solar systems like ours to fuelling the nuclei of the active Galaxies. Despite its importance, our knowledge of the physical processes driving accretion is quite limited. Among the objects undergoing accretion there is a group of close binary systems called Cataclysmic Variables (CVs) whose characteristics make them the best suited laboratories for the study of accretion physics: the binary components are in general well understood; many of these systems can be found relatively nearby (a few hundred parsecs away); they orbit around their centre of mass on timescales ranging from a few days to a few minutes, making accretion-related variability studies much more accessible to observations than in any other type of objects.

1.1.1 Cataclysmic variables

CVs are also interesting objects to study in their own right. Most of the normal stars we see are part of a binary system. Those in which the stellar components are close together (i.e. having orbital periods of less than a few days) comprise the most exotic objects of them all. Their behaviour mainly depends on the combination of stellar components they harbour: from low mass X-ray binaries (LMXBs) made up of a neutron star (or a black hole) as the compact star with a late-type main sequence companion, to systems in which both stellar components are white dwarfs, neutron stars or even a mixture of the two. CVs belong to the population of semi-detached close binary systems containing a white dwarf as the compact star and a late-type main-sequence star or brown dwarf as the donor companion (see Patterson 1984; Smith & Dhillon 1998). The white dwarf is feeding on material lost by the donor star either via an accretion disc (if the white dwarf has a weak or no magnetic field Fig. 1.1a) or along the magnetic field lines of the white dwarf (if the magnetic field is strong enough; Fig. 1.1b) or in some cases using a mixture of the two. CVs are named after the most obvious behaviour they display: outbursts. But not all CVs exhibit outbursts. In fact some never do and are persistently found in a bright (high) state, while others show low states instead. These low states have been observed in polars (CVs containing a white dwarf with a magnetic field strong enough to prevent the formation of a disc) and nova-like variables (high mass transfer rate CVs) and are directly related to variations in the mass loss rate from the donor star (King & Cannizzo 1998). I will discuss the different types of CVs in Sec. 1.3. Within the CV population there is a large variety of species which can be characterized by the knowledge of the orbital period ($P_{\rm orb}$), the accretion mass rate ($\dot{M}$), and the magnetic field strength of the white dwarf (B). The different possible combinations of these three parameters can explain the whole range of behaviours seen in CVs. From the relatively quiet polars to the explosive classical novae. Even one of the most violent astrophysical phenomenon, supernovae type Ia, maybe be related to CVs within a certain range of $P_{\rm orb}$, $\dot{M}$ and B. This type of supernova is used

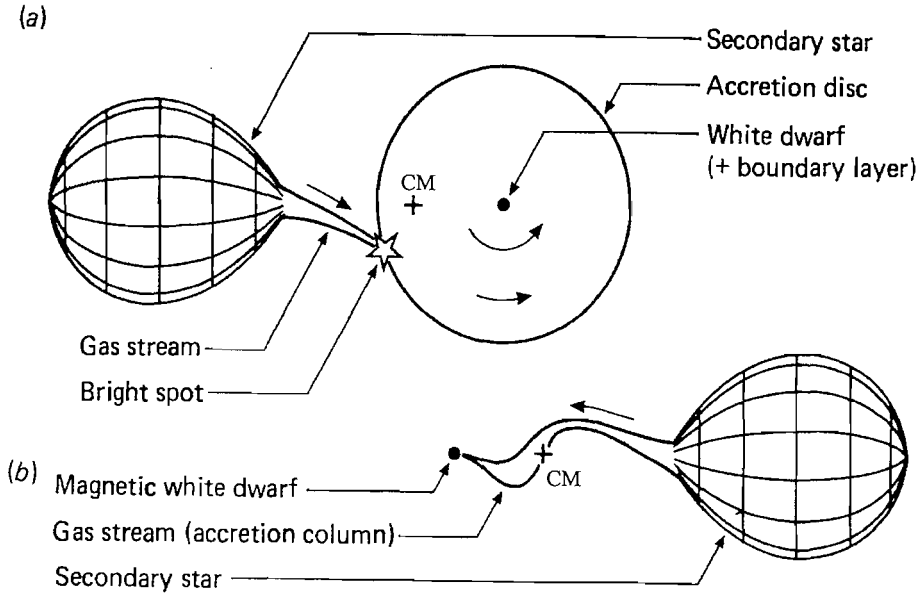

Figure 1.1: Illustration of the constituents of the two main types of CVs. (a) The white dwarf magnetic field is not strong enough to interfere with the mass transfer from the secondary and a disc is formed. The point of impact between the stream of material and the outer edge of the disc is the bright spot. (b) The magnetic field of the white dwarf is strong enough to prohibit the formation of a disc. The stream is instead channelled along the magnetic field lines to the surface of the white dwarf. In both cases, the stars rotate around the centre of mass (CM) of the system. Modified from (Pringle & Wade 1985).

to estimate the distance to remote galaxies which enables cosmological studies on the evolution of the Universe as a whole. Most importantly, supernova explosions trigger stellar formation and seed the Universe with the heavy elements which enable terrestrial planets, and subsequently life, to exist. It is therefore extremely important to understand how CVs (and close binaries in general) are formed, how they live and how they finally die, as a precursor to understand more fundamental questions.

The work presented here is focused on CVs and is aimed at a better understanding of their evolution. Specifically, I use spectroscopic and photometric observations of newly discovered CVs in order to address the current disagreement between the theory of CV

evolution and observations. The only previously known CV in my study is DW UMa, which belongs to a rather peculiar subgroup of CVs (the SW Sextantis stars). Understanding why these CVs behave so differently deserves some special attention when one embarks on a study of CV evolution. In the remainder of this Chapter I describe the structure and properties of CVs and the defining characteristics of the different classes.

1.2 Mass transfer

Continuous mass transfer in CVs (and in close binaries in general) is achieved by material overflowing the secondary's Roche lobe. In most CVs, mass is transferred from the less massive donor onto the more massive accretor, i.e. the white dwarf[1]. In this configuration, the conservation of angular momentum will cause the mass transfer to widen the binary orbit, and, consequently, will result in the donor star detaching from its Roche lobe. That is because mass is transferred closer to the center of mass of the system, losing angular momentum, and so the system increases the orbital separation to compensate. To keep mass transfer alive there are two possibilities: angular momentum losses from the system shrink the orbit of the binary enough so that the secondary is kept in contact with its Roche lobe (typical picture for CVs); the other possibility is the expansion of the secondary as a direct consequence of its nuclear evolution. However, the latter does not apply to most CVs since they contain secondary stars of less than a solar mass. Stars with such low masses have lifetimes too long to undergo significant nuclear evolution in a Hubble time (i.e. the age of the Universe).

[1]The opposite case, namely the heavier star is the donor and the lighter companion is the receiver, is dynamically unstable. Refer to Sec. 1.2.1 for a full explanation.

1.2.1 Roche lobe overflow

The Roche lobe model for CVs was put forward by Crawford & Kraft (1956) in their study of AE Aqr, where they first proposed the picture of a late-type star filling its Roche lobe by transferring mass to the primary star. The donor star has two timescales on which to respond to mass loss: the dynamical timescale ($\sim$ hours) on which the star adjusts itself to hydrostatic equilibrium and the thermal or Kelvin-Helmholtz timescale ($\sim 10^8$ yr) on which the star adjusts itself to thermal equilibrium. In a typical CV, dynamically stable mass transfer can occur over long time scales as long as the donor star is less massive than the white dwarf. Due to the constraint on the masses of both stellar components. i.e. $M_2 < M_1 < M_{\rm Chandrasekhar}$, the companions in CVs should be low mass late-type stars of type K, M or brown dwarfs.

The total potential within the binary due to the gravitational forces of the two stars and to the centrifugal force (from the circular motion of the system) defines the volume of influence of the two stellar components. Figure 1.2 illustrates a cross section of the gravitational potential field in the orbital plane of a binary system with a mass ratio of 0.3, i.e. $q = M_2/M_1 = 0.3$, where M_1 is the mass of the primary (white dwarf) and M_2 is the mass of the secondary (main-sequence star). The critical surface within which material is bound to either one or the other star defines the Roche lobes which are shown in bold, touching at the inner Lagrangian point, L_1. In the Lagrangian points L_1 to L_5 all existing forces within the system cancel each other, (i.e. $\partial\Phi/\partial x = 0$; Φ is the total potential and x is the spatial direction in the line joining the centers of the two stars). Matter from the Roche-lobe-filling secondary escapes through L_1 because it is a saddle point of the Roche lobe equipotential surface, so it is easier to go through L_1 than to escape the critical surface altogether. One immediate consequence of the distortion of the secondary (due to tidal interaction with the white dwarf) is that it ends up tidally locked: its spin period matches the orbital motion of the system. A good estimate of the radius of the mass donor, R_2, can be found using Eggleton (1983)'s approximation of the radius of

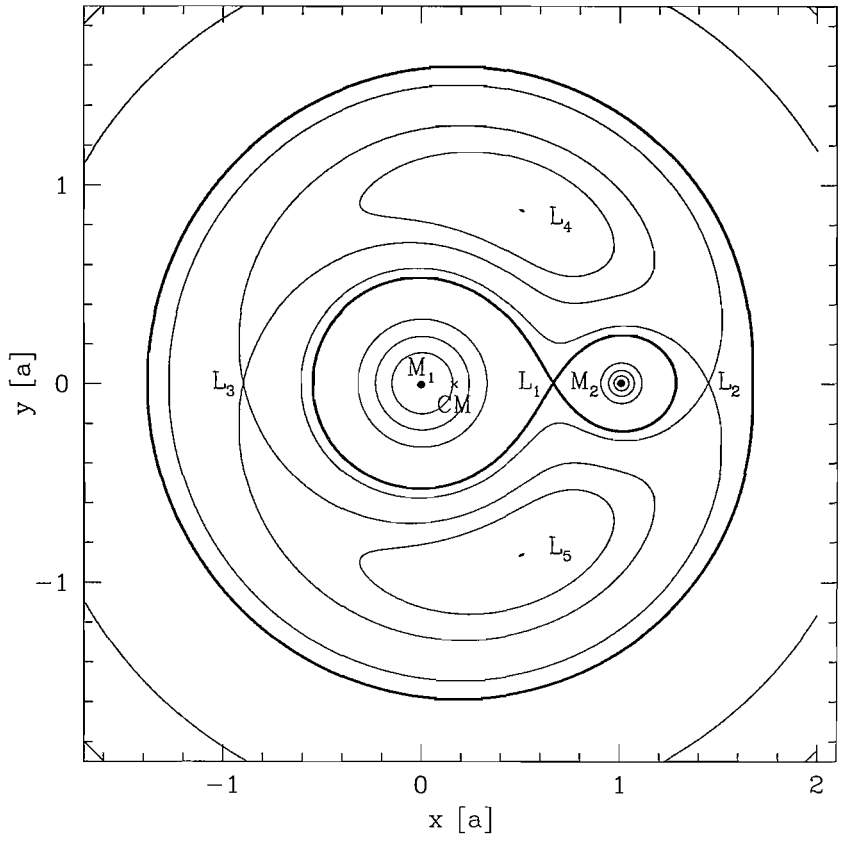

Figure 1.2: Schematic Roche lobe geometry (cross section in the plane of the orbit) and Lagrangian points, L_1, L_2, L_3, L_4 and L_5, for a close binary system of $q = 0.3$. The potential surfaces touching at the L_1 (in bold) are the Roche lobes of the two stars. Both bold contours have the same potential. Provided by B. Gänsicke.

a sphere containing the same volume as the secondary's Roche lobe,

$$\frac{R_2}{a} = \frac{0.49q^{2/3}}{0.6q^{2/3} + \ln(1+q^{1/3})}. \tag{1.1}$$

The binary separation, a, defined as the distance between the centres-of-mass of the two stars (of the order of a few solar radii) can be calculated using Kepler's law,

$$\frac{4\pi^2}{P_{\rm orb}^2} = \frac{G(M_1+M_2)}{a^3} \tag{1.2}$$

$$\text{as} \quad a = 3.53 \times 10^{10} \left(\frac{M_1}{M_\odot}\right)^{1/3} (1+q)^{1/3} P_{\rm orb}({\rm h})^{2/3} \text{ cm}. \tag{1.3}$$

1.2.2 The formation of a disc

The majority of CVs have a weak or no magnetic field on the white dwarf and, as pictured in Fig. 1.1a, accrete through an accretion disc. It is therefore appropriate at this stage to include a more detailed description of the processes involved in disc-accreting systems.

As mentioned in Sec. 1.2.1, material from the donor star is injected through inner Lagrangian point L_1. The injection velocity is a combination of the thermal speed of the gas ($\sim$ 10 km s^{-1}) and the orbital motion of the secondary (more than 100 km s^{-1}). The former is in effect the sound speed in the gas and is directed radially towards the white dwarf, and the latter is pointing parallel to the orbital motion. Since the resultant velocity is very high compared with the sound speed of the gas, the stream swings around the white dwarf in an almost ballistic path. Fig. 1.3 shows an example of what the stream might look like after a few orbital periods of the binary. After hitting itself, the flow of material loses energy and eventually its trajectory settles into the lowest-energy type of orbit: a circular one. However, the angular momentum of the gas around the primary has not changed. The Keplerian velocity of the gas at this so called circularization radius, R_c, is

$$v_k(R_c) = \left(\frac{GM_1}{R_c}\right)^{1/2}$$

The specific angular momentum of the gas at L_1 is $j_{L_1} = R_{L_1}^2\Omega$ and the specific angular momentum at the circularization radius is $j_{R_c} = R_c v_k(R_c)$. Here Ω is the orbital angular velocity of the system and R_{L_1} is the distance from the centre of the primary to L_1 given by the following relations:

$$\frac{R_{L_1}}{a} = 0.5000 - 0.227\log q, \qquad \text{for } 0.1 \leq q \leq 10 \quad \text{(Plavec \& Kratochvil 1964)},$$

or alternatively,

$$\frac{R_{L_1}}{a} = 1 - w + \frac{1}{3}w^2 + \frac{1}{9}w^3, \qquad \text{for } q \leq 0.1 \quad \text{(Kopal 1959)},$$

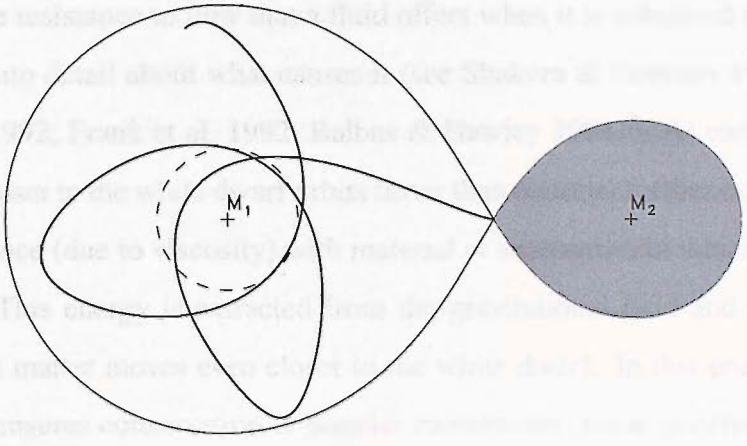

Figure 1.3: Example of the initial stream after a few orbital periods of the binary. Matter flows from the secondary (donor; M_2) to the primary (white dwarf; M_1). The dash circle marks the circularization radius; see text for details. Modified from Hellier (2001).

$$\text{where } w^3 = \frac{q}{3(1+q)}.$$

Equating both, the specific angular momentum of the gas at L_1 and at the circularization radius gives,

$$\frac{R_c}{a} = \left(\frac{R_{L_1}}{a}\right)^4 \frac{4\pi^2 a^3}{GM_1 P_{\rm orb}^2},$$

and eliminating $P_{\rm orb}$ by using Kepler's law (Eqn. 1.2) leads to,

$$\frac{R_c}{a} = \left(\frac{R_{L_1}}{a}\right)^4 (1+q).$$

Since the circular orbit has the lowest energy for a given angular momentum, the gas can only be accreted by the white dwarf if it loses angular momentum. To understand what happens next it is assumed that the disc behaves, in effect, like a fluid with a very high viscosity. A note of caution is needed at this stage: even though it is commonly accepted that viscosity is essential to the operation of an accretion disc, its nature is still very poorly understood and a discussion of it is beyond the scope of this thesis. In the remainder of this section, as well as in the next one, I make use of the physical concept of viscosity (i.e.

a measure of the resistance to flow that a fluid offers when it is subjected to shear stress) without going into detail about what causes it (see Shakura & Sunyaev 1973; Balbus & Hawley 1991, 1992; Frank et al. 1992; Balbus & Hawley 1994)[2]. At each radius in the disc, material closer to the white dwarf orbits faster than material further out, causing friction and turbulence (due to viscosity) with material at adjacent radii which consequently heats the gas. This energy is extracted from the gravitational field and radiated away. This means that matter moves even closer to the white dwarf. In this process, viscosity in the material ensures conservation of angular momentum: some material moves to orbits further out in order for other material to move further in. The result is a disc with material continually flowing through it. At the outer edge of the disc tidal interactions with the secondary ensure that the angular momentum transported outwards returns to the binary orbital motion (see Buat-Ménard et al. 2001, and references therein). A shock front (bright or hot spot) is formed where the stream of matter from the secondary hits the disc (see Fig. 1.1a). Once in the disc, some material accretes onto the surface of the white dwarf while some other carries away the angular momentum. As long as matter keeps flowing the disc is maintained.

1.2.3 Discs outbursts: the disc instability model

It is commonly accepted that outbursts are triggered by a thermal-viscous instability in the accretion disc (originally suggested by Osaki 1974). Basically, the accretion rate on the white dwarf is low during quiescence, while in outburst the accumulated matter in the disc is dumped onto the white dwarf. The physical cause of the instability is partial ionization of hydrogen, as first pointed out by Meyer & Meyer-Hofmeister (1981). The opacity (the

[2]Of special importance for the whole area of accretion disc research has been the work by Shakura & Sunyaev (1973), who calculated the radial structure of slim accretion discs subsuming all the unknown physics concerning the nature of viscosity in the parameter α, such that the viscosity $\nu = \alpha c_s H$, with c_s the local sound speed and H the scale height of the disc.

ability to obstruct the flow of radiation) of partially ionized hydrogen gas is extremely sensitive to temperature ($\propto T^{10}$). In particular, some of the free electrons combine with hydrogen atoms to create H^- ions which are especially efficient at absorbing photons.

If a disc is in thermal equilibrium the heat produced by viscous interaction is equal to the energy radiated away, so that its temperature is held constant with respect to time. This equilibrium state depends on the small variation of opacity with temperatures at which the hydrogen gas is kept either neutral or fully ionized ($T \lesssim 5000$ K and $T \gtrsim 10\,000$ K respectively).

A decrease in the viscosity of the material leads to a decrease in the temperature and the mass transport through the disc. Remember that viscosity ensures angular momentum redistribution so material can flow through the disc. However, since matter is streaming from outside, the surface density (Σ) increases which leads in turn to an increase in temperature ($A \longrightarrow B$ in Fig. 1.4). Material is piled up in the disc since the mass transfer rate from the secondary is higher than the mass accreted by the white dwarf. At $T \sim 7000$ K partial ionization of hydrogen sets in. If the temperature is increased a little further, most of the energy goes to create even more ions causing a huge increase in opacity. In this case, the disc is no longer capable of radiating enough energy away to lower the temperature. Therefore, the temperature climbs further and the disc becomes thermally unstable ($B \longrightarrow C$). The instability lasts until the hydrogen gas is completely ionized ($T \sim 10\,000$ K). At this stage, the opacity of hydrogen loses its extreme sensitivity to temperature, and the disc settles into a quasi-equilibrium state. In this high temperature state the viscosity is very high, leading to a redistribution of matter in the disc and enhanced accretion onto the white dwarf which is identified with an outburst. Since the inward flow of material through the disc exceeds that entering the disc from the mass-transfer stream, the surface density and with it the temperature decreases ($C \longrightarrow D$). If the temperature falls low enough, the hydrogen can recombine and this instability leads to a steep drop in temperature until hydrogen becomes neutral again at ~ 5000 K and a new

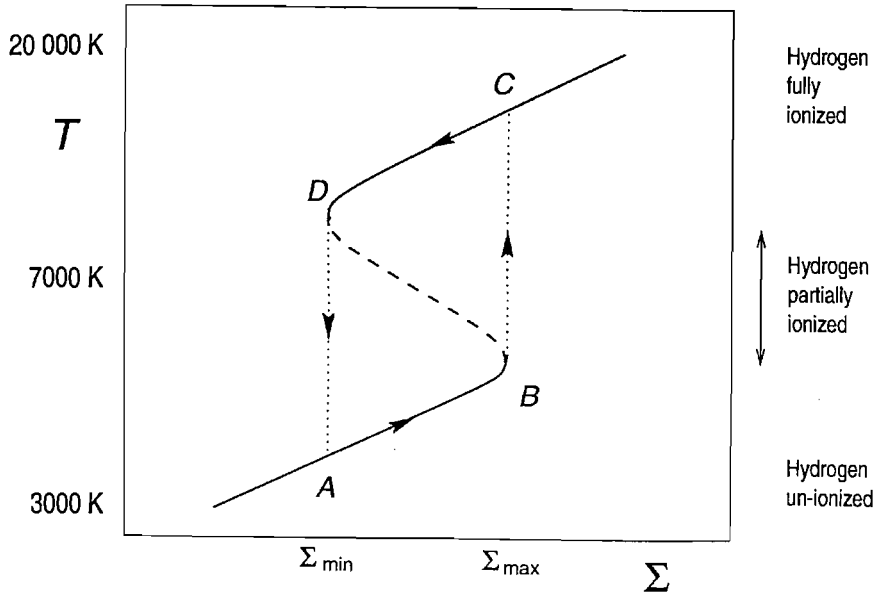

Figure 1.4: Disc Instability Model. Conditions in the disc oscillates about the equilibrium values, $A \longrightarrow C$, leading to the observed outbursts activity in dwarf novae. See text for a detailed description. From Hellier (2001).

quasi-equilibrium regime is entered ($D \longrightarrow A$) identified as quiescence. This is then the new starting point for the next cycle. The difference between these two equilibrium states is a large difference in temperature which leads to a large difference in the amount of radiation emitted. However, the change in disc brightness caused by the transition from the cold, neutral to the hot, ionized state is not sufficient to explain the observed amplitude of the outbursts. To match the observations, an additional (arbitrary) change in the disc viscosity is introduced in the form of an α_{cold} and α_{hot}[3], which differ by about an order of magnitude (Meyer & Meyer-Hofmeister 1984). For a review on dwarf nova outbursts see Cannizzo (1993) and Ludwig et al. (1994) for a detailed parameter study.

The mass transfer rate determines whether the disc is thermally stable or not. The critical mass accretion rate above which the flow of material through the disc is constant and hence the instability driving outbursts is suppressed is given by Osaki (1996), Meyer

[3] α_{cold} and α_{hot} are two different α parameters for the lower and upper branch of the S-curve

& Meyer-Hofmeister (1983) and Cannizzo & Wheeler (1984). Their expressions can be approximated as,

$$\dot{M} \simeq 1.6 \times 10^{-10} R_{d_{10}}^{2.6} M_1^{-0.87} M_\odot \, \mathrm{yr}^{-1} \tag{1.4}$$

where $R_{d_{10}}$ is the radius of the accretion disc in units of 10^{10} cm (Shafter 1992).

Nova-like systems (see next section) show steady state discs corresponding to mass transfer rates greater than the critical value above ($\gtrsim 10^{-9} M_\odot \mathrm{yr}^{-1}$) and therefore do not exhibit outbursts. Dwarf novae, on the other hand, have mass accretion rates below the critical value and give rise to thermally unstable discs. Z Cam stars are on the borderline between the nova-likes and the dwarf novae, with a mass transfer rate that fluctuates about the critical value (Meyer & Meyer-Hofmeister 1983; Lin et al. 1985; Buat-Ménard et al. 2001). This type of dwarf novae shows outbursts occasionally interrupted by periods in which the system stays at more or less constant brightness at a level intermediate between outburst maxima and minima, the so-called standstills.

Although the thermal-viscous disc instability model identifies a physical cause for the instability - partial hydrogen ionization - the outburst cycles it produces differ in many important respects from the observed ones (see e.g. Smak 2000; Lasota 2001). The need to include various processes which play an important role in the physics of the disc outbursts cycle is now widely accepted: irradiation of the disc and secondary star, inner disc truncation and mass transfer rate fluctuations (see e.g. Schreiber et al. 2000).

1.3 CV classification

CVs are divided into different types according to their observed properties. Some of these properties reflect the inclination at which a system is viewed, but most are a reflection of the orbital period of the binary, the mass transfer rate and the magnetic field strength of the accreting white dwarf. The field strength controls whether or not a disc can be formed

at all. The orbital period is a measure for the size of the disc; the longer the orbital period, the bigger the Roche lobe of the white dwarf, and the bigger the disc can be. Typical CV discs fill $\sim 50-80\%$ of the Roche lobe of the white dwarf (Harrop-Allin & Warner 1996). Since the critical mass transfer rate, defined in Eqn. 1.4, strongly depends on the size of the disc, this, together with the accretion rate, defines whether the disc is stable (hot upper branch of Fig. 1.4) or unstable (= occurrence of outburst). Fig. 1.5 shows the orbital period distribution of the different types of CVs from the Ritter and Kolb catalogue (Ritter & Kolb 2003). The most striking feature is the lack of systems (of any type) with periods between 2 and 3 hours, the so-called period gap, while there are many systems above and below this period range. Another obvious peculiarity in the orbital distribution is the decay in numbers of systems at long orbital periods and the sharp cut off at ~ 80 min. A successful theory of CVs must be able to explain the shape of the orbital period distribution as well as the origin of the period gap and the phenomena characterizing each of the following subclasses:

1. **Classical novae** Found preferentially at orbital periods above the gap (see Fig. 1.5), they experience eruptions ranging from 6 to more than 18 magnitudes, lasting from months to years. These outbursts are powered by a thermonuclear runaway due to the deposition of hydrogen-rich material onto the white dwarf. As the accreted material piles up on the surface of the white dwarf, it compresses the material at the base of the envelope. As a consequence the temperature and pressure increase. Eventually the density will be so high that the material at the bottom of the hydrogen envelope becomes degenerate, and it does not respond to the increase of temperature in the same way as normal matter would (i.e. expand to keep material in hydrostatic equilibrium). Instead, temperature increases even further to a point where nuclear reactions takes place leading to a runaway effect (nuclear reaction increase the temperature which increases the reaction rate and so on). The runaway continues until the rise in temperature causes the gas pressure to exceed the degen-

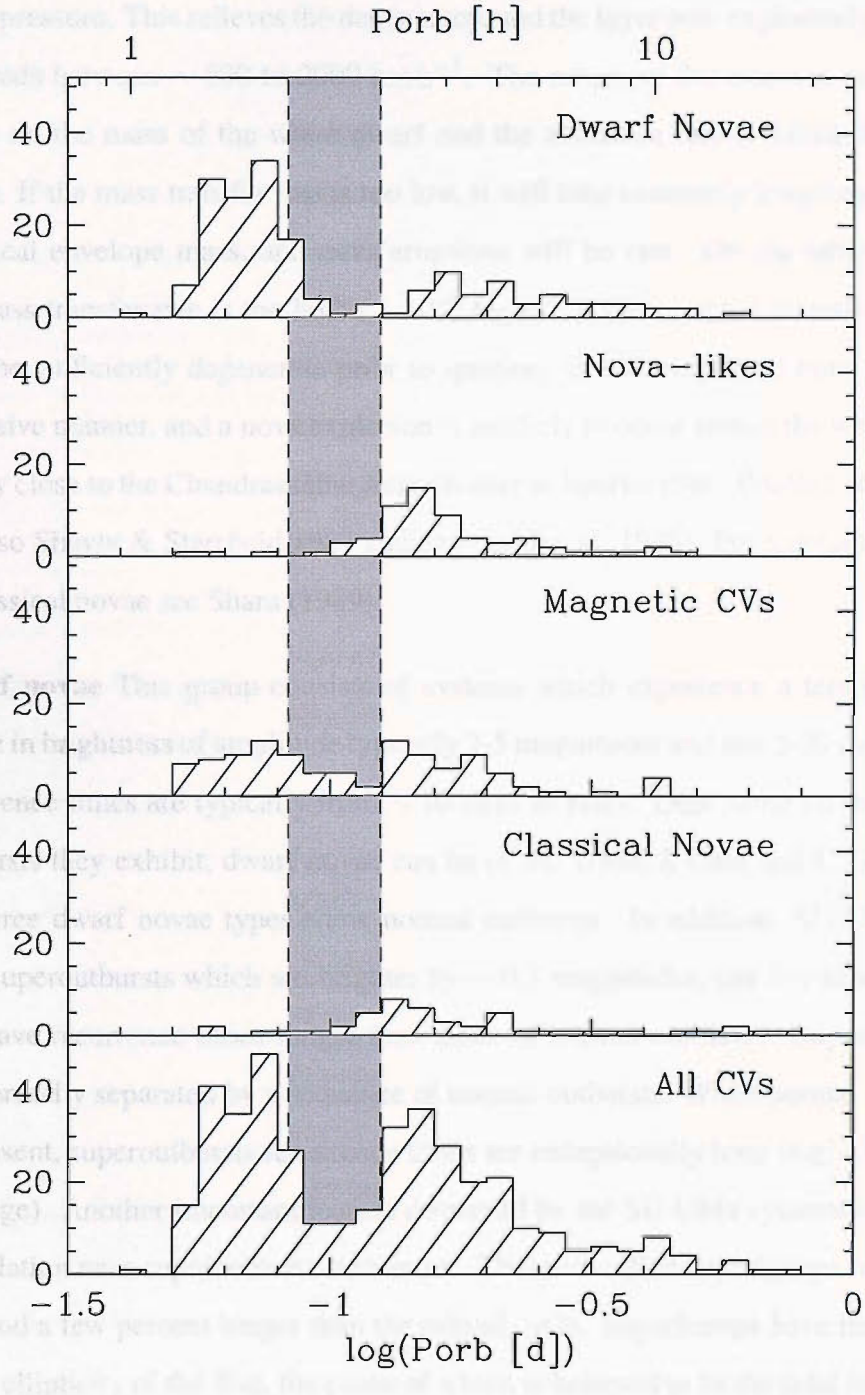

Figure 1.5: Orbital period distribution of the different types of CVs. Note that AM CVn systems were excluded from this figure. The most noticeable features in the 'All CVs' period distribution is: a decay in numbers of CVs at long orbital periods, a lack of systems in the 2-3 h orbital period range and a sharp cut-off at $\sim$ 80 min.

eracy pressure. This relieves the degeneracy, and the layer now explosively expands at speeds between $\sim$ 500 to 2000 km s^{-1}. The nature of the eruption mainly depends on the mass of the white dwarf and the accretion rate (Prialnik & Kovetz 1995). If the mass transfer rate is too low, it will take extremely long time to build a critical envelope mass, and nova eruptions will be rare. On the other hand, if the mass transfer rate is too high ($> 10^{-8} M_{\odot}$yr^{-1}), the accreted material will not become sufficiently degenerate prior to ignition, the envelope will burn in a non-explosive manner, and a nova explosion is unlikely to occur unless the white dwarf is very close to the Chandrasekhar limit (Kutter & Sparks 1980; Prialnik et al. 1982; see also Shaviv & Starrfield 1987 and Starrfield et al. 1985). For a detailed review of classical novae see Shara (1989).

2. **Dwarf novae** This group consists of systems which experience a temporary increase in brightness of amplitude typically 2-5 magnitudes and last 2-20 days. Their recurrence times are typically from $\sim$ 10 days to years. Depending on the type of outbursts they exhibit, dwarf novae can be of SU UMa, Z Cam and U Gem type. All three dwarf novae types show normal outbursts. In addition, SU UMas display superoutbursts which are brighter by $\sim$ 0.7 magnitudes, last five times longer and have recurrence times longer than those of normal outbursts. Superoutbursts are normally separated by a sequence of normal outbursts. When normal outbursts are absent, superoutbursts recurrence times are exceptionally long (e.g. 33 years in WZ Sge). Another important feature displayed by the SU UMa systems is a hump modulation near superoutburst maximum. These so-called superhumps recur with a period a few percent longer than the orbital cycle. Superhumps have their origin in the ellipticity of the disc, the cause of which is believed to be the tidal interaction with the secondary. SU UMas are all short orbital period systems (below the gap). Z Cam are characterized by the "standstill" phenomenon I described in Sec. 1.2.3: the decline from outburst maximum is interrupted, and the luminosity of the system settles to a value $\sim$ 0.7 mag lower than the peak luminosity. Smak (1983) described

Z Cam stars as an intermediate case between stable nova-like stars (see below) and unstable dwarf novae (e.g. Schreiber et al. 2002). In fact, Z Cam periods are concentrated above the gap, just as nova-like variables are. U Gem stars comprise those dwarf novae with the most regular outbursts, which do not belong to the SU UMa and Z Cam type. They are in general found with periods above the gap.

3. **Nova-like variables** These systems do not undergo quasi-periodic outbursts. They are instead characterized by a high, steady accretion rate which places these systems on the stable upper branch in Fig. 1.4. However, a number of nova-like variables, the VY Scl stars, most of them with periods between 3-4 h, exhibit low states during which mass transfer from the secondary and/or accretion onto the white dwarf decreases or shuts off completely. As I mentioned in Sec. 1.1.1, the reason for the low states is thought to be related to the donor star but its nature is uncertain; one possibility is that they are associated with the magnetic activity of the secondary (see Hessman et al. 2000). Recently, Thorstensen et al. (1991) proposed the existence of another subgroup of nova-likes variables which they called SW Sex stars (after their prototype). SW Sex stars are grouped together because they exhibit several unusual properties: (a) they are often eclipsing systems with orbital periods of 3-4 hrs; (b) their continuum eclipses are more V-shaped (as opposed to U-shaped) than those of other nova-like variables; (c) their optical emission lines are single-peaked, instead of double-peaked (as expected for high-inclination, disc-formed lines); (d) their Balmer and HeI lines remain largely unobscured during primary eclipse, but display absorption events at the opposite orbital phase; (e) the radial velocity curves derived from their optical emission lines lag substantially behind the phase one expects from the white dwarf on the basis of eclipses. Several models have been put forward to account for the SW Sex stars, and although each is capable of explaining a subset of the SW Sex behavior, none has so far been able to explain all the features listed above (e.g. Knigge et al. 2000, and references therein). Among the nova-like variables there also two other subgroups: UX UMa stars with persis-

tent, broad Balmer absorption line spectra, and RW Tri stars displaying pure line spectra (albeit occasionally with sharp absorption cores). Here is a clear case where the morphological class definition depends primarily on the viewing geometry, contrary to all other classes where the distinction is based mainly on the combination of values for the orbital period, the mass accretion rate and the white dwarf magnetic field strength. In the case of UX UMa and RW Tri, the former contains systems with low inclination and the latter those having mainly high inclination.

4. **Magnetic CVs** In these systems the magnetic field of the white dwarf ($1 \lesssim B \lesssim 200$ MG) plays an important role in the interaction between the two stellar components (see Fig. 1.1b). Systems with a $10 \lesssim B \lesssim 200$MG white dwarf cannot form a disc and matter from the secondary is channelled through the magnetic field lines until it impacts (at the free fall velocity of ~ 3000 km s^{-1}) on the surface of the white dwarf near its magnetic pole(s). This class of magnetic CVs (which contains 67 confirmed members[4]) are called polars or AM Her systems, and the white dwarf spin is synchronized with the orbital motion of the binary. The synchronism is thought to be due to the interaction of the strong magnetic field of the white dwarf with the field of the secondary. The impact of the accreted material on the surface of the white dwarf generates a shock, which is the source of X-rays. In systems in which the white dwarf has $B \sim 1 - 10MG$, a disc can form but can only extend inwards down to the radius where magnetic pressure begins to dominate. These systems are called intermediate polars (IPs) or DQ Her stars. Apart from a few exceptions (e.g. AE Aqr and EX Hya), the white dwarfs of IPs rotate with spin periods of the order ten percent the orbital period (i.e. $P_{\rm spin} \sim 0.1 P_{\rm orb}$; Patterson 1994), ranging from 33 s to ~ 2 h. The IP class contains fewer confirmed members than the polar class[5], (23 systems). The light curves can display modulations on the orbital period, the spin period and/or the beat period between the spin and orbital

[4]http://www.mssl.ucl.ac.uk/www_astro/gal/polar.html

[5]http://lheawww.gsfc.nasa.gov/users/mukai/iphome/members.html

cycle [6]. High mass transfer rates in IPs make them stronger hard X-ray emitters than their polar cousins. Any theory which purports to explain the period distribution of CVs must also account for the properties of the magnetic CVs which, as a group, comprise some $\sim 22\%$ of all CVs of known orbital period (Ritter & Kolb 2003). In the 'Magnetic CVs' panel in Fig. 1.5, the majority of polars are found below the gap, while the IPs are located mostly above the gap.

5. **AM CVn** These systems are ultracompact binaries with orbital periods as short as $\sim$ 10 min, and secondaries composed mostly of helium. Consequently, the accretion discs in these systems are nearly pure helium. At present there are two popular models for the nature of AM CVn systems: (a) a double-degenerate model and (b) a model in which the primary is a white dwarf and the secondary is a semi-degenerate helium star. Their evolutionary track is believed to be essentially the same as in normal CVs but shifted to shorter periods. The study of AM CVn systems goes beyond the scope of this thesis. I have included them here merely for completeness.

For a thorough review on the properties of these different groups see e.g. Patterson (1984) and Warner (1995).

1.4 Spectral characteristics

Much of the work contained in this thesis is based on spectroscopic observations. The majority of the system parameters can be deduced from spectroscopy alone. Orbital periods and estimates for the radial velocities of the stellar components can be obtained by measuring the Doppler shift of the emission and absorption lines. Unfortunately, radial velocity studies cannot be used to obtain reliable system parameters for SW Sex stars because of their emission line properties (refer to Sec. 1.3). In Chapter 4 I will show an

[6] $1/P_{\rm beat} = 1/P_{\rm spin} - 1/P_{\rm orb}$

alternative way in which data from one of the occasional low states experienced by the SW Sex system, DW UMa, is used to estimate a set of its system parameters. One can also estimate physical parameters such as the mass accretion rate, the temperature of the white dwarf and the spectral type of the secondary, masses and radii of both components, as well as the distance to the system. In this section I outline the composite nature of the CV spectrum, describing the constituents and how much each of them contributes to the resultant spectrum (see Fig. 1.6).

1.4.1 The white dwarf

Most white dwarfs in CVs have temperatures higher than $\sim$ 12000 K (Gänsicke 2000; Sion 1999) and therefore emit mostly in the ultraviolet. Their spectra are characterized by a continuum rising towards the blue with broad hydrogen absorption lines from the white dwarf photosphere. The broadening of the lines is due to a phenomenon called pressure broadening. Because of the intense gravity at the surface of white dwarfs and the resulting high density, the energy levels of atoms and ions are perturbed by the nearby presence of other atoms, ions, electrons etc. Any transitions occurring will therefore have a somewhat different wavelength from 'normal', and the average spectral line resulting from such transitions will be broadened. This effect increases with pressure and in the case of white dwarfs dominates over any other broadening mechanism (e.g. thermal broadening).

1.4.2 The donor star

The low temperature ($T \sim 3000$ K) donor star emits mainly at red and infrared wavelengths. The low temperature atmosphere of the donor star allows molecules to form. These molecules can be detected in the donor star spectrum as broad absorption bands. In mid to late M-stars the most noticeable of these bands is titanium oxide (TiO).

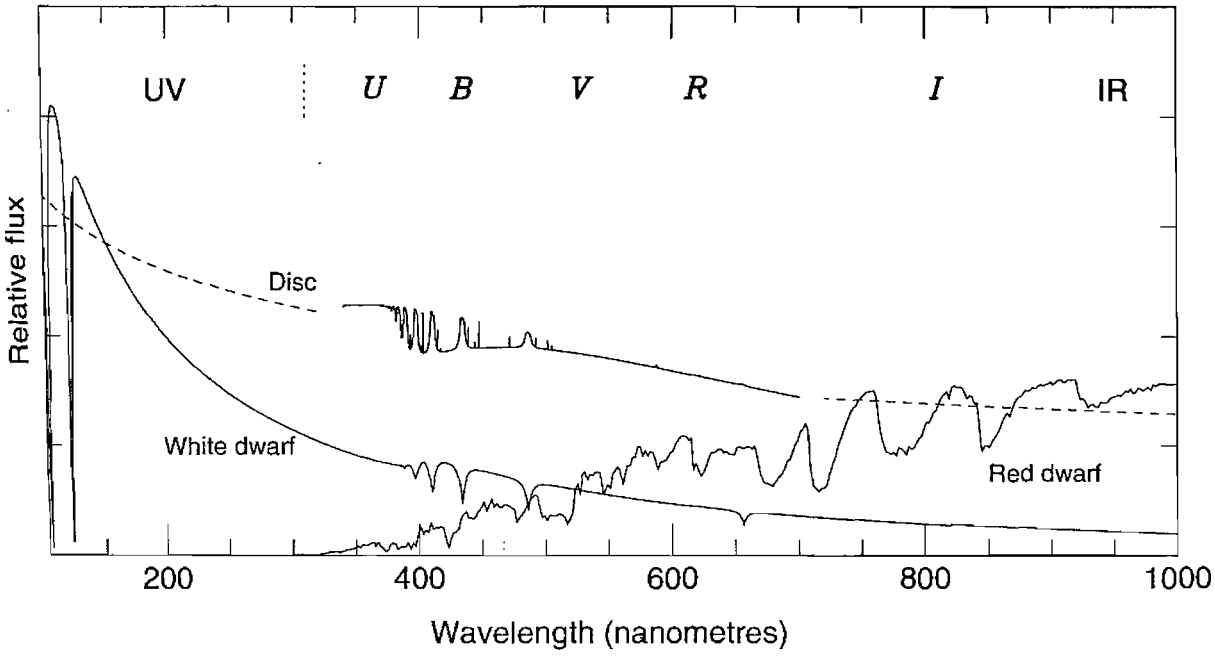

Figure 1.6: Schematic spectra of the components of a CV. The labels *UBVR* and *I* show the regions of the spectrum from the different filters. In the case of the accretion disc model, the energy distribution is the result of the summed radiation of blackbodies with different temperatures. Emission lines have only been added in the optical region (solid line). From Hellier (2001).

Fig. 1.7 and 1.8 show a selection of spectra from nearby isolated main-sequence K-L7-type stars with their respective two micron all sky survey (2MASS) colours (i.e. J, H, K). In Chapter 6 I use these spectra as templates to constrain the contribution of the secondary star to the optical/IR observations in a new and unusual system, HS 2331+3905.

1.4.3 The accretion disc

In the accretion disc about half of the gravitational potential energy of the accreting material is released heating the disc to typical temperatures of $\sim 3000 - 100000$ K in the

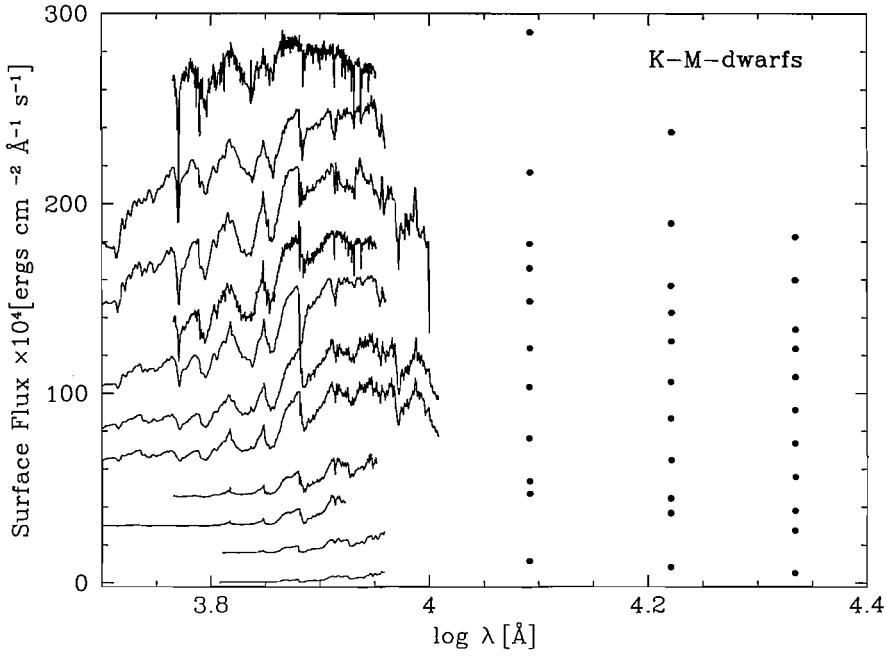

Figure 1.7: Energy distribution for isolated K7, M0.5, M1.5, M2, M3, M4, M4.5, M6, M7, M8 and M9 stars from top to bottom. The dots show the two 2MASS colours, J, H and K, for each of the stars. Starting with M8, each spectral type energy distribution has been displaced from the preceding one by 10×10^4 surface flux units for clarity. The spectra were provided by K. Beuermann (Beuermann et al. 1998).

outer and inner part of the disc respectively[7]. If the disc is assumed to be optically thick (opaque to radiation) in the vertical direction then its temperature distribution can be approximated as the sum of a blackbody spectrum of the appropriate temperature for each of the annuli. If in addition one assumes a stable state disc (see Sec 1.2.3) which is much bigger than the size of the white dwarf, then the temperature distribution can be simplified as $T \propto R_d^{-3/4}$, (see e.g. Frank et al. 1992). This temperature distribution is only useful as a rough estimate since external effects (such as irradiation by the primary, tidal interaction with the secondary, etc.) can heat the disc with a consequent departure from

[7]Note that these temperatures strongly depend on the mass accretion rate. The temperatures given here are typical of $\dot{M} \sim 10^{-9} M_\odot \mathrm{yr}^{-1}$ discs.

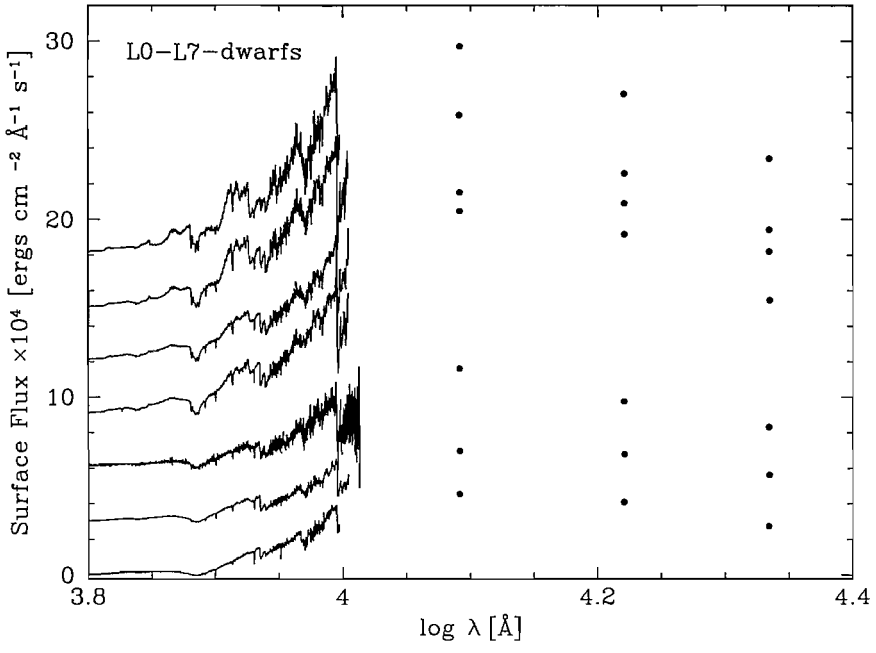

Figure 1.8: Energy distribution for isolated L0, L1, L2, L3, L4, L5 and L7 stars from top to bottom. The dots show the two 2MASS colours, J, H and K, for each of the stars. Starting with L5, each spectral type energy distribution has been displaced from the preceding one by 2×10^4 surface flux units for clarity. The spectra were provided by D. Kirpatrick (Kirkpatrick et al. 1999, 2000)

$T \propto R_d^{-3/4}$. Its spectrum dominates over the other components[8] (i.e. white dwarf and donor star), with a maximum in the ultraviolet which falls monotonically towards longer wavelengths. Superposed onto this continuum are prominent emission (or absorption) lines, mainly from low ionization species such as hydrogen (Paschen, Balmer & Lyman series), helium (He I), calcium (Ca II) and iron (Fe II). The excitation of the lines tends to increase with the mass accretion rate and with the magnetic field strength of the white dwarf. In fact, the high ionization line, He II, serves as a tracer of high accretion rate systems (nova-like variables) or magnetic CVs. There are two possibilities for an emission line spectrum to be observed: (1) the disc needs to be optically thin in the continuum and

[8]This is not necessarily true in quiescent dwarf novae. Here we keep the assumption of an optically thick disc.

significantly optically thick in the lines or (2) an optically thick disc (in the continuum and/or in the lines) underlying an optically thin (in the continuum but not in the lines) hot chromosphere. In quiescent dwarf novae (low mass accretion rate discs), the disc spectrum always contains emission lines which could be the result of either of the two possibilities described above. The occurrence of emission lines from a high-mass transfer disc, such as in nova-like variables, or dwarf novae in outburst, strongly depends on the inclination (emission lines in high inclination systems, absorption in low inclination systems) and is an optical depth effect. At the interface between the inner accretion disc and the white dwarf, the so-called boundary layer (see Fig. 1.1a), material rotating at Keplerian velocities is decelerated to the rotational velocity of the white dwarf. The flow is thermalized and radiated away as far ultraviolet and X-ray emission (Shaviv 1987).

1.4.3.1 Line profiles

As I mentioned in Sec. 1.2.2 the velocity of the gas flow through the accretion disc is much higher that the sound velocity. The profiles of the lines formed in such a disc are dominated by Doppler broadening and give information on the velocity and intensity distributions in the disc. The radial velocity (the velocity projected on the line of sight) of a point located at (r, θ), where θ is the azimuth of the observer with respect to the radius vector, is

$$v_{\rm rad} = v_k(r) \sin\theta \sin i$$

The orbital inclination, i, is the angle between the perpendicular to the orbital plane and the line of sight, and v_k is the Keplerian velocity of the gas. If we compute the lines of constant $v_{\rm rad}$ we obtain a dipole pattern on the surface of the disc, as can be seen in Fig. 1.9a. The result of combining the contribution of the different velocity elements is a double-peaked line profile as in Fig. 1.9b. The peaks are a reflection of the outer disc velocity, reduced by the $\sin i$ projection factor, and dominate over other constant velocity regions in the line profile because of the greater area. Emission at the line wings originates

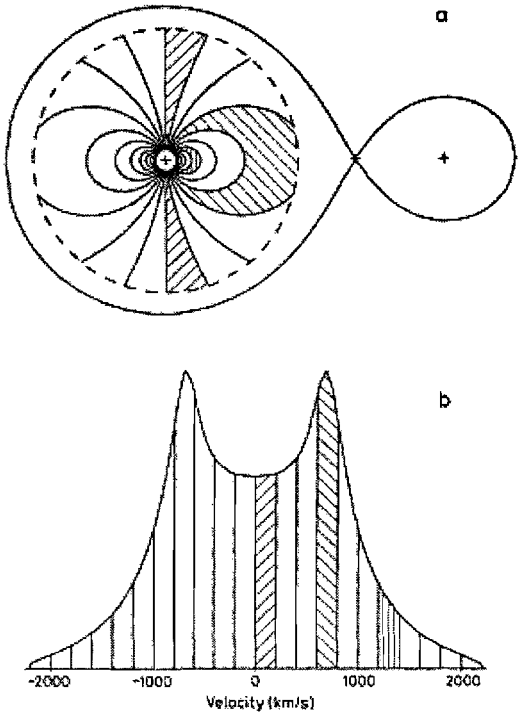

Figure 1.9: (a) Keplerian disc with contours of constant radial velocity. (b) Velocity profile of emission lines from the disc. Emission in the shaded velocity ranges originates in corresponding shaded regions on the disc. From Horne & Marsh (1986).

in the regions very close to the primary star (high velocity regions). The corresponding surfaces (see shaded areas of Fig. 1.9) are very small, so the intensity in the line wings is also very small. The center of the line corresponds to regions in the disc perpendicular to the line of sight where the radial velocity of a gas particle is zero. Clearly, the width of the profiles decreases with inclination because the projected velocity in the line of sight decreases. Thus we expect to observe double-peaked profiles in moderately inclined discs.

As the disc is centred on the white dwarf it follows the orbital motion of the compact star around the center of mass of the system. This means that the double-peaked line profile executes an S-wave in sympathy with the white dwarf. This property of the line profile is commonly used to obtain the orbital period of close binary systems. It should, nevertheless, be used with care, as shown in the case of HS 2331+3905 in Chapter 6.

Radial velocity studies of HS 2331+3905 failed to reveal the orbital period of the system at first instance. The dominant radial velocity variability had to be subtracted in order to detect the orbital motion of the system seen in the photometry.

1.5 Future chapters

In Chapter 2 I introduce the theory of CV evolution and I discuss the discrepancies between theory and observations. Here I also discuss the approach used in this thesis to tackle this problem. Data acquisition and reduction is described in Chapter 3. A detailed analysis of the system parameters of DW UMa based on far-ultraviolet (FUV) observations is given in Chapter 4. In Chapter 5 I present the study of a recently discovered magnetic CV, 1RXS J062518.2+733433. Chapter 6 describes the observational study of the unusual CV, HS 2331+3905, in which the dominant radial velocity variability does not correspond to the orbital period of the system, contrary to all other known CVs. Chapter 7 concentrates on a full discussion of the main aim of this work. Finally, a summary of the content of this thesis is given in Chapter 8.

Chapter 2

The Evolution of Cataclysmic Variables

Over the past few years it has become increasingly clear that our understanding of the evolution of CVs is a rather unsettled matter. A number of the predictions made by the standard theory of CV evolution, disrupted magnetic braking, are in direct conflict with observations. The current sample of galactic CVs is likely to be biased towards bright, young CVs, and therefore is not representative of the intrinsic CV population. A significant progress in our understanding of the evolution of close binaries relies on the analysis of unbiased observations of large samples of such objects.

The orbital period is the only global system parameter accurately determined for a large number of CVs. The observed orbital period distribution is therefore a major diagnostic tool to constrain the evolutionary history of the whole class of CVs.

In this Chapter I start by describing the standard model for CV evolution. In Sec. 2.2 I outline the disagreements between theory and observations, exposing the observational biases of the currently known CV sample. Some of the recent progress towards a better understanding of the CV evolution, including additions and alternatives to the prevailing

theory are covered in Sec. 2.3. Finally in Sec. 2.4 I describe the projects I am currently involved with and whose main objective is resolving the issue of the likely statistically incompleteness of the currently known CV population.

2.1 The standard model for CV evolution

2.1.1 Pre-Cataclysmic evolution

Stars destined to become CVs begin as binaries separated by a few hundred solar radii, with orbital periods of ~ 10 years (zero-age main-sequence binaries; ZAMS). The stellar components consist of an intermediate mass star ($\sim 1 - 10 M_{\odot}$) with a low mass companion ($< 1 M_{\odot}$). The more massive star evolves more rapidly, expands, and in doing so it fills its Roche lobe. Dynamically unstable mass transfer is initiated due to a combination of two effects: conservation of angular momentum which reduces the orbital separation[1], and the tendency of the convective envelope of the giant to expand in response to mass loss (Paczynski 1965). The secondary cannot assimilate such an influx (Webbink 1985), so the material forms an extended structure around both stars: the system enters into a 'common envelope' phase (Meyer & Meyer-Hofmeister 1979; Iben & Livio 1993). Friction within the envelope drains the orbital energy of the binary, causing the secondary to spiral inwards. At some point during this process, the heat deposited in the envelope exceeds the binding energy and the envelope is ejected as a planetary nebulae (Livio & Soker 1988; Taam & Bodenheimer 1989). The time spent in the common envelope stage is very short, on the order of $\sim 10^3$ yr. If coalescence between the core of the giant (the

[1]Material is moved from the more massive star further away from the center of mass of the binary and since angular momentum is conserved the system responds by decreasing the binary separation.

future white dwarf) and its companion does not occur,[2] we are left with a white dwarf and a late-type main sequence secondary which in general underfills its Roche lobe (pre-CV phase). Due to tidal interactions with the white dwarf, the secondary will be brought into synchronous rotation very rapidly if the binary separation is not too large. Angular momentum loss, primarily via magnetic braking (see Sec. 2.1.2), drives the systems towards shorter periods and eventually brings the secondary into contact with its Roche lobe (zero-age CV). For a given initial period and core mass of the giant in the pre-common envelope phase, the post-common envelope (or pre-CV) orbital period is shorter the more massive the total mass of the giant, as more orbital energy is needed to eject a more massive envelope. About 22% of all zero-age CVs are predicted to form in the period gap, although subsequent stellar evolution is expected to reduce the fraction of CVs in the gap (Politano 1996; Kolb 1993).

Another interesting possibility for the origin of CV precursors has been proposed by Livio (1982) (see also Soker et al. 1984). In their model the primary's giant envelope engulfs a planet/brown dwarf, which through accretion transforms itself into a low mass star. In their simplified calculations, fine tuning of the system parameters is needed for a system such as this to survive the common envelope phase. If the binary separation is too far ($a \gtrsim 1000 R_{\odot}$) the planet will not accrete enough material to go through the next stage (pre-CV phase). If, instead, the separation is too close ($a \lesssim 500 R_{\odot}$) the planet will coalesce with the giant.

2.1.2 Disrupted magnetic braking

The disrupted magnetic braking model was developed 20 years ago with the main purpose of explaining the 2 - 3 h period gap in the observed period distribution of the bottom panel

[2]If the timescale for mass loss from the envelope were longer than the time of the spiralling process then coalescence would occur.

of Fig. 1.5 (e.g. Rappaport et al. 1983; Spruit & Ritter 1983; Paczynski & Sienkiewicz 1983; Patterson 1984; King 1988). The essential idea is that CVs evolve towards shorter periods because of a combination of angular momentum losses: magnetic braking, owing to a magnetized wind from the donor star (Verbunt & Zwaan 1981), and the less efficient gravitational radiation (Kraft et al. 1962; Krzeminski & Kraft 1964) from the orbiting of the two stars (see Howell et al. 2001, for a recent review). The net effect of reducing orbital angular momentum via magnetic braking is possible because, as mentioned earlier, the secondary's rotation is tidally synchronized with the orbital motion. Gravitational radiation, on the other hand, only requires the orbital motion of the binary to drain angular momentum from the system. The timescales for the angular momentum loss are (Kolb & Stehle 1996):

$$\tau_{MB} = -\left(\frac{J}{\dot{J}}\right)_{MB} = 2.2\times10^{9}\frac{M_1}{(M_1+M_2)^{1/3}}R_2^{-4}P_{orb}^{10/3}(d)yr$$

and

$$\tau_{GR} = -\left(\frac{J}{\dot{J}}\right)_{GR} = 3.8\times10^{11}\frac{(M_1+M_2)^{1/3}}{M_1M_2}P_{orb}^{8/3}(d)yr$$

for magnetic braking and gravitational radiation, respectively. Typical evolutionary timescales are $\sim 10^8$ yr for systems to evolve from $P_{orb} \sim 10$ h to $P_{orb} \sim 3$ h, $\sim 10^9$ yr to go through the period gap and $\sim 10^9$ yr again from $P_{orb} \sim 2$ h to the period minimum.

Once the secondary fills its Roche lobe, the mass transfer rate is determined by the prevailing mechanism of angular momentum loss (Fig. 2.1). In the early phases of the CV life, in the period range from ~ 10 h to ~ 3 h, magnetic braking dominates over gravitational radiation, driving mass transfer rates at $\sim 10^{-9} - 10^{-8} M_\odot$ yr^{-1}. The rapid mass loss associated with magnetic braking drives the secondary out of thermal equilibrium, causing it to bloat beyond its main-sequence radius (Ritter 1985). At some point in the evolution, the secondary becomes completely convective (at $\sim 0.23\ M_\odot$) and magnetic braking is believed to be greatly reduced (Rappaport et al. 1983; Spruit & Ritter 1983 and Taam & Spruit 1989). This occurrence may be related to the changing character of the dynamo believed to drive the magnetic activity of CV secondary stars. The magnetic

field is either destroyed, or, more likely, rearranged (see Taam & Spruit 1989, and references therein). The reduction of magnetic braking results in a decrease of the angular momentum loss rate, and hence, of the mass loss rate of the secondary. As a reaction to the decreasing mass loss rate, the secondary starts to relax towards its thermal equilibrium structure, i.e. shrinks and detaches from its Roche lobe, bringing the mass transfer rate $\dot{M}$ to essentially zero. This is the cause of the period gap. The system reappears as a mass-transferring CV when gravitational radiation shrinks the Roche lobe enough to bring the secondary back into contact with it, at an orbital period of $\sim 2\,\mathrm{h}$. From then on the binary evolution occurs on the much longer timescale of gravitational radiation with mass transfer rates of $\sim 10^{-11} - 10^{-10} M_\odot\ \mathrm{yr}^{-1}$ (see Fig 2.1). By applying standard models for the formation and the evolution of CVs, Kolb & Stehle (1996) determined the age structure of a model population of Galactic CVs: systems above the gap have been typically formed $\sim 1.5 \times 10^9$ yr ago, while systems below the gap represent a much older population, formed $\simeq 3 \times 10^9$ yr ago. In the same study, they apply the age-velocity dispersion relation found by Wielen et al. (1992), to predict the CV's velocity dispersion as a function of orbital period (see also van Paradijs et al. 1996). According to their model, young systems above the gap have a smaller velocity dispersion than the older generation below the gap.

Below the period gap, as the orbital separation shrinks and the mass of the donor star decreases, the mass loss timescale increases, but the thermal timescale increases much faster. Eventually, the donor star will be unable to adjust itself to the mass loss on its thermal timescale (when its mass reaches $\sim 0.08 M_\odot$) and becomes degenerate (Paczynski 1981; Paczynski & Sienkiewicz 1981; Rappaport et al. 1982), behaving like a white dwarf: its radius increases when its mass decreases. As a result of this change in the mass-radius relation of the secondary star, the orbital period of a CV goes through a minimum during the course of its evolution. The actual period at which a CV bounces depends on the thermal timescale (which in turn depends on the internal structure of the donor star) and the mass transfer timescale (depending on the angular momentum loss rate), the

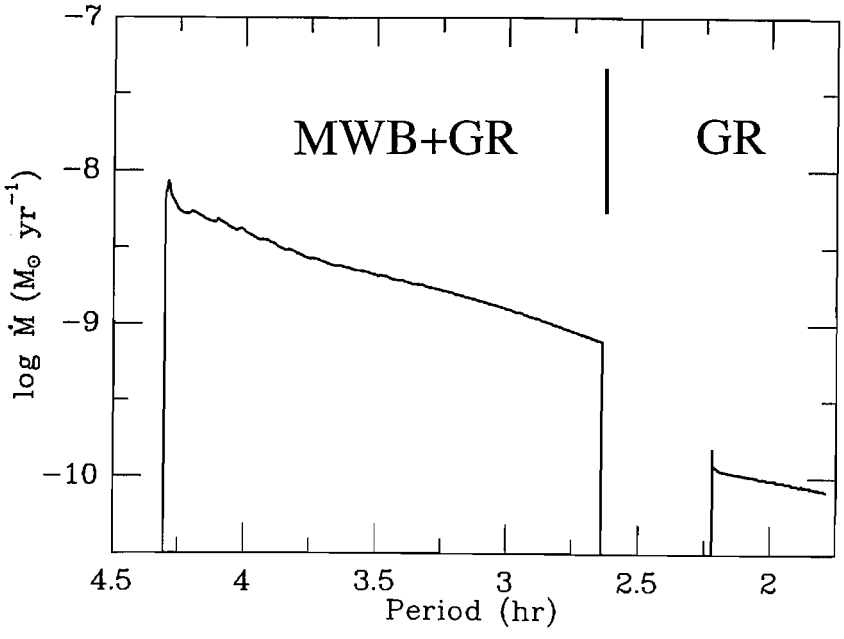

Figure 2.1: Once the secondary overflows its Roche lobe mass transfer rates are governed by the prevailing angular momentum loss mechanisms. Magnetic braking dominates in systems with $P_{\rm orb} \gtrsim 3$ h driving mass transfer rates at $\sim 10^{-9} - 10^{-8} M_{\odot} {\rm yr}^{-1}$. Gravitational radiation also operates in this range but at a much less extend. Systems with $P_{\rm orb} \lesssim 3$ h are driven by gravitational radiation only, causing low mass transfer rates at $\sim 10^{-11} - 10^{-10} M_{\odot}\,{\rm yr}^{-1}$. Modified from McDermott & Taam (1989).

two characteristic timescales for restoring and perturbing equilibrium respectively. The smaller the mass transfer timescale compared to the thermal timescale, the shorter the minimum period. The minimum period calculated by equating these two timescales, assuming gravitational radiation as the prevailing angular momentum loss mechanism, is $\sim 65 - 70$ min (Kolb & Ritter 1992; Howell et al. 1997). Those systems which manage to get past the period minimum are commonly called 'period bouncers'; good candidates are WZ Sge ($M_2 \simeq 0.058 M_{\odot}$, Patterson et al. 1998) and OY Car ($M_2 \simeq 0.07 M_{\odot}$, Pratt et al. 1999). A discussion of this late stage of CV evolution is given by Howell et al. (1997) and Patterson (1998).

2.2 Problems with the standard model

Despite the success of the disrupted magnetic braking model in explaining the period gap, there are a number of observational features that do not fit in well with the model's predictions:

- Standard population models (e.g. de Kool 1992; Kolb 1993; Politano 1996) typically give a galactic CV space density of up to $10^{-4}\,\mathrm{pc}^{-3}$, i.e. ~ 400 CVs within a distance of 100 pc, of which we currently know only a very small fraction ($\sim 10\%$). The ratio of magnetic/non-magnetic white dwarfs in CVs is 22% (if we only include confirmed polars and IPs; Ritter & Kolb 2003) while in isolated white dwarfs is $\sim 5\%$ (Jordan 1997; Wickramasinghe & Ferrario 2000). If we assume that the fraction of magnetic stars should be similar in both groups then we arrive independently to the same conclusion as the standard theory: there is a large fraction of CVs not accounted for.

- The predicted minimum orbital period for hydrogen-rich CVs is 65-70 min, instead of the observed cutoff at 80 min (Kolb & Baraffe 1999; Howell et al. 1997).

- The evolution lifetimes of stars near the shortest periods (1.3 h) should become drastically longer as the timescale for gravitational radiation losses increases (Paczynski & Sienkiewicz 1981). This together with the fact that period bouncers pass twice through that region implies very large numbers of CVs at or near the minimum period. Kolb (1993) predicted that $> 95\%$ of CVs should have orbital periods below the gap. Of these, $\sim 70\%$ should have already reached the period minimum near 80 min and be 'bouncing' back towards longer periods (see also Howell et al. 1997), and should be detected in the observed period distribution as "minimum period spike". From a close look at the observed orbital period distribution of Fig. 1.5 (bottom panel) it is obvious that observations do not agree with these predictions

(e.g. Kolb & Baraffe 1999).

- There is no observational evidence for a discontinuous change in the spin-down rate due to magnetic braking between late-type field stars that are fully convective (like the donor on CVs below the period gap) and those that have a radiative core (like donors of CVs above the period gap) (see Andronov et al. 2003).

- The period gap should be narrower for systems with low mass transfer rates (the dwarf novae) than for those having high mass transfer rates (nova-likes) (Shafter 1992 and Warner 1987). The reason for this is that the width of the gap depends on how far out of thermal equilibrium the secondary star is when magnetic braking is diminished, which in turn depends on the secondary star's mass-loss rate. The lower the mass transfer rate, the narrower the resulting period gap. If dwarf novae and nova-likes retain their distinction during the secular evolution of the system, then this appears to be in contradiction with the observed period distribution of Fig. 1.5: the period gap is actually wider for dwarf novae than it is for nova-likes. One possibility for explaining the wider gap apparently observed for dwarf novae is given by Livio & Pringle (1994) in terms of star spots[3]. Systems with low mean mass transfer rates are more easily interrupted by the star spot mechanism because the density and pressure are correspondingly lower at the L_1-point.

- There is a significant dispersion in the mass accretion rate or absolute magnitudes at a given orbital period (Hameury et al. 1989; Warner 1987; Patterson 1984). Mass transfer rates are observed to vary by over an order of magnitude, from $\sim 10^{-10} - 10^{-9} M_\odot \mathrm{yr}^{-1}$ in dwarf novae to $\sim 10^{-9} - 10^{-8} M_\odot \mathrm{yr}^{-1}$ in nova-like variables. Although there are large systematic errors in such estimates, the existence of an intrinsic scatter in any accretion rate-period relation is strongly supported by the coexistence of various CV subtypes at similar orbital periods. This

[3]Star spots are also believed to be the cause of the low states observed in some Polars, IPs and nova-like variables (Livio & Pringle 1994; Hessman 2000).

is because the sharp observed differences between the CV subtypes are generally ascribed to differences in the accretion rates. However, if the observed scatter in the accretion rate were characteristic of the long-term average mass transfer rate, features of the CV period histogram such as the period gap and minimum period probably could not be anything like as sharply defined as they are observed to be. Real differences in the long-term average mass-loss rates at a given period would cause the secondary stars to have widely varying degrees of disequilibrium, leading to very different minimum periods and period gaps for systems with high and low transfer rates, contrary to observations. King et al. (1995) show that irradiation of the secondary might account for the dispersion of mass transfer rates by inducing fluctuations on timescales of 10^5 yr.

2.2.1 Selection effects

A problem in interpreting the observed period distribution arises from strong selection effects in the discovery of CVs. Since different subclasses are discovered in different ways, they are also subject to very different selection effects. Variability, for example, makes the discovery of classical nova and dwarf nova much easier than that of any other class of CVs. The discovery probability is also strongly brightness-dependent, favouring the selection of high mass-transfer rate CVs (mainly systems above the gap). Colour surveys, for example, whose selection criteria are based on blue/ultraviolet excesses[4], are flux-limited (e.g. the Palomar-Green, $B_{\rm lim} \sim 16$; Green et al. 1982; Ringwald 1996). Many Polars and IPs systems are detected first as X-ray sources and only subsequently identified with CVs (e.g. Beuermann et al. 1999). The absence of discovered systems in a particular period range may well be a result of the absence of easily identifiable phenomena in that period range, rather than to the absence of CVs. If phenomena that

[4]As CVs typically contain a hot component (accretion disc/column,white dwarf) they show up as blue/ultraviolet excess objects in colour surveys.

increase the detection probability of a CV are concentrated at particular period ranges, an apparent dearth of observed systems could arise in the region between.

2.3 Additions/alternatives to the standard model

The widely accepted standard scenario of CV evolution described in Sec. 2.1 has remained essentially unchanged since it was established twenty years ago, even though it has been challenged by a number of alternative suggestions (Livio & Pringle 1994; King & Kolb 1995; Clemens et al. 1998; Kolb et al. 1998; Patterson 1998). More recently, a number of far-reaching modifications for the standard scenario have been proposed that warrant close scrutiny.

- Andronov et al. (2003) introduced an empirical angular momentum loss rate obtained from observations of main-sequence stars in open clusters covering a range of masses and ages (see also Sills et al. 2000; Pinsonneault et al. 2002). They show that the empirical timescale for angular momentum loss above the fully convective boundary ($P_{\rm orb} > 2$ h) is ~ 2 orders of magnitude longer than predicted by the theoretical models used so far. This has two direct and important consequences. First, the angular momentum loss timescale is significantly longer than the thermal timescale for all but the shortest period CVs, which implies that the secondary star will be in thermal equilibrium. Second, the timescale for CV evolution above the gap is increased significantly, so that for those CVs with unevolved secondaries it takes close to a Hubble time to reach the period gap from their pre-CV phase. Andronov et al. (2003) also provide evidence for a smooth transition in the empirical angular momentum loss properties at the onset of the fully convective boundary ($P_{\rm orb} \sim 3$ h), suggesting that something other than a phase transition in the angular momentum loss rate must be used to explain the origin of the period

gap. According to Andronov et al. (2003) magnetic braking remains an important angular momentum loss mechanism even in CVs with a fully convective secondary (i.e. CVs with $P_{\rm orb} < 3$ h). Due to the increased angular momentum loss below the gap, the predicted minimum CV period increases from 65-70 min (using only gravitational radiation) to $\sim$ 80 min (including the empirical magnetic braking in addition to gravitational radiation) in agreement with the observations. The authors also suggested a very interesting possibility to explain the period gap: the two distinct peaks in the period distribution (one above and one below the period gap) could reflect two different populations of objects with different origins, depending on the evolutionary state of the secondary at the onset of mass transfer. Using their empirical angular momentum loss rate the period evolution for the post-common envelope phase is very slow. The timescale for the formation of CVs can therefore be longer than the age of the galaxy, especially for systems containing low mass secondaries. This can solve the population density problem since less CVs will have been formed to the present day compared to the numbers predicted by the standard model. A problem with the reduced angular momentum loss is that the predicted mass transfer rates in systems above the gap are much lower that those estimated from observations. Another serious problem is that it predicts more pre-CVs than, at the moment, can be accounted for (see also the Binary Age Postulate scenario described below).

- Spruit & Taam (2001) suggested a circumbinary disc (CB; a disc shell of matter surrounding the binary in the orbital plane of the system) as an effective means of extracting orbital angular momentum from the binary system. The CB may have been established at an early stage as a result of its formation following the common envelope phase or as a result of mass outflow from the white dwarf or the accretion disc. In this picture, tidal torques due to the gravitational interaction of the disc with the binary are exerted on the CB disc, thus removing angular momentum from the binary orbit inside it. Presuming that some fraction of the mass lost from the donor

star condenses into the CB disc, then a feedback process can operate to elevate the transfer rates above those determined by magnetic braking or gravitational radiation losses acting alone[5]. The evolutionary time for CVs are, therefore, much shorter than in the standard scenario, solving the space density problem. In fact, for high mass input rates into the CB, the secondary can be completely dissolved in less than a Hubble time. Allowing for a range of ages of the systems, masses and evolutionary state of the donor and the existence of a CB disc at the beginning of the binary evolution, this model can reproduce the observed spread of mass transfer rates at a given period but it has difficulties preserving the period gap at the same time.

- Recently, King & Schenker (2002) and Schenker & King (2002) have proposed a radically different approach to CV evolution by postulating that angular momentum loss during the common envelope phase is much less efficient than typically assumed (c.f. Andronov et al. 2003). Consequently, pre-CV binaries exit the common envelope with very wide orbits, and evolve into the semi-detached CV configuration only on very long timescales. Hence, a smaller number of CVs has been produced to date compared to the standard scenario, and the present-day CV population has not yet reached the minimum period. This scenario, dubbed the Binary Age Postulate (BAP), solves both the problem of the minimum period and of the space density, but it does create a new one: it predicts a vast number of pre-CV binaries, as in the case of Andronov et al. (2003)'s empirical angular momentum loss prescription seen above. With only some 30 pre-CVs known (Schreiber & Gänsicke 2003), discovered through a random assortment of techniques, a detailed test of the BAP is currently not possible. The BAP hypothesis also allows a large population of significantly-evolved CVs to coexist with the familiar unevolved CVs assumed in the standard picture. The result are two very different groups of CVs:

[5]The gradual build up of disc mass implies a growing tidal torque and as a consequence an increase on mass transfer rates.

a normal one showing all the phases characteristic of the standard theory of CV evolution and in addition a nuclear evolved group descended from more massive secondary stars (more massive than the primary) via thermal timescale mass transfer phase[6]. Schenker et al. (2002) suggested that the anomalous characteristics of AE Aquari are well-explained in the thermal-timescale mass transfer scenario. Recently, Gänsicke et al. (2003) identified four additional CVs that show strongly enhanced N/C emission line flux ratios, suggesting peculiar abundances of their donor stars. This is the likely hall mark of nuclear evolved stars. Schenker et al. (2002) suggest that many of the thermal-timescale mass transfer CVs have been reduced to the He-rich donors in AM CVn systems (briefly described in Sec. 1.3). The bimodality of CVs formed in both ways naturally provides the spread in mass transfer rates seen in the observed population of CVs.

- In the hibernation scenario proposed by Shara et al. (1986) novae, dwarf novae, and nova-like variables represent cyclical stages in the evolution of the same systems. Following the nova eruption, irradiation of the secondary by the hot white dwarf induces mass transfer long after mass ejection from the binary ends ($\sim$ 100 yr). As the white dwarf gradually cools, the mass transfer rate decreases to very low values and the donor star shrinks to its thermal equilibrium radius, inside the Roche-lobe, slowing down the mass transfer even further, until it stops altogether. The latter stage is caused possibly by a combination of two things: irradiation drives the secondary out of thermal equilibrium as mass transfer timescales are shorter than thermal timescales, and the nova eruption may result in a slight widening of the binary orbit with the consequent increase in the radius of the Roche lobe. During the subsequent (quasi)-detached hibernation phase, the white dwarf has time to cool

[6]In this phase mass transfer is driven on the thermal timescale of the donor star, at rates of $\sim 10^{-7} M_{\odot}\,\mathrm{yr}^{-1}$. Once the secondary/primary mass ratio decreases sufficiently ($q \lesssim 1.25$) thermal timescale mass transfer ends. The system either evolves off to longer $P_{\rm orb}$, driven by nuclear evolution, or switches to stable mass transfer driven by angular momentum losses like ordinary CVs. For a review on stability of mass transfer in binaries see de Kool (1992), particularly their Fig. 2.

and the bottom of its hydrogen envelope will eventually become degenerate (Prialnik & Shara 1986). Once angular momentum loss brings the secondary again into contact with its Roche-lobe, mass transfer resumes, the system emerges from hibernation and a nova eruption follows soon. The high mass transfer rates immediately prior to and following a nova eruption are high enough to suppress disc instabilities, and the system appears as a nova-like variable. During the transitions into and out of hibernation, the mass-transfer rates should be such as to permit dwarf nova outbursts[7]. The hibernation scenario resolves the space density problem by postulating that CVs hide from view during most of the millenia between eruptions. Recently, Schenker et al. (1998) and Kolb et al. (2001) considered the effects of nova eruptions on the evolution of CVs and concluded that the mean mass transfer rate and orbital periods are not continuous functions of time but change discontinuously with every nova eruption by an amount proportional to the ejected envelope mass. In addition, energy and angular momentum can be removed from the orbit owing to dynamical friction of the secondary orbiting in the expanding nova envelope. Nova eruptions can thus lead to a spread of mass transfer rates in systems with similar periods.

2.4 On the search for the missing CVs and Pre-CVs

Whereas a number of additions/alternatives to the standard model have been recently proposed, it is apparent that the disturbing disagreements between theory and observations have a common denominator: the possible impact of selection effects on the currently known population of galactic CVs. In order to quantitatively test any theory of CV evolu-

[7]Schreiber et al. (2000) recently modelled in detail the transition from the nova-like to the dwarf nova phase for V446 Her (Nova Her 1960), showing that irradiation from the hot white dwarf is an essential ingredient suppressing dwarf nova outbursts following the nova eruption.

tion it is necessary to establish a statistically complete sample of this class of binary stars. There are currently a number of large-scale surveys for CVs underway that pursue this aim (e.g. Szkody et al. 2002, uses the Sloan Digital Sky Survey or SDSS). I am involved in two of these CV/pre-CV surveys based in a variety of selection schemes (spectroscopy - using the Hamburg Quasar Survey; X-ray emission and multi-colour - using ROSAT and 2-Mircron All-Sky Survey archival data). This thesis is mainly based on work related to these large-scale searches for CVs and pre-CVs, especially on the study of systems discovered from the Hamburg Quasar Survey.

2.4.1 The Hamburg Quasar Survey

The Hamburg Quasar Survey (HQS; Hagen et al. 1995) is a photographic objective prism survey, covering $\sim 13\,600$ deg^2 in the northern sky ($\delta > 0°$) at high galactic latitudes ($|b| > 20°$) with the primary aim to find bright ($B \lesssim 17.5$) quasars. The observations were taken with the former Hamburg Schmidt telescope, which is located at the Spanish-German Astronomical Center (DSAZ) on Calar Alto/Spain since 1980. The dynamic range of the survey is $13 \lesssim B \lesssim 18.5$ and the spectral coverage is $3400 - 5400$ Å with a resolution of ~ 45 Å at H_γ. Direct Schmidt plates were obtained in addition to the spectroscopic plates to astrometrically identify the objects. Spectroscopic plates were obtained for the majority of all fields during at least two epochs, providing some information on the variability of the objects. All spectra were initially scanned in a low-resolution mode. Blue objects selected from these low resolution scans (see small inserts in Fig. 5.1 and 6.1) were then scanned at the full spectral resolution. The total data base of these high resolution scans contains ~ 50000 objects. These spectra are visually examined to classify the sources into preliminary categories (Hagen et al. 1999). The criteria to select CV candidates from the high resolution HQS spectra is detection Balmer emission or blue continuum plus significant variability ($\Delta V \gtrsim 1.5$ mag; see Fig. 5.1 and 6.1). So far this selection criterion has been used only to a very limited extent, most of the 2-3 dozen spectroscopically

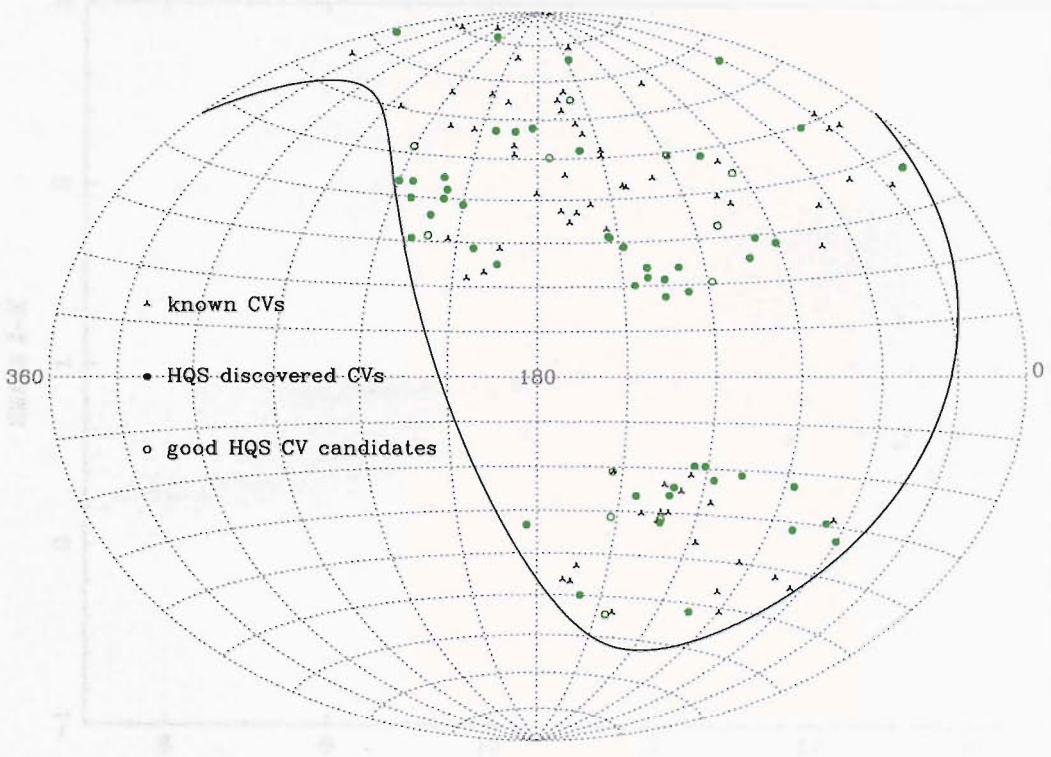

Figure 2.2: Distribution of the HQS-discovered CVs over the sky in galactic coordinates. The HQS covers the northern hemisphere ($\delta = 0°$, indicated by the solid line) and galactic latitudes $|b| > 20°$.

discovered CVs stem from the first and second Byurakan surveys (see e.g. Stepanian et al. 1999).

At the present time, 52 CVs and one likely pre-CV have been discovered, and 36 very promising CV candidates await spectroscopic confirmation (e.g. Gänsicke et al. 2000; Nogami et al. 2000; Gänsicke et al. 2002b,c,; see Fig. 2.2). In Chapters 5 and 6 I present a detailed analysis of the follow up observations from two of the CVs discovered in the HQS: 1RXS J062518.2+733433, a new IP with an orbital period of 4.85 h and HS 2331+3905, an unique CV with an orbital period of 81.08 min and a dominant radial velocity periodicity which is incoherent but persistent over three years.

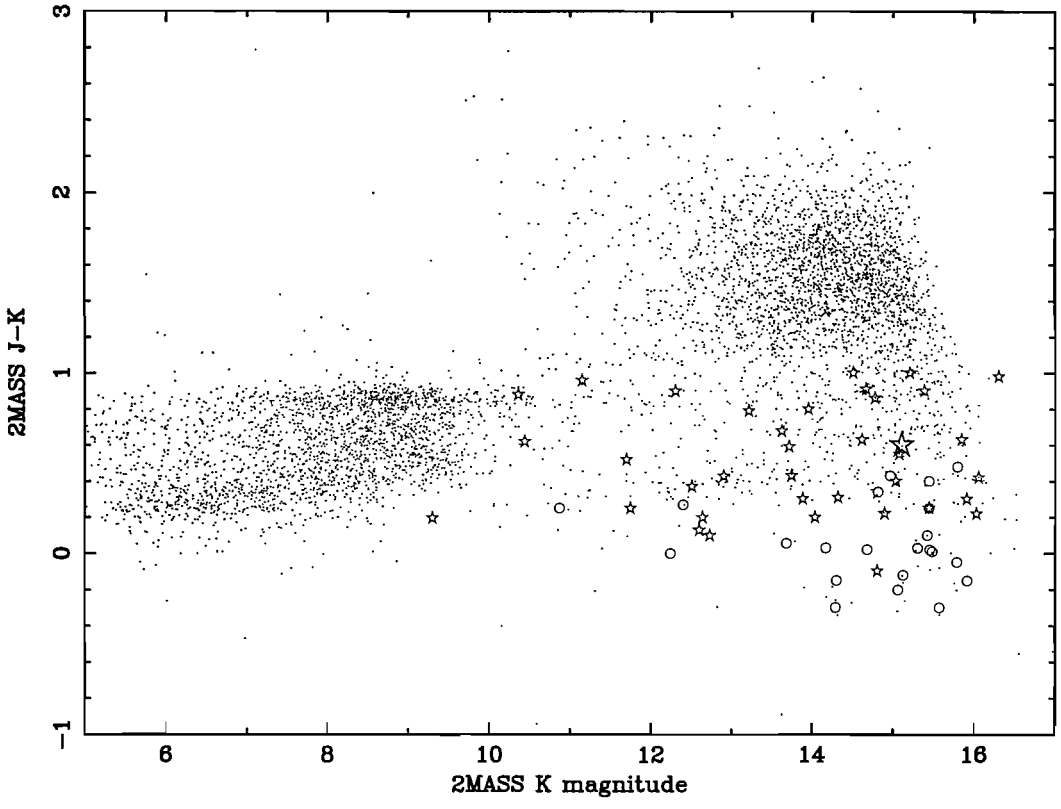

Figure 2.3: The 2MASS "magnitude-colour" diagram of stellar sources from the RASS, showing how infrared colours distinguish CVs and white dwarfs from other sources. Bright stars appear towards the left, while AGN appear in the upper-right. Known white dwarfs are marked by circles, known CVs by stars.

2.4.2 A combination of ROSAT and 2-Micron All-Sky Survey

In a parallel program aimed to discover weakly X-ray emitting CVs, a combination of ROSAT All-Sky Survey (RASS) archival data, optical (B and R), and 2-Micron All-Sky Survey (2MASS) colours (R, J and K),was used to select possible candidates. The following limitations were applied to help in the selection process and in order to discriminate against active M-stars and AGN which comprise the majority of the sources: the selected sources have X-ray count rates from 0.05 to 0.2 counts/sec, a regime not systematically explored before; to avoid confusion only sources with galactic latitude $|b| > 5°$ were chosen; for practical reasons (detectability in follow up observations) $R < 17$; infrared

colours were used to remove AGNs and active stars from the list of possible candidates by selecting only those objects with $K > 11$ and $J - K < 1.0$, see Fig. 2.3. From over 10 000 sources, 250 unidentified targets remain. Positive identification is then possible by their optical spectroscopic appearance: relatively strong Balmer and helium emission lines.

Chapter 3

Reduction Techniques

The main aim of our photometric and spectroscopic observations is to detect variability in the light received from the object under study. Specifically, we search for variability associated with the changing geometry of the system as the binary rotates around its centre of mass or as the white dwarf spins. Fig. 7.2 (bottom panel) illustrates an example of photometric variability: in a high-inclination CV, the dim (cool) secondary star will eclipse the bright (hot) accretion disc and/or the white dwarf. The spectroscopic variations observed in spectral lines are due to the Doppler-shifts corresponding to the motion of the absorbing or emitting material within the binary. Most commonly, these Doppler shifts directly trace the orbital motion of the absorbing/emitting component.

Detailed time-resolved observations of the spectroscopic and/or photometric variability of a CV can be used to constrain the parameters of the system. The most important of these parameters (in the context of our study of CV evolution) is the orbital period. Determining this parameter for a complete sample of CVs, such as e.g. the HQS CVs, will help us to overcome the likely statistical incompleteness of the orbital period distribution

and hence will improve our understanding of the evolution of CVs.

Due to the extent of the programs I have been involved with, most of the work presented in this thesis is part of a team effort. The majority of the optical spectroscopic data have been collected, reduced and calibrated by myself as well as most of the photometry acquisition; however reduction and analysis of the photometry has been performed by B. Gänsicke.

In what follows, I outline the general principles involved in reducing the data, focusing on the techniques applied to the observations presented here. I leave the description of the instruments used to gather the data as well as details of the observing runs to the relevant chapters.

3.1 Ground based observations

These data comprise time-resolved CCD photometry obtained mostly at the Kryoneri Observatory and at the 2.2 m Calar Alto telescope, and time series spectroscopy obtained mainly at the Isaac Newton Telescope (INT) in La Palma and again at the 2.2 m in Calar Alto. All of the data were obtained using charge-coupled device arrays (CCDs). The aim in reducing such data is to translate the two-dimensional data recorded by such an array into either one-dimensional data in the case of spectroscopy (i.e. a spectrum), or zero-dimensional data in the photometric case (i.e. a magnitude).

3.1.1 CCD data reduction

In order to extract useful information from these two dimensional images we must correct for any instrumental effects related to the way that a CCD detector operates. This is

a common procedure applied to practically all CCD datasets, whether photometric or spectroscopic. The standard way of reducing CCD images consists of the removal of the bias level and dark current (if necessary) and the correction for sensitivity variations across the chip.

3.1.1.1 Bias removal

The bias (or zero level) is a base count rate electronically added to the detector output signal to avoid negative values in the readout process (i.e. when converting the measured analogue voltage into a digitized sum of counts).

This bias level is in general subject to spatial and temporal variations. The temporal variations can be accounted for by using the data in the overscan region of the CCD image, a number of columns which are not exposed to light. The counts for each of these columns are averaged to estimate the bias level for each readout row. If the variations between rows is small then an average bias level may be used. If, on the other hand, the variations are significant, then a low-order polynomial or spline function is fitted to avoid introducing unwanted noise into the image[1]. The result is then subtracted from all the frames, including calibration frames. To correct for the two-dimensional bias structure (the spatial variation), a set of images of zero exposure time with the shutter close are obtained. These images once bias-subtracted as above, are combined together to obtain a mean zero frame. This zero image can be finally subtracted from all the frames. We need a large number of zero frames to avoid introducing noise into the images.

[1]The overscan region does not contain enough columns to smooth out the noise by calculating the average.

3.1.1.2 Dark count subtraction

In general, CCDs are subject to a dark current due to the thermal noise in the detector, which is proportional to exposure time. This dark current can in principle be removed by taking exposures with the shutter closed and with the same exposure time as the images to be corrected. In practice, this effect is almost negligible in most CCDs since they are cooled down to very low temperatures. None of the spectroscopic datasets considered in this thesis were corrected by dark current as in all of them it proved to be insignificant. The only detector used in this project that has a significant dark count rate is the CCD camera at the 1.2 m Kryoneri telescope. The data obtained with this instrument were accordingly dark-subtracted before further processing.

3.1.1.3 Flat-fielding

The pixels of a CCD detector do not have the same response to a constant flux of light. In addition, there is the problem of uneven illumination. This latter effect can be caused by dust either on the CCD surface itself, on the filter of a CCD camera or on the slit of a spectrograph and could be time-dependent. Vignetting (shadowing) from the optics can also cause uneven illumination, but on a larger scale. To correct for these effects, we need to take images of a source of light with a homogeneous light distribution (hence the terminology flat-field), such as an illuminated screen in the dome, or the twilight sky. In both cases the flat-field images should be taken with the same instrumental setup as the science frames, and ideally they should be taken often enough to account for a possible time-dependence. In practice this is not always possible and flat-fields are taken either before and/or after the observing night.

Independently of how individual frames are acquired, a mean flat-field frame is usually derived from several independent exposures via averaging (after bias-subtracted). The

mean flat-field frame is then scaled to a mean of unity with small deviations from unity reflecting the response variation on the pixels. The object frame is simply divided by this frame.

3.1.2 Differential photometry

Since our main interest is to measure brightness variations, we perform time-series differential photometry. Here, the photometric measurements are made with respect a comparison star. In practice, several comparison stars are chosen within the same CCD frame as the object under observation. This will ensure they are subject to the same atmospheric conditions and the same airmass. By selecting more than one comparison in the field one can check if any of then is variable (which would give erroneous results). The technique used to obtained the photometric data from the CCD images is aperture photometry.

3.1.2.1 Aperture photometry

In what follows it is assumed that the CCD images being operated on have already been reduced as described in the previous section (i.e. bias and dark subtracted and flat-fielded). Aperture photometry involves placing a virtual aperture (usually circular) around the target and adding up the counts inside it after subtracting the sky background contribution. The sky contribution per pixel is given by the median of the counts contained in an annulus well separated from the aperture of the target. The choice of the photometric aperture has to be done with care. A large aperture will collect virtually all the signal from the target but it will also include a large amount of sky light, therefore increasing the random errors from the flux of the star. A smaller aperture will decrease the random errors (less sky contamination) but some of the star signal will fall outside. In this case, the result will be subject to a systematic error due to under or overestimating the loss of signal outside

the aperture, and a decrease in the signal to noise ratio (as this is proportional to the square root of the number of counts). The photometric reduction used in this project adjusts the aperture size for each individual image according to the median seeing measured from that image.

3.1.3 Long-slit spectroscopy

3.1.3.1 Spectral extraction

One-dimensional spectra are generally extracted, from the reduced target frames using the optimal extraction method of Horne (1986). Essentially, this method uses a fit to the spatial profile containing the stellar flux to weight each pixel contribution in order to maximize the quality of the derived spectrum. Before the extraction itself we must follow several previous steps. If the dispersion direction is not parallel to the CCD x- or y-axis, we must trace it by fitting a polynomial function to the dispersion direction. We then define an extraction aperture for the target by collapsing the traced spectrum onto the spatial direction. The spectral image is corrected for the sky background contribution by fitting polynomials to the selected sky regions in the spatial direction and evaluating them in the object region. The sky contribution can then be subtracted from the spectral image. The spatial profile is derived as described by Marsh (1989) to estimate the optimal weight of each of the pixels within the selected object aperture. The spectrum is finally extracted by summing the weighted pixel contribution over the spatial profile to yield a value for each element in the dispersion direction. The algorithm used here is also capable of eliminating cosmic rays and bad pixels from the spectrum by detecting the distortion they produce in the spatial profile.

3.1.3.2 Wavelength calibration

Wavelength calibration of the extracted spectrum requires a defining correspondence between pixel number and wavelength. However, this correspondence changes with time due to instrumental flexure as the telescope moves across the sky. An accurate wavelength calibration, therefore, requires careful monitoring of this time dependence. This involves observations of calibration arc spectra obtained repeatedly during the observing run, ideally every 30 minutes. The idea is to identify a large number of arc lines to determine a correspondence between wavelength and pixel position by a low order polynomial fit for each arc spectrum. Finally, the wavelength scale of each target spectrum is interpolated from the wavelength scales of two neighboring arc spectra.

3.1.3.3 Flux calibration

The aim here is to convert the ordinate scale of the object spectra from rather anonymous counts to physical flux units. This involves up to three possible steps. (1) Correct for the instrumental response, (2) correct for the atmospheric extinction, and (3) avoid slit losses. To accomplish this delicate task, spectra from flux standards obtained with the same instrumental setup, including the same slit width, should be obtained as close as possible in time and airmass to the target spectrum.

The wavelength-dependent sensitivity of the entire spectrograph is called the instrumental response, which is made up of a combination of the reflectivity/transmission of the various optical elements, as well as of the quantum efficiency of the CCD detector. The likewise wavelength-dependent atmospheric extinction is primarily related to the fact that blue light suffers stronger scattering than red light. The detailed run of the atmospheric extinction can change quite dramatically depending on the atmospheric conditions, e.g. dust in the atmosphere will result in an increased reddening of the observed spectrum. In

MOLLY, the reduction package used for the spectroscopic data in this project, the combined instrumental response function and wavelength-dependent atmospheric extinction is obtained by comparison of tabulated spectral energy distribution (SED) of the flux standard with the actual observed flux standard SED. Specifically, the ratio of the observed SED to the tabulated one is computed. After masking out spectral lines, a polynomial or spline is fitted to this ratio as a function of wavelength. The end product is the response function. If the airmass of the target and flux standard stars are the same, then the response function could be applied as it stands to the target star. If, on the other hand, both stars have different airmasses, then a correction for this difference must be applied.

Possible sources of error in the flux calibration are incorrect atmospheric extinction (due to the target and the flux standard being observed at very different times) and differential slit losses. As already mentioned, if the amount of dust or aerosols changes between the flux standard and target observations, the wavelength-dependence of the atmospheric extinction will change, and consequently the slope of the calibrated target spectrum will be wrong. In addition, the refraction of the light from the star is wavelength-dependent. As a result, the image of the star on the slit is not circular, but elongated, and depending on the slit width and angle part of the stellar flux is lost. In many telescopes the TV guider used to centre the star on the slit is red-sensitive, so that it is almost unavoidable that the red end of the stellar spectrum is centred on the slit, and blue light is lost. The direction parallel to this dispersion is called the parallactic angle. We can avoid differential slit losses by aligning the slit parallel to this angle, and hence parallel to the atmospheric dispersion. This effect becomes stronger with increasing zenith distance. In principle, differential slit losses could be corrected for if the standard star was observed at the same time as the target or in the same conditions (i.e. same zenith distance and slit angle with respect to atmospheric dispersion). If this were not the case, flux calibration of data suffering from this effect would produce an incorrect spectral shape.

3.2 Space observations

Space observations were used for two of the objects presented in this thesis: DW UMa (Chapter 4) and HS 2331+3905 (Chapter 6). In both cases long-slit far-ultraviolet (FUV) spectroscopy was obtained with the Space Telescope Imaging Spectrograph (STIS), using a multi-anode microchannel array (MAMA) detector, on board of the Hubble Space Telescope (HST).

The observations of DW UMa were obtained by C. Knigge and collaborators with the aim of improving the situation on the understanding of a type of nova-like variable CVs called SW Sex stars (see Sec. 1.3). In the case of HS 2331+3905, the observations are part of an ongoing program led by B. Gänsicke to survey CVs in the FUV. The observations are carried out as "snapshots", gaps in the HST schedule that cannot be filled with regular observations.

MAMA detectors are photon counting detectors. They differ from CCDs mainly in that they do not suffer from cosmic rays or read noise. These detectors can operate either in TIMETAG mode, in which the position and detection time of every photon is recorded (as in the case of DW UMa data), or in ACCUM mode, to produce a time-integrated image (as in the case of HS 2331+3905 data). Doppler correction for the spacecraft motion up to 7.5km/s is applied automatically on-board for data taken in ACCUM spectral resolution modes and during ground processing for TIME-TAG mode data. An internal calibration lamp observation (wavecal) is taken every 40 min in order to allow calibration of the zero point of the wavelength (dispersion) and spatial (cross dispersion) axes in the spectroscopic science data during post observation data processing.

The reduction of STIS/MAMA data is carried out, as with all of the HST instruments, through a pipeline, the STIS-specific one being CALSTIS. Briefly, the reduction steps are similar to those described for a CCD above, except for the bias removal. The shift

in the dispersion direction is found by cross-correlating the observed wavecal spectrum with a template spectrum. In the cross dispersion direction or spatial direction, edge location is used to obtain the shift. The science image is then corrected using these values. A one-dimensional spectrum is extracted along a narrow band, summing in the cross-dispersion direction (non-weighted sum) and subtracting nearby background values. Flux calibration is also applied during pipeline extraction. Flux standards are observed roughly on a monthly base to monitor the instrumental response. As HST is above the earth atmosphere, (variable) atmospheric extinction is no issue for STIS data.

Chapter 4

DW UMa: a SW Sex Star with VY Scl Behaviour

4.1 Introduction

The subject of this chapter, DW Ursae Majoris, is an eclipsing nova-like variable CV with a period of $P_{\rm orb} = 3.28$ h which exhibits the low states characteristics of VY Scl stars. In addition, DW UMa belongs to the subclass of nova-like variables called SW Sextantis stars (Thorstensen et al. 1991). Refer to Sec. 1.3 for a description of this type of objects.

One reason for our poor understanding of the SW Sex phenomenon is the scarcity of reliable system parameters for members of this class. This scarcity is a direct consequence of the defining SW Sex characteristics. More specifically, radial velocity studies of SW Sex stars are of limited value, given the ubiquitous and significant phase lags seen in the radial velocity curves of these systems. Eclipse studies have been similarly unsuccessful, since white dwarf contact points are not evident in the V-shaped eclipse light

curves of SW Sex stars (perhaps because the discs are self-occulting; Knigge et al. 2000). Also, the high accretion rates exhibited by these systems during normal states cause the late-type main sequence secondary to be invisible against the glare of the white dwarf and/or accretion disc.

In this chapter, a set of reliable system parameters for DW UMa is derived in an attempt to improve this situation. This is possible because a recent HST observation of the system found DW UMa in a deep low state, during which the white dwarf dominated the far-ultraviolet (*FUV*) light. This same data was used in Knigge et al. (2000) to report the low-state *FUV* spectrum. Here I analyze the time-resolved behaviour around the eclipse and discuss *I*- and *K*-band photometry obtained during the same low state. The remainder of this chapter is organized as follows: the observations are described in Sec. 4.2. In Sec. 4.3 I discuss our determination of the contact phases describing the eclipse of the white dwarf by the secondary. In Sec. 4.4 I use the contact phases and other information to determine the parameters of the binary system and its constituents. Then, in Sec. 4.5, I calculate estimates for the distance to DW UMa and for the spectral type of the donor star in two different ways: using our *I*- and *K*-band photometry and re-fitting the Knigge et al. (2000)'s white dwarf model atmosphere to the low-state *FUV* spectrum of DW UMa. Finally, in Sec. 4.6, I discuss our results and compare the system parameters we have derived to those previously reported for DW UMa, and in Sec. 4.7 I give a brief summary of the results presented here.

4.2 Observations

The observations of DW UMa with the HST/STIS took place on 1999 January 25 UT and covered just over two complete cycles of DW UMa's 3.28 h orbital period. DW UMa is located in HST's continuous viewing zone (CVZ), so the observations were interrupted

only three times for short ($\simeq$ 6 minutes) wavelength calibrations. The instrumental set-up consisted of the $52'' \times 0.2''$ slit, the FUV-MAMA detectors, and the G140L grating. This combination provides a wavelength coverage of $1150 - 1720$ Å at a resolution of $\simeq 1$ Å (FWHM). TIME-TAG mode was used throughout, so that individual photon arrival times were recorded at a sampling rate of 125 μs.

Near-simultaneous optical photometry obtained from the MDM Observatory on Kitt Peak, Arizona, shows DW UMa at $V \simeq 17.6$ around the time of the HST observations. The data indicate that the system was in a deep low state at this time ($V \simeq 14.5$ in the high state). Given that the accretion rate must be severely reduced during a low state, the hot white dwarf primary may be expected to dominate the FUV light in this state. Indeed, Knigge et al. (2000) have already used the same data set to show that the low-state, out-of-eclipse FUV spectrum of DW UMa is consistent with that of a hot white dwarf. Our FUV eclipse observations therefore provide us with an unusual opportunity to determine the white dwarf contact phases (and therefore system parameters) of this eclipsing SW Sex star.

For the purpose of the eclipse analysis, we constructed light curves directly from TIMETAG files. These files contain a list of the arrival times and detector positions of all recorded photon events, and are therefore ideally suited for short-timescale variability studies. Since we wanted to exclude geocoronal and other strong lines from our light curves, we first determined an approximate linear dispersion relation to relate pixel numbers in the dispersion direction with physical wavelengths. Light curves were then constructed at 1-s time resolution, based on all counts recorded in three continuum windows in the dispersion direction, *viz.* 1340 – 1380 Å, 1410 – 1520 Å and 1570 – 1720 Å (see Fig. 4.1), and in a 0.36 arcseconds window in the spatial direction. Since we are only interested in determining contact phases, the zero-level of the light curves is irrelevant. We therefore did not carry out any background subtraction on our light curves. The background is, in any case, expected to be negligible: our continuum regions are well sep-

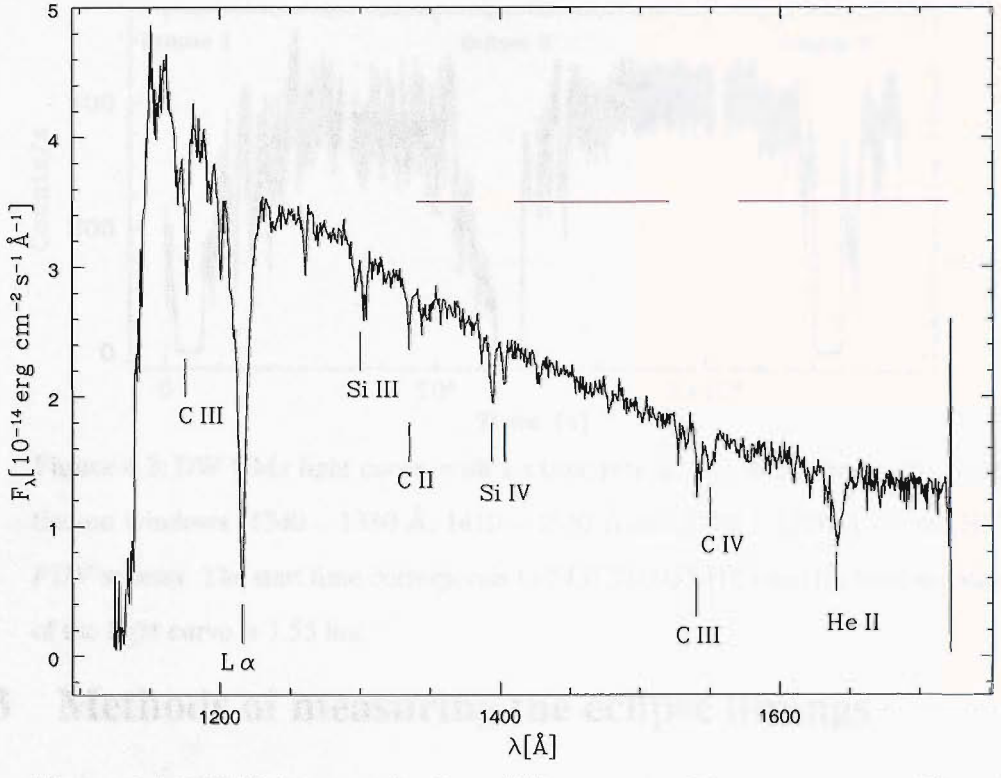

Figure 4.1: DW UMa's out-of-eclipse UV spectrum. The strongest transitions in the white dwarf-dominated low state spectrum are indicated. The red lines mark the wavelength ranges used to construct the light curve of Fig. 4.2, i.e. 1340 – 1380 Å, 1410 – 1520 Å and 1570 – 1720 Å.

arated from geocoronal lines, and dark current contributes only about 7 c/s across the entire FUV-MAMA detector, and therefore less than 0.1 c/s in the small region used for extracting the count rate.

Figure 4.2 shows the resulting *FUV* light curve of DW UMa. Several points should be noted: (i) the count rate at mid-eclipse phases is close to zero, confirming that there is no significant background contribution in our light curves; (ii) there are sharp features in each of the eclipses (especially eclipse 3), which are likely due to ingress and egress of the white dwarf; (iii) the light curves exhibit substantial short-timescale, stochastic variability.

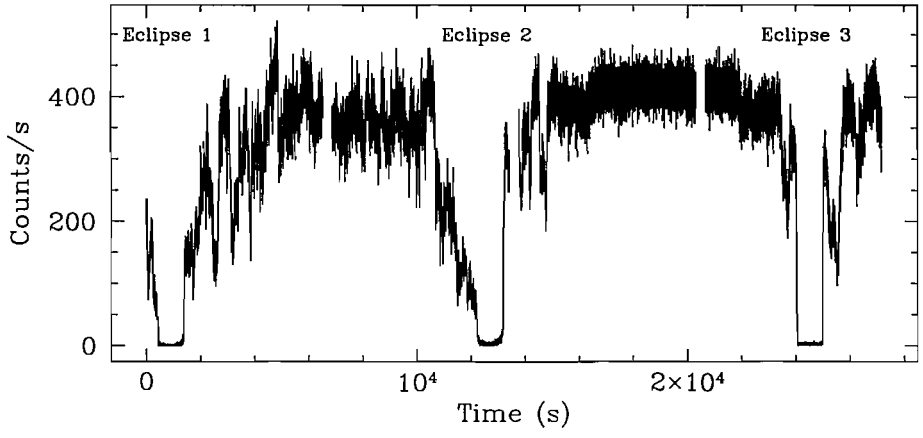

Figure 4.2: DW UMa light curve, with 1 s time resolution, constructed from 3 continuum windows (1340 – 1380 Å, 1410 – 1520 Å and 1570 – 1720 Å) of the HST *FUV* spectra. The start time corresponds to 2451203.933 HJD and the total duration of the light curve is 7.55 hrs.

4.3 Methods of measuring the eclipse timings

In order to convert the HJD times to orbital phases, we used the ephemeris

$$T_{\mathrm{mid-eclipse}} = 2446229.00696(3) + 0.136606499(3)E, \tag{4.1}$$

where the numbers in parentheses designate the errors on the last digits. This is an updated version (Smith et al. 2002) of the ephemeris presented by Dhillon et al. (1994). In practice, we still found an O-C shift of approximately +0.0062 (73 s) with this new ephemeris. This is consistent with that found by Smith et al. (2002) from a high state of DW UMa observed at a similar epoch to ours. Note that our O-C shift, which has been removed in all of the phase-folded light curves shown below, could include a contribution of a few seconds from the uncertainty in the STIS absolute timing (see Long 2000).

The phase intervals inside which the white dwarf disappears (ingress) and reappears (egress) from behind the occulting secondary are defined as $\Delta\phi_{\mathrm{wi}} = \phi_{\mathrm{w2}} - \phi_{\mathrm{w1}}$ for ingress, and $\Delta\phi_{\mathrm{we}} = \phi_{\mathrm{w4}} - \phi_{\mathrm{w3}}$ for egress, where ϕ_{w1}, ϕ_{w2}, ϕ_{w3} and ϕ_{w4} are the white dwarf contact phases (c.f. Fig. 4.3). The half-flux phases within each of these intervals, ϕ_{wi} and ϕ_{we}

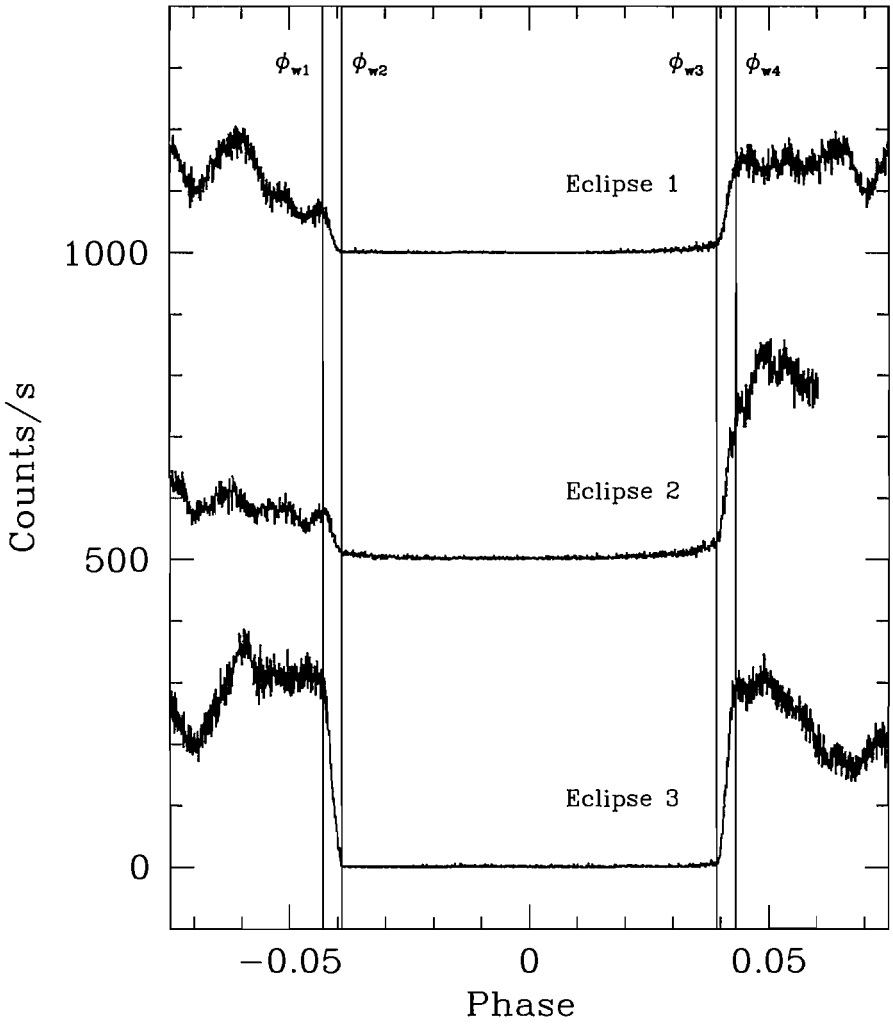

Figure 4.3: The three individual eclipses of Fig. 4.2 plotted against orbital phase. Eclipse 2 and 1 are offset upward by 500 and 1000 counts/s respectively. The vertical lines mark the locations of the contact phases (ϕ_{w1}, ϕ_{w2}, ϕ_{w3} and ϕ_{w4}) inferred from eclipse 3 (see Fig. 4.4).

respectively, are the phases at which half of the light from the compact object is eclipsed. The full-width at half out-of-eclipse intensity is then defined as $\Delta\phi = \phi_{we} - \phi_{wi}$, or, in units of time, $\Delta t = P_{orb}\Delta\phi$.

The white dwarf contact phases were measured using the method described by Wood et al. (1985). Figure 4.4 illustrates this procedure carried out on eclipse 3. The light curve

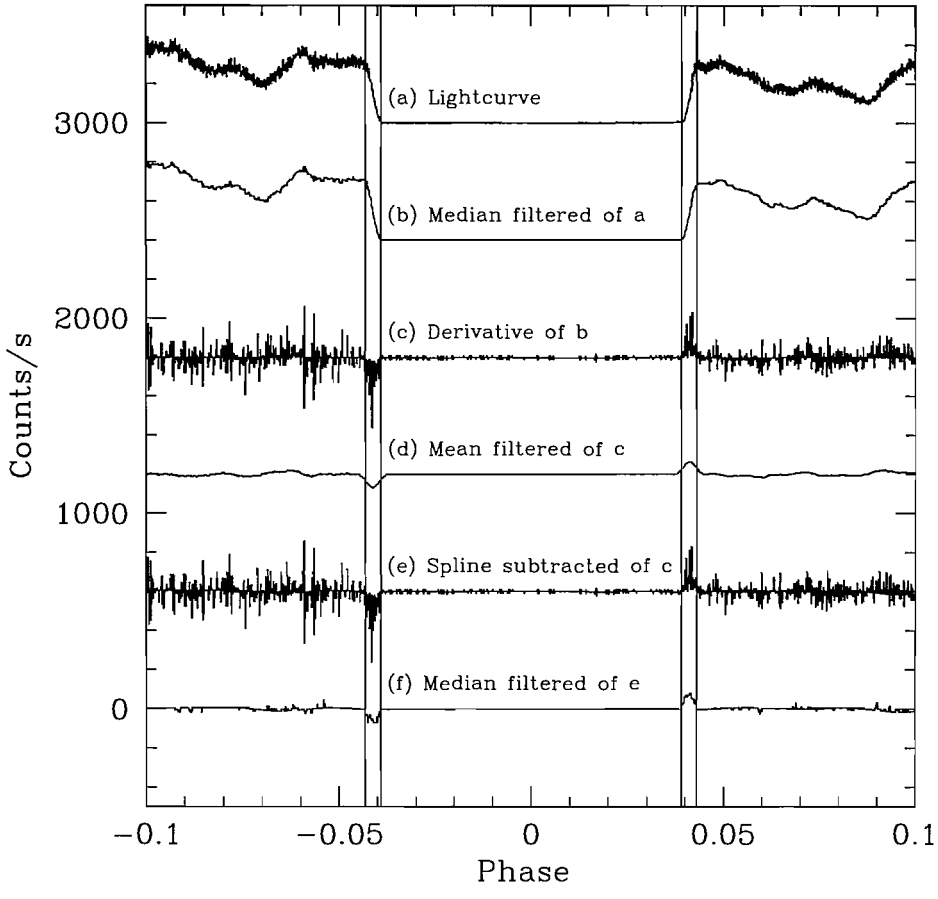

Figure 4.4: Illustration of the method used to obtain the contact phases from eclipse 3 of the light curve of DW UMa. Curves (a) - (e) were successively displaced upward by 600 counts/s each from curve (f). Curves (c), (d), (e) and (f) have been multiplied by a factor of 10 s for clarity. (a) Original light curve with 1 s time resolution. (b) Median-filtered light curve (filter width 11 s). (c) Derivative of the median-filtered light curve. (d) Mean-filtered derivative (filter width 43 s). The highest negative and positive points in this curve indicate the location of the mid-points of ingress and egress respectively, (i.e., ϕ_{wi} and ϕ_{we}). (e) Result of the spline fit and subtraction from the derivative light curve. (f) Median filtered version of (e) (filter width 11 s). The vertical lines represent the measured positions of the contact points ϕ_{w1}, ϕ_{w2}, ϕ_{w3} and ϕ_{w4}.

is smoothed with a median filter of width 11 s. The amount of filtering chosen is a compromise between the desire to reduce the noise (Poisson plus intrinsic variability) and the need to retain the most rapid changes in the eclipse. The smoothed light curve is differentiated numerically to enhance regions of sharp brightness variations. The derivative light curve is then smoothed by applying a mean filter of width equal to the expected value for the times of ingress and egress of the white dwarf (43 s). The largest negative and positive peaks after application of the mean filter indicate the location of the mid-points of ingress and egress respectively. The width at half-peak intensity of these features gives a rough estimate of their duration. A spline function is fitted to the derivative omitting those points inside the estimated ingress and egress intervals. This last step is carried out to account for the contribution (if any) of the extended and slowly varying eclipse of the disc. The fitted function is then subtracted from the derivative, and the result is smoothed with a median filter of width equal to the median filter used in the first part of the reduction. The contact phases are located by identifying the points where the resultant derivative departs from zero.

The main difficulty in identifying the white dwarf contact phases is the presence of stochastic variability on timescales that are only slightly longer than the duration of white dwarf ingress/egress. Figures 4.2 and 4.3 show that this type of variability severely limits our ability to determine white dwarf contact phases for eclipses 1 and 2, in particular. We therefore did not use these two eclipses for measuring the contact points, but only to provide qualitative checks on the contact phases determined from eclipse 3. Figure 4.3 confirms that the contact phases derived from eclipse 3 are indeed consistent with eclipses 1 and 2. The final value for the duration of the ingress/egress of the white dwarf is $\Delta\phi_{wd} = (\Delta\phi_{wi} + \Delta\phi_{we})/2$. In units of time, this is $\Delta t_{wd} = P_{orb}\Delta\phi_{wd}$. Our final estimates of Δt and Δt_{wd} are listed in the first section of Table 4.1.

Table 4.1: Parameters inferred from the eclipse analysis of DW UMa.

Parameter	Value
Eclipse Measurements	
$\Delta t\ (s)$	969 ± 4
$\Delta t_{wd}\ (s)$	48 ± 3
Fundamental constraints	
$q\ (M_2/M_1)$	> 0.24
$M_1\ (M_\odot)$	$0.67 \leq M_1 \leq 1.06$
$R_1\ (R_\odot)$	$0.008 \leq R_1 \leq 0.014$
$M_2\ (M_\odot)$	> 0.16
$R_2\ (R_\odot)$	> 0.28
$a\ (R_\odot)$	> 1.05
With $q < 1.5$	
$q\ (M_2/M_1)$	$0.24 \leq q \leq 1.5$
$M_1\ (M_\odot)$	$0.67 \leq M_1 \leq 0.96$
$R_1\ (R_\odot)$	$0.009 \leq R_1 \leq 0.014$
$M_2\ (M_\odot)$	$0.16 \leq M_2 \leq 1.44$
$R_2\ (R_\odot)$	$0.28 \leq R_2 \leq 0.62$
$a\ (R_\odot)$	$1.05 \leq a \leq 1.50$
i (degrees)	> 71
With M_2-P_{orb} relation	
$q\ (M_2/M_1)$	0.39 ± 0.12
$M_1\ (M_\odot)$	0.77 ± 0.07
$R_1\ (R_\odot)$	0.012 ± 0.001
$M_2\ (M_\odot)$	0.30 ± 0.10
$R_2\ (R_\odot)$	0.34 ± 0.04
$a\ (R_\odot)$	1.14 ± 0.06
i (degrees)	82 ± 4

4.4 Binary parameters

The mass ratio, $q = M_2/M_1$ (M_1 and M_2 are the masses of the white dwarf and secondary, respectively), and inclination, i, of the system can be constrained by considering the eclipse of a point source by a Roche-lobe-filling secondary. More specifically, the observed eclipse duration ($\Delta\phi$) defines a unique relation between q and i. This relation is calculated using a code written by Christian Knigge which is based in a method similar to Chanan et al. (1976). Following their Fig. 1, we define a spherical coordinate system centered on the white dwarf, in which the direction vector (θ,ϕ) = (90°,0°) points towards the centre of the secondary. The main idea is to consider the intersection of the secondary's Roche lobe and the plane $\phi = \Delta\phi/2$. This reduces the problem to finding the minimum value of θ along the curve defined by this intersection. For each q, this minimum value is then just the inclination i that produces an eclipse of width $\Delta\phi$. The method requires the critical value of the Roche potential. This is calculated by using the fact that the net effective force vanishes at the inner Lagrangian point; $\partial\Phi/\partial x = 0$ at L_1 (see Sec. 1.2.1). The q vs i relation for our measured $\Delta\phi$ is shown in Fig. 4.5.

The mean duration of the ingress and egress features of the eclipse ($\Delta\phi_{\rm wd}$), together with the calculated numerical relation $i = f(q, \Delta\phi)$, can be used to constrain the remaining binary parameters. In practice, we use the full Roche lobe geometry of the secondary to obtain the radius of the spherical compact primary. For each (i, q) pair, our algorithm (a code written by Tom Marsh) computes the radius of the white dwarf scaled to the binary separation, R_1/a, that successfully reproduces the observed value for $\Delta\phi_{\rm wd}$. The white dwarf is assumed to be fully visible; this is appropriate here, since there is no evidence for an optically thick disc in the low state.

Kepler's third law, which defines the binary separation, a (see Eqn. 1.3), is then combined with a theoretical white dwarf mass-radius relation to yield a definite white dwarf mass, M_1, for each q. The inset in Fig. 4.6 shows the resulting constraints on the compo-

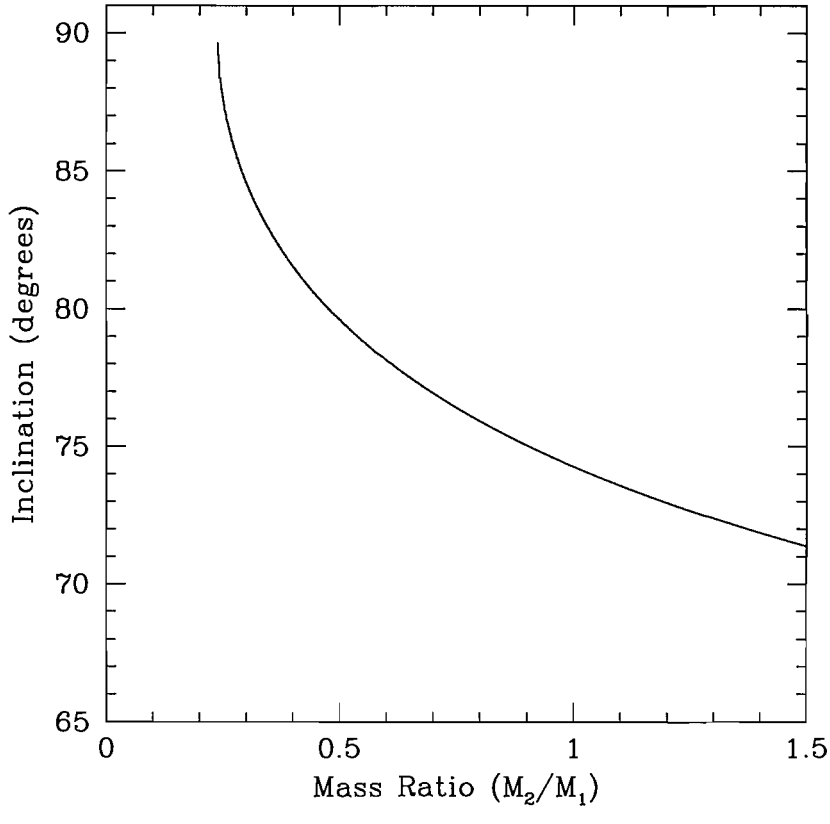

Figure 4.5: Orbital inclination, i, as a function of mass ratio, q. Note that the uncertainty limits on the q vs i relation were not plotted as they were negligible compared to the scale of figure.

nent masses for a wide range of mass ratios.

Finally, we use Eggleton (1983)'s approximation, Eqn. 1.1, to estimate the volume-averaged radius of the secondary, R_2.

The theoretical white dwarf mass-radius relation that we use was taken from Panei et al. (2000) and describes hot ($T_{\rm eff} = 50\,000$ K) CO-core white dwarfs with a relatively massive, non-degenerate hydrogen envelope ($M_{\rm env}/M_1 = 10^{-5}$). The effective temperature adopted here is close to the value (46 000 K) inferred by Knigge et al. (2000) from a white dwarf model atmosphere fit. For reference, the spectrum analyzed by Knigge et al. (2000) was constructed from the time interval between eclipses 2 and 3, when the

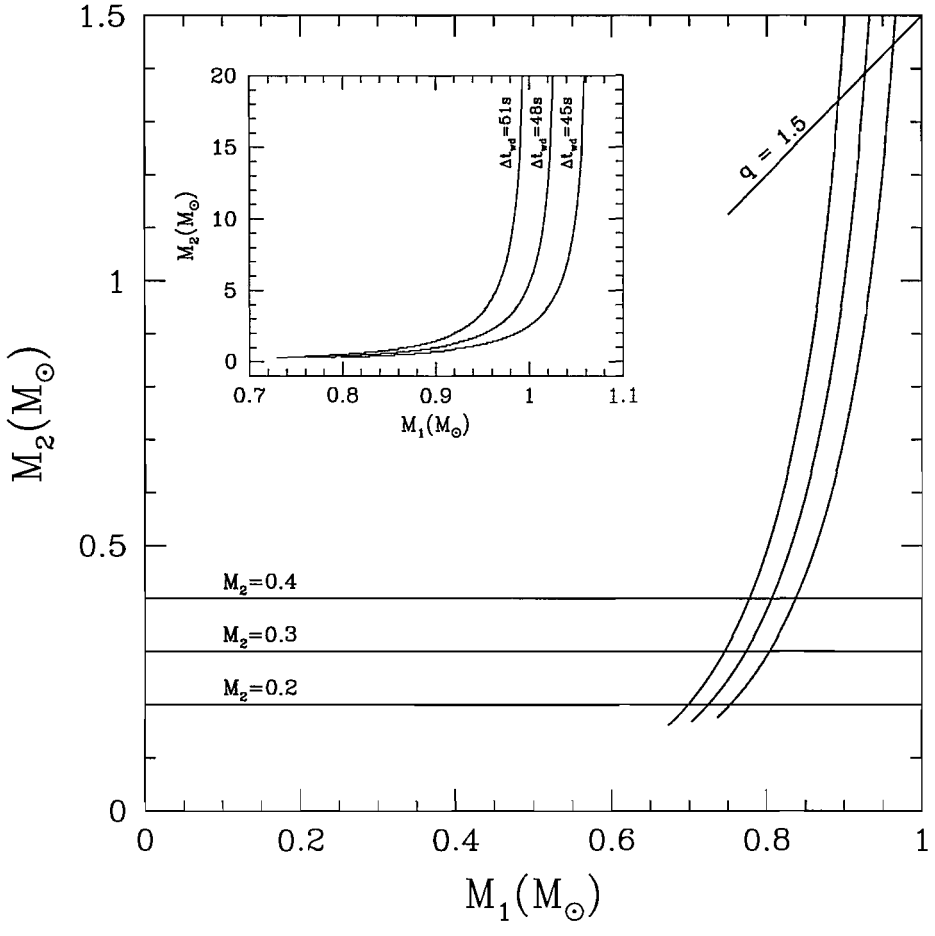

Figure 4.6: Constraints on the component masses of DW UMa. The three curves in both plots correspond to $\Delta t_{wd} = 45$ s, 48 s and 51 s. The inset shows a larger range of values for M_2 so that the fundamental upper limits on M_1 can be clearly seen. The $q = 1.5$ line on the main plot shows the upper limits on the component masses based on theoretical grounds (see text). The horizontal lines represent the value of $M_2/M_\odot = 0.3 \pm 0.1$ obtained from the $M_2 - P_{orb}$ relation of Smith & Dhillon (1998). The corresponding value for the mass of the white dwarf is $M_1/M_\odot = 0.77 \pm 0.07$.

count rate was high and relatively stable. We used a slightly higher temperature here, because our analysis indicates a higher surface gravity ($\log g$). More specifically, preliminary parameters inferred with a $T_{eff} = 46000$ K mass-radius relation yielded white dwarf parameters corresponding to $\log g \simeq 8$. As discussed in more detail in Sec. 4.5, we then

refit the low-state *FUV* spectrum with this new gravity estimate and obtained a new temperature estimate of $T_{\rm eff} = 50\,000$ K. We note that the systematic errors associated with the presence or absence of a hydrogen envelope and with errors in temperature up to at least 10 000 K are smaller than the random errors resulting from observational uncertainties. Hence, the iteration process does not change the parameter values substantially, but merely improves their internal consistency.

At this stage, we can already place useful constraints on most of the system parameters, which are listed in the second section of Table 4.1. These constraints are only based on the eclipse geometry and the theoretical white dwarf mass-radius relationship and are therefore particularly robust. If the mass ratio is made to satisfy $q < 1.5$ (see Fig. 4.6), as required for stable mass-transfer from any main-sequence secondary (Politano 1996; de Kool 1992), the constraints are tightened, as shown in the third section of Table 4.1.

If we are willing to assume that the secondary star is "typical" for a CV with DW UMa's orbital period, we can tighten our constraints even further by using Smith & Dhillon (1998)'s mass-period relationship for CV secondaries. The resulting estimate for the mass of DW UMa's secondary is $M_2/M_\odot = 0.3 \pm 0.1$, where the error is based on the rms scatter quoted Smith & Dhillon (1998) for this relationship. The effect of this M_2 constraint on M_1 is shown in Fig. 4.6. The corresponding estimates for all system parameters are listed in the fourth section of Table 4.1.

4.5 Spectral type and distance

Bailey (1981)'s method is based on the fact that the K-band surface brightness, $S_{\rm K}$, is only a weak function of spectral type among isolated, late-type, main-sequence stars. The definition of $S_{\rm K}$ is

$$S_{\rm K} = K + 5 - 5\log d + 5\log R_2 \tag{4.2}$$

where K is the star's K-band magnitude, R_2 is its radius (in solar units) and d is its distance (in parsecs). The most recent calibration of S_K against $(V-K)$ colour for late-type stars is due to Beuermann (2000)

$$S_K = 2.98 + 0.264(V - K_{cit}). \tag{4.3}$$

In this equation, V is the usual Johnson waveband, and K is on the CIT system as defined by Elias et al. (1982). Our own K-band observations are on the UKIRT system, but according to Leggett (1992), $K_{cit} = K_{ukirt}$. By combining Equations 4.2 and 4.3, the distance towards a CV can be determined.

In the case of DW UMa, we have an estimate of the mid-eclipse K-band magnitude obtained during a low-state, i.e., at a time when any white dwarf and disc contribution should be relatively small. This estimate – $K_{ukirt} = 16.43 \pm 0.14$ – should therefore be quite close to the true K-band magnitude of the secondary.

In order to determine, S_K, one needs the $(V-K)$ colour of the secondary. In practice, this is difficult to obtain in most CVs, including DW UMa, because the V-band is usually dominated by the white dwarf and/or the accretion disc of the system, and hence the $(V-K)$ colour must be estimated from its (known/assumed) spectral type. In our case, although we do not have a V magnitude for the secondary, we do have an estimate – $I_{kc} = 18.71 \pm 0.14$ – of the mid-eclipse I-band magnitude in the low state. We can therefore use the observed $(I-K)$ colour to estimate the spectral type of the secondary and use this to predict its $(V-K)$ colour.

More specifically, we use the spectral-type vs colour calibration presented by Bessell (1991). This calibration uses optical colours (*BVRI*) on the Kron-Cousins system, but infrared colours (*JHKL*) on Bessell & Brett (1988) homogenized system. We therefore used the transformations provided by Bessell & Brett (1988) to transform our $K_{ukirt} = K_{cit}$ to K_{BB} (on the Bessell & Brett 1988 system), although the resulting correction turned out to be insignificant (+0.02). Armed with the $(I_{kc} - K_{BB})$ colour of the secondary (Ta-

Table 4.2: Parameters inferred from I- and K-band photometry.

Parameter	Value
$(I_{\rm kc} - K_{\rm BB})$	2.3 ± 0.2
Spectral Type...	$M3.5 \pm 1.0$
d (pc).....	930 ± 160

ble 4.2), we then interpolated on Table 2 of Bessell (1991) to estimate the spectral type of the secondary in DW UMa, $M3.5 \pm 1.0$ (to the nearest half-subtype). This may be compared with the spectral type of $M4.2 \pm 0.8$ predicted by Smith & Dhillon (1998)'s orbital period-spectral type relation for CV secondaries (the error here corresponds to the rms scatter of the data about their relation). For this spectral type, Bessell (1991) predicts $(V-K) = 5.0 \pm 0.7$, which in turn gives $S_{\rm K} = 4.3 \pm 0.2$. Here, we have dropped the subscript on K, since the differences between the various systems are insignificant compared to the uncertainty on the colour.

Having determined both K and $S_{\rm K}$, we can now estimate the distance to DW UMa. We use the secondary's radius derived from the Smith & Dhillon (1998) mass-period relation for CV secondaries and Eggleton (1983)'s approximation for the radius, $R_2/R_\odot = 0.34 \pm 0.04$ (Sec. 4). Solving Equation 4.2 for d finally yields an estimate $d = 930 \pm 160$ pc (Table 4.2).

By comparison, Knigge et al. (2000) estimated $d = 830 \pm 150$ pc from the normalization of their fit to the low state FUV spectrum and the radius of the white dwarf inferred from their $\log g$. This agrees very well with our own estimate, but this is partly fortuitous since their fit yielded $\log g = 7.60$, whereas our new parameters suggest $\log g \simeq 8$. We have therefore refit the low state FUV spectrum with surface gravity fixed at $\log g = 8$. Visually, this new fit is almost indistinguishable from the fit shown in Knigge et al.

(2000), with a reduced Chi-squared of $\chi^2_\nu = 1.55$ (up from $\chi^2_\nu = 1.50$). The parameters describing this new fit are listed in Table 4.3. Combining this with our new estimate of $R_1/R_\odot = 0.012 \pm 0.001$, we obtain a new value for the distance of $d = 590 \pm 100$ pc. If we adopt this distance estimate and assume that the mid-eclipse K-band flux is entirely due to the secondary, we can also obtain a new estimate for the spectral type of the donor star. With $d = 590 \pm 100$ pc, $K_{\rm ukirt} = K_{\rm cit} = 16.43 \pm 0.14$ and $R_2/R_\odot = 0.34 \pm 0.04$, Equations 4.2 and 4.3 predict $(V-K) = 8.5 \pm 1.9$. For this colour, Bessell (1991) predicts $SpT_2 = M7 \pm 2.0$ (to the nearest half-subtype). If not all of the K-band light is due to the secondary, the spectral type must be even later.

Our two sets of distance and spectral type estimates are only marginally consistent with each other. We therefore briefly consider potential sources of systematic errors in both of the methods we used to obtain them. Most distance estimates based on Bailey's method are, strictly speaking, lower limits, since the observed K-band magnitude may contain residual disc and/or white dwarf contributions (Hoard et al. 2002). In our case, the situation is less clear. This is because our value for d depends on our spectral type estimate, which in turn is based on the observed $(I-K)$ colour. But contamination by sources other than the secondary will affect the measured I- and K-band magnitudes differently. Indeed, any reasonable contaminating spectrum will be bluer than that of the secondary, in which case the I-band would be more contaminated than the K-band. If so, then our measured $(I-K)$ colour would be too blue, our spectral type too early and our predicted $(V-K)$ colour also too blue. Thus this effect may cause the distance to be *over*-estimated. It is not clear if our estimate for d is affected by these biases, and, if so, which of them dominates.

By contrast, the key assumption in the white dwarf fit is that the observed spectrum is due entirely to a fully visible white dwarf. We first consider the possibility that the observed spectrum actually includes a contribution from another component. If the spectrum of this source is redder than that of the white dwarf, then the true white dwarf spectrum

Table 4.3: Parameters inferred from the white dwarf model atmosphere fit.

Parameter	Value[a]
$T_{\rm eff}$ (K)	$50\,000 \pm 1000$
$\log g$ ($\log$cm s^{-2})	8^b
$v \sin i$ (km s^{-1})	345 ± 86
Z ($Z_\odot$)	0.71 ± 0.14
$N = 4\pi(R_1/d)^2$ (10^{-24})	2.68 ± 0.10 (stat) $\pm$ 0.67(sys)[c]
$E_{\rm B-V}$ (mag)	0.004 ± 0.004
$\log N_{\rm H}$ (cm^{-2})	19.4 ± 0.06
M_1 ($M_\odot$)	$0.67 \leq M_1 \leq 0.92$
R_1 ($R_\odot$)	$0.010 \leq R_1 \leq 0.014$
d (pc)	590 ± 100
Spectral Type	$M7 \pm 2.0$[d]

[a] Uncertainties on the fit parameters correspond to 2σ confidence level for one interesting parameter

[b] Fixed value

[c] The systematic error accounts for the uncertainty in the absolute flux calibration of the spectrum and and in the normalization of the models (Brown et al. 1996; Knigge et al. 1997)

[d] This value was calculated assuming the mid-eclipse K-band flux is entirely due to the secondary and adopting $d = 590 \pm 100$ and $R_2/R_\odot = 0.34 \pm 0.04$

must be (a) bluer and (b) fainter than the observed spectrum. Effect (a) would tend to make our distance estimate too low, because a hotter white dwarf is intrinsically brighter and, for given radius and observed flux, must therefore be further away. Effect (b) would also lead us to underestimate the distance, since the latter scales with observed flux as $F_{\rm obs}^{-1/2}$. Similarly, if the contaminating spectrum is bluer than the white dwarf spectrum (which seems unlikely), then effect (a) above is reversed and would compete with effect

(b). Finally, if a significant portion of the white dwarf is obscured, the observed spectrum arises from a projected area that is smaller than πR_1^2. For a given observed flux (and hence a fixed fit normalization $N = 4\pi R_1^2/d^2$), this would imply that our distance estimate is too large.

In principle, we consider the distance estimate based on the white dwarf model fit more direct, and therefore more reliable, than the estimate derived from Bailey's method. However, the spectral type of the secondary we infer from the former estimate seems suspiciously too late by comparison to other CVs with similar orbital periods (Beuermann et al. 1998). On balance, we therefore expect that the true distance and spectral type will turn out to lie between the values suggested by the two methods.

4.6 Discussion

SW Sex stars display a range of peculiarities that do not seem to fit the standard steady accretion disc model for nova-like variables. There is currently no single agreed-upon explanation for the SW Sex phenomenon. Indeed, no real consensus has been reached about whether SW Sex stars deserve a nova-like variable-sub-class label in the first place. Rather, the SW Sex *syndrome* is so widespread (also seen in X-ray binaries; Hynes et al. 2001) that we must consider the possibility that some important element is missing in our standard picture of the accretion flows. Whatever the nature of the SW Sex stars, they may play an important role in CV evolution: with very few exceptions (e.g., BT Mon with $P_{\rm orb} = 8$ hrs; Smith et al. 1998), SW Sex stars have orbital periods falling in the 3 – 4 hrs range, just above the period gap.

Reliable system parameters are desperately needed in order to understand the origin of the SW Sex phenomenon. Unfortunately, the very characteristics that distinguish SW Sex stars from other nova-like variables have also prevented us from accurately determining

their physical and geometrical parameters. In particular, the phase-shifted radial velocity curves seen in these systems make it very difficult to accurately determine the K-velocities of the component stars (from which other system parameters could then follow). In addition, the high accretion rates exhibited by the SW Sex stars hamper the detection of the individual components of the system since the accretion disc dominates the emission and may even be self-occulting (Knigge et al. 2000). These latter effects are greatly reduced during the sporadic low states displayed by at least some of the SW Sex stars.

In the case of DW UMa, radial velocity studies have been carried out based on both high-state (Shafter et al. 1988) and low-state (Dhillon et al. 1994; also see Rutten & Dhillon 1994) observations. However, as emphasized by both sets of authors, neither study has provided reliable results. In the former study, significant ($55° - 75°$) phase lags were seen in all the radial velocity curves from which K_1 was estimated; in the latter study, the radial velocity curve was based on emission lines that clearly arise on the irradiated front face of the secondary (Rutten & Dhillon 1994), and may therefore provide only a lower limit for K_2.

Our HST low state *FUV* observations of DW UMa have provided a rare opportunity to accurately determine the system parameters of an SW Sex star from the eclipses of its white dwarf. This has been possible because the accretion disc contribution is dramatically reduced, revealing the sharp ingress and egress features that mark the white dwarf eclipse. Therefore, we have been able to avoid many of the difficulties associated with radial velocity studies. However, potential sources of systematic errors remain and include (1) our assumption that the white dwarf is entirely unobscured, (2) the application of the mass-period relation for CV secondaries, and (3) the application of the theoretical mass-radius relation for isolated white dwarfs.

As it turns out, the system parameters listed in Table 4.1 agree reasonably well with the constraints inferred by Shafter et al. (1988) and Dhillon et al. (1994) from radial velocity

analyses. However, as argued above, we consider our new estimates to be considerably more reliable, particularly the ones labelled "fundamental" in Table 4.1. Our estimate of the white dwarf mass ($M_1/M_\odot \simeq 0.77$) is considerably higher than that obtained by Knigge et al. (2000) from their model atmosphere fit to the low state HST *FUV* spectrum ($M_1/M_\odot \simeq 0.5$). Their estimate was based on the surface gravity inferred from the spectral fit and essentially the same mass-radius relation used here but for a white dwarf with $T_{\rm eff} = 46000$ K (Panei et al. 2000). Given the systematic uncertainties inherent in spectroscopic $\log g$ estimates, we consider our new set of constraints on the white dwarf parameters more reliable.

Both of our distance estimates, $d = 930 \pm 160$ pc (from Bailey's method) and $d = 590 \pm 100$ pc (from the white dwarf model fit), indicate that DW UMa is quite far away. For comparison, Marsh & Dhillon (1997) estimated $d \gtrsim 850$ [450] pc if the secondary is an $M4$ [$M5$] star, based on the absence of clear secondary signatures in their low-state I-band spectroscopy. We note, however, that even though our estimate of $I \simeq 18.7$ for the secondary star is fainter than the (out-of-eclipse) I-band magnitude they actually observed ($I \simeq 18$), it is brighter than the limit of $I > 19.5$ ($< 25\%$) they suggest for the secondary's contribution to their spectrum. If the mid-eclipse I-band flux in our data is due to the secondary, the latter should have contributed roughly half of the I-band flux in their spectrum instead of the $< 25\%$ they claimed. If, on the other hand, our I-band flux measurement is not entirely due to emission from the secondary but to a combination of secondary plus contribution from another source, then their estimate would be closer to the truth.

4.7 Summary

I have presented new constraints on the system parameters of the SW Sex star DW UMa, based on *FUV* eclipse observations with the HST. The data were obtained during a low state of the system, in which the *FUV* light was dominated by the hot white dwarf primary. The duration of the white dwarf eclipse allows us to set a firm lower limit on the mass ratio, $q = M_2/M_1 > 0.24$; if $q < 1.5$ (as expected on theoretical grounds) the inclination must satisfy $i > 71°$. We have also been able to determine the duration of white dwarf ingress and egress from our data. This allows us to constrain the masses and radii of the system components and the distance between them to be $0.67 \leq M_1/M_\odot \leq 1.06$, $0.008 \leq R_1/R_\odot \leq 0.014$, $M_2/M_\odot > 0.16$, $R_2/R_\odot > 0.28$ and $a/R_\odot > 1.05$. If the secondary follows Smith & Dhillon's mass-period relation for CV secondaries, our estimates for the system parameters become $M_1/M_\odot = 0.77 \pm 0.07$, $R_1/R_\odot = 0.012 \pm 0.001$, $M_2/M_\odot = 0.30 \pm 0.10$, $R_2/R_\odot = 0.34 \pm 0.04$, $q = 0.39 \pm 0.12$, $i = 82° \pm 4°$ and $a/R_\odot = 1.14 \pm 0.06$.

We have also obtained time-resolved I- and K-band photometry of DW UMa during the same low state. Using Bessell's spectral-type vs $(I-K)$ colour calibration, we estimate the spectral type of the donor star to be $M3.5 \pm 1.0$. This latter result helps us to estimate the distance towards the system via Bailey's method as $d = 930 \pm 160$ pc.

Finally, we have repeated Knigge et al. (2000)'s white dwarf model atmosphere fit to the low-state *FUV* spectrum of DW UMa in order to account for the higher surface gravity indicated by our eclipse analysis. The best-fit model with surface gravity fixed at $\log g = 8$ has an effective temperature of $T_{\rm eff} = 50\,000 \pm 1000$ K. The normalization of the fit also yields a second distance estimate, $d = 590 \pm 100$ pc. If we adopt this distance and assume that the mid-eclipse K-band flux is entirely due to the donor star, we obtain a second estimate for the spectral type of the secondary in DW UMa, $M7 \pm 2.0$. After discussing potential sources of systematic errors in both methods, we conclude that the true value for

the distance and spectral type will probably be in between the values obtained by the two methods.

I conclude this chapter by reiterating the need for accurate system parameters for the SW Sex stars. Given that most SW Sex stars are high-inclination systems, it is natural to try and exploit this in the way we have done here. However, eclipse analyses based on white dwarf ingress and egress features are usually impossible, since the light from these systems is usually dominated by their (possibly self-occulting) accretion discs. In the case of DW UMa, we have succeeded only because the system was caught in a deep low state. This raises the obvious question whether other SW Sex systems may also exhibit such low states. This would obviously be interesting for its own sake, but would also open a new avenue of attack for determining their system parameters.

A partial answer to this question is already available: of the 19 objects listed as SW Sex stars in the Göttingen Online CV Catalog[1], 5 (including DW UMa) are already classified as VY Scl stars (i.e. nova-like variables that exhibit occasional low states). We therefore advocate a long-term photometric monitoring program of SW Sex stars. This would tell us whether all SW Sex stars are also VY Scl stars and permit us to exploit the low states when they occur.

[1] http://www.cvcat.org

Chapter 5

1RXS J062518.2+733433: A New Intermediate Polar

5.1 Introduction

1RXS J062518.2+733433, henceforth RX J0625, has been observed as part of our ongoing search for new CVs selected on the basis of their spectroscopic properties from the HSQ. RX J0625 was originally identified as a CV on the basis of its X-ray emission and optical spectrum (Wei et al. 1999). We have independently selected RX J0625 as a CV candidate because of the noticeable Balmer emission in its HQS data (see Fig. 5.1). The strong He II λ4686 emission detected in the identification spectrum of RX J0625 (see Fig. 5.2) along with coherent optical variability observed on a time scale of $\sim$ 20 min in the photometry (see Fig. 5.3), immediately reveal the IP nature of this CV.

In this chapter I present a detailed study of this new IP CV. The structure goes as follows: observations and data reduction are described in Sect. 5.2; the orbital and spin

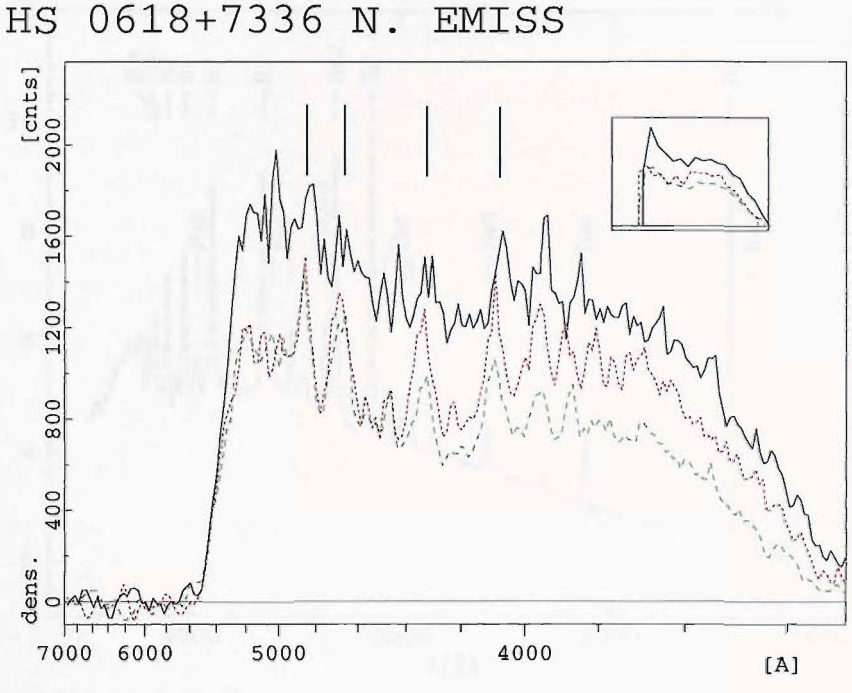

Figure 5.1: HQS density spectra of RX J0625. The three spectra displayed in the figure were obtained at three different epochs in order to search for variability. The lines mark the position of Hδ λ4102, Hγ λ4341, He II λ4686 and Hβ λ4861 from right to left. Note the inverted logarithmic scale of the x-axis. The small insert show the low resolution version of the spectra (15 pixel per spectrum).

period are computed, from radial velocity analysis and differential photometry respectively, in Sect. 5.3; finally, the behaviour of the strongest emission lines is discussed in Sect. 5.4 and a summary of the whole analysis is given Sect. 5.5.

5.2 Observations and Data Reduction

5.2.1 Spectroscopy

On April 29 2001 we obtained a single identification spectrum of RX J0625 at the Calar Alto 2.2 m telescope with the CAFOS focal reductor spectrograph, using the standard

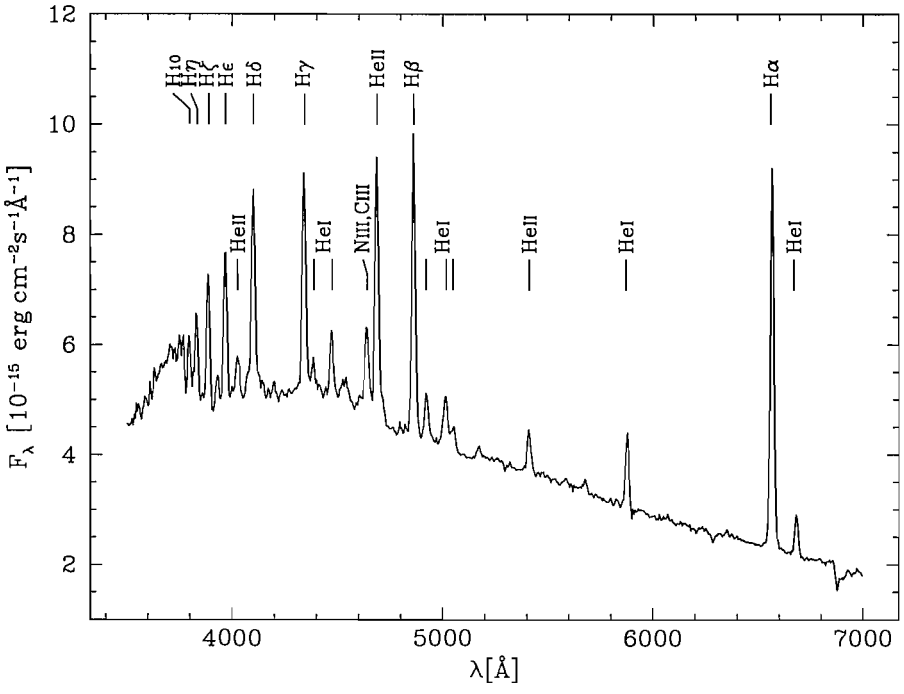

Figure 5.2: Identification spectrum of RX J0625 obtained on 2001 April 29.

SITe CCD (Table 1). We used the B-200 grism and a slit width of 2″, resulting in a useful wavelength range of 3500–7000 Å and a spectral resolution of 4.7 Å (Fig. 5.2). A flux standard (BD+75° 325) was observed with the same set-up in order to correct for the instrumental response. The identification spectrum contains noticeable Balmer, He I and He II and N/C Bowen emission lines. The strength of He II λ4686 is comparable to Hβ, indicating the presence of a strong source of ionizing photons in RX J0625, typical of either magnetic CVs or nova-like variables.

In order to determine the orbital period of RX J0625, we obtained 45 higher resolution spectra, again with CAFOS at the Calar Alto 2.2 m telescope (Table 5.1). This time the G-100 grism was used in conjunction with a 1.2″ slit which gave a wavelength range of 4240–8300 Å and a spectral resolution of 4.2 Å. The higher resolution spectra were obtained over a period of 3 weeks, optimizing the sampling for an efficient period determination.

Table 5.1: Log of Observations.

Date	UT Time	Data	Exp.(s)	Num. Obs	Observer[a]
		Spectroscopy			
2001 Apr 29	20:37 - 20:47	B-200	600	1	BG
2002 Dec 09	01:09 - 01:21	G-100	600	2	BG
2002 Dec 13	04:05 - 05:44	G-100	600	9	service
2002 Dec 14	23:20 - 00:08	G-100	600	5	service
2002 Dec 15	03:00 - 03:45	G-100	600	5	service
2002 Dec 15	05:23 - 06:07	G-100	600	5	service
2002 Dec 15	22:47 - 23:32	G-100	600	5	service
2002 Dec 16	01:39 - 02:24	G-100	600	5	service
2002 Dec 28	23:04 - 23:26	G-100	600	3	SAB
2002 Dec 29	01:12 - 01:34	G-100	600	3	SAB
2002 Dec 29	03:58 - 04:20	G-100	600	3	SAB
		Photometry			
2002 Dec 09	01:29 - 06:23	V	30	386	BG
2002 Dec 15	00:57 - 02:14	Clear	30	100	service
2002 Dec 15	02:33 - 02:39	Clear	30	10	service
2002 Dec 16	00:00 - 01:15	Clear	30	100	service
2002 Dec 28	21:07 - 22:23	V	30	100	SAB
2002 Dec 28	23:43 - 00:51	V	30	98	SAB
2002 Dec 29	01:48 - 03:41	V	30	270	SAB
2002 Dec 29	23:55 - 03:36	V	30	23	SAB
2002 Dec 30	03:55 - 04:48	V	30	293	SAB
2002 Dec 31	04:11 - 06:00	V	30	136	SAB

[a] BG: Boris Gänsicke, SAB: Sofía Araujo-Betancor

Table 5.2: Equivalent widths and line widths (corrected for the instrumental resolution) of the strongest emission lines measured from the average of the 45 spectra obtained in December 2002

Line	FWHM [Å]	EW [Å]
Hγ	13.7 ± 0.2	14.3 ± 1.0
He II λ4686	14.2 ± 0.3	15.0 ± 2.0
Hβ	14.2 ± 0.2	22.0 ± 2.0
He I λ5876	14.0 ± 0.3	9.6 ± 0.5
Hα	15.8 ± 0.2	64.0 ± 2.0
He I λ6678	17.3 ± 0.2	7.5 ± 0.5

All spectra were reduced in a standard manner using the `Figaro` package within the Starlink software collection. The frames were corrected for the bias level by subtracting the mean of a series of bias images taken at the start and end of each observing night. Dome flat-fields were used to remove pixel to pixel variations of the chip. The spectra were then optimally extracted (Horne 1986; Marsh 1989) and sky line subtracted using Tom Marsh's `Pamela` package. Special care was taken to account for the tilt of the spectra in order to maximize the signal-to-noise ratio. The wavelength calibration was performed using mercury-cadmium, helium-argon and rubidium arcs. Uncertainties on every data point calculated from photon statistics and readout noise are rigorously propagated through every stage of the data reduction. We did not attempt to flux-calibrate the higher resolution spectra as it was not required for the radial velocity analysis described below.

Table 5.2 gives the equivalent widths and line widths of the main emission lines detected in the average of the 45 high resolution spectra.

5.2.2 Photometry

We obtained differential V-band and filterless photometry of RX J0625 during 6 nights in December 2002 with the CAFOS SITe CCD camera on the Calar Alto 2.2 m telescope (Table 5.1). In order to achieve a high time resolution (~ 30 s), only a small window of the chip ($\sim 3' \times 2'$) was read out. The data were bias-subtracted and flat-fielded in a standard fashion using the ESO-MIDAS package, and aperture magnitudes were extracted with the sextractor (Bertin & Arnouts 1996). The V magnitudes of RX J0625 were derived relative to the HST Guide Star GSC 0437000234 ($V = 13.4 \pm 0.4$), located $1'50''$ southwards of RX J0625. This comparison star was saturated in a number of the filterless CCD images obtained on December 14/15, and, hence, we used GSC 0437000998 ($V = 14.9 \pm 0.4$), located $1'10''$ northwards of RX J0625 for the reduction of these images. RX J0625 was found at an average magnitude of 14.80 ± 0.05(statistical) ± 0.4(systematic) throughout the nights in which we used the V band filter. The light curves of RX J0625 clearly reveal the presence of variability with a period of ~ 20 min and an amplitude of $\sim \pm 0.2$ mag throughout all nights (Fig. 5.3). In addition to this short-term variation the light curve of RX J0625 displays a modulation on time scales of several hours.

5.3 Analysis

5.3.1 Spectroscopy

The primary aim of our time-resolved spectroscopy of RX J0625 is to measure its orbital period from the radial velocity variations of the emission lines. The line profiles clearly display a complicated multicomponent structure (Fig. 5.4). In a first attempt, we used a single Gaussian least square fitting procedure to determine the radial velocity variations of Hα, Hβ and He II λ4686. The radial velocity data were then subjected to the follow-

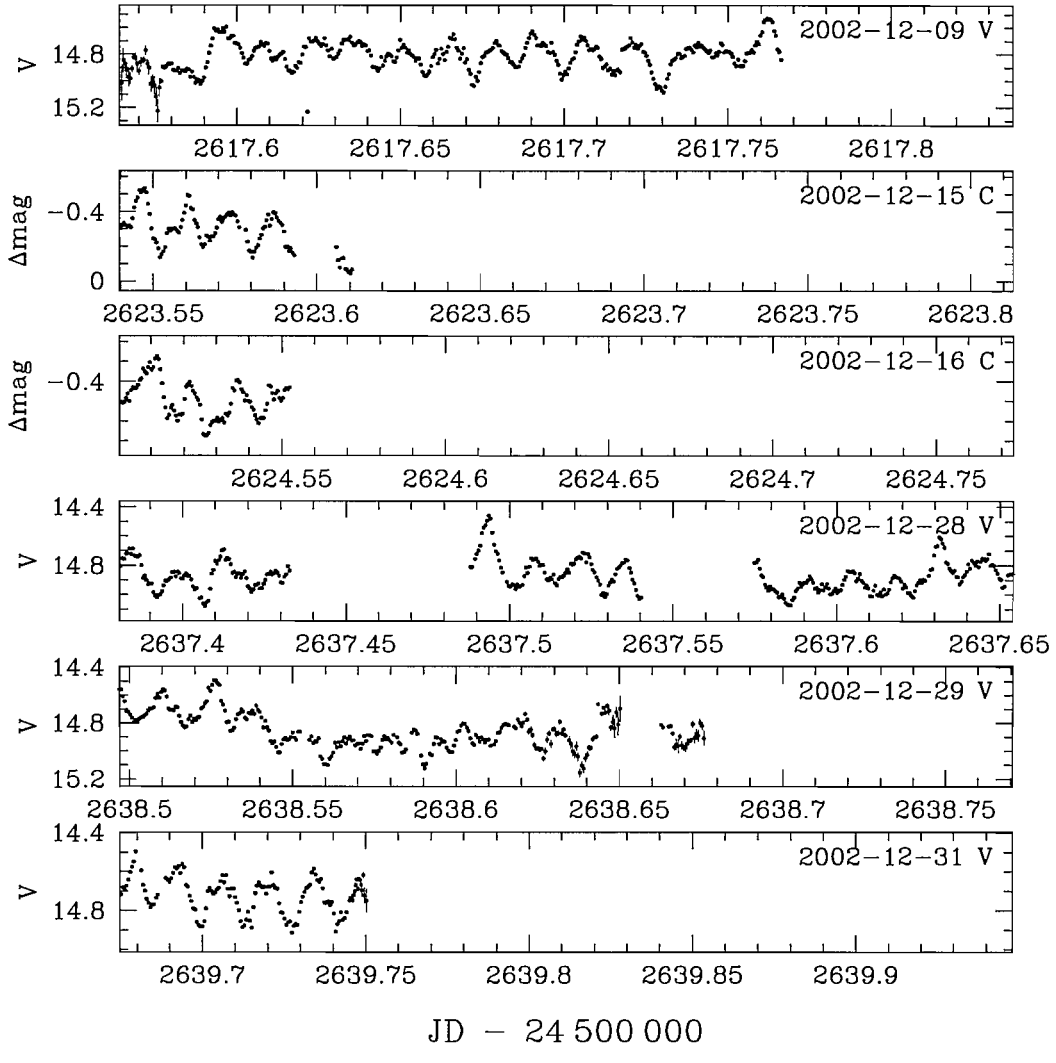

Figure 5.3: Differential CCD V-band (V) and filterless (C) photometry obtained at the Calar Alto 2.2 m observatory. Note the different scales of the filterless and V band data.

ing period analysis methods: (a) the phase dispersion method (Stellingwerf 1978), (b) the analysis of variance (Schwarzenberg-Czerny (1989), as implemented in the `MIDAS` context `TSA`), (c) and a sine wave χ^2 fitting procedure, using `chisq` in the Starlink package `period`. The resulting periodograms for Hα are shown in Fig. 5.5. The orbital frequency (period) is inferred from the three independent techniques in a consistent way to be $\Omega = 5.088 \pm 0.003\,\mathrm{d}^{-1}$($P_{\mathrm{orb}} = 283.0 \pm 0.2$ min), where the error is computed from the

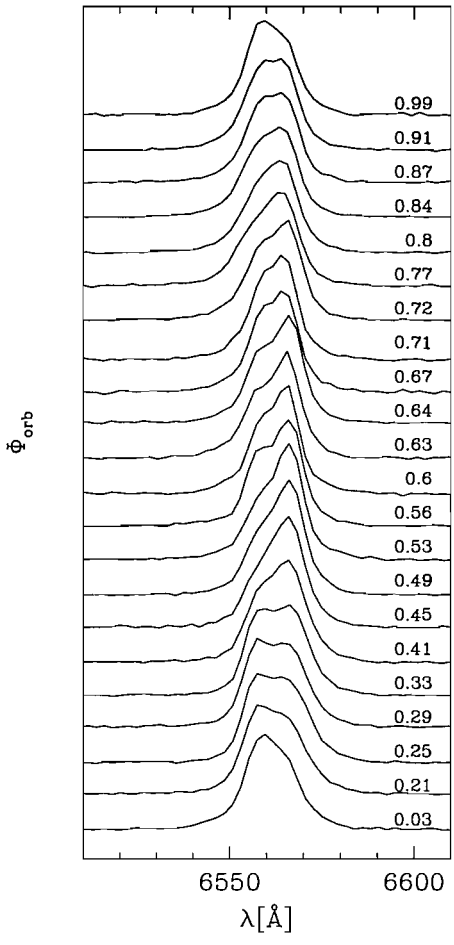

Figure 5.4: Continuum-subtracted and normalized Hα profile sample sorted by orbital phases computed from Eq. 5.2.

χ^2 sine wave fitting (2σ, 4 free parameter). A slightly more conservative error estimate based on the results obtained from all three methods gives $P_{\rm orb} = 283.0 \pm 0.3$ min. The analysis of Hβ and He II λ4686 provides consistent results for $P_{\rm orb}$, but with significantly larger errors. The robustness of our period determination is shown in Fig. 5.6 where we folded the Hα radial velocities over the orbital period. The radial velocity measurements from this fit are provided in Table 5.3.

For comparison purposes we measured the radial velocities of Hα cross-correlating the observed line profile with a single Gaussian of fixed width of $300\,{\rm km\,s^{-1}}$ (Schneider & Young 1980). The resulting orbital period is identical to that derived from the single

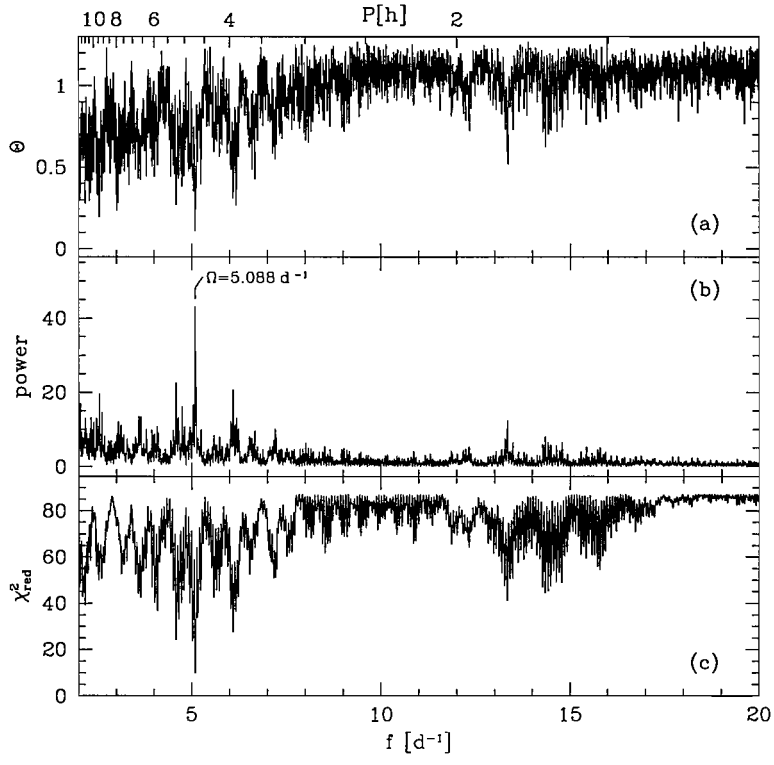

Figure 5.5: Period analysis of the radial velocities measured from a single Gaussian fit to the Hα emission line profiles. (a): Phase dispersion method periodogram. (b): Analysis of variance periodogram. (c): χ^2 sine fit.

Gaussian fit to the Hα profiles, but the radial velocity variation displays an amplitude larger by a factor of ~ 2.

Finally, we attempted to fit the Hα emission with a blend of a narrow and a broad Gaussian component to model more accurately the complex structure of the observed profiles. Unfortunately, this procedure did not provide unambiguous results because of the limited spectral resolution of our data. Due to the multicomponent structure of the lines profile (see Fig. 5.4) it is difficult to interpret the radial velocity variation obtained from either the single Gaussian fit (Fig. 5.6) or the Gauss correlation to Hα. The behaviour of the most important emission lines is discussed in more detail in Sect. 5.4 on the basis of trailed spectrograms.

Table 5.3: Radial velocities of the Hα emission line determined from a single-Gaussian fit to the line profile (corrected for the heliocentric velocity).

HJD −2450000	RV [km s^{-1}]	RV error [km s^{-1}]	HJD −2450000	RV [km s^{-1}]	RV error [km s^{-1}]	HJD −2450000	RV [km s^{-1}]	RV error [km s^{-1}]
617.5515	42.7	9.3	623.5093	-31.0	6.0	624.4842	1.6	6.0
617.5598	61.9	8.5	623.6290	24.3	4.8	624.5729	-54.7	5.5
621.6740	48.7	5.3	623.6368	42.1	4.2	624.5807	-51.5	5.4
621.6847	35.4	5.9	623.6446	64.0	5.0	624.5884	-16.3	6.4
621.6925	27.2	6.0	623.6524	65.4	6.0	624.5962	-21.8	6.3
621.7003	24.9	6.5	623.6601	64.9	7.1	624.6040	11.6	6.3
621.7085	14.4	6.2	623.7279	-48.5	4.2	637.4651	-51.3	5.7
621.7162	5.2	5.1	623.7357	-61.2	3.8	637.4729	-82.4	5.7
621.7240	-9.8	4.8	623.7434	-88.2	3.9	637.4807	-85.1	4.5
621.7318	-12.1	4.6	623.7512	-84.6	3.8	637.5538	-69.1	4.1
621.7425	-20.8	5.4	623.7590	-88.2	4.0	637.5616	-33.9	4.7
623.4760	8.3	7.6	624.4531	26.7	7.2	637.5694	-28.9	4.5
623.4838	6.9	7.4	624.4609	26.7	7.0	637.6690	-45.4	4.5
623.4915	6.0	5.6	624.4687	31.7	7.0	637.6768	-61.9	4.7
623.5007	-10.9	6.1	624.4764	18.9	6.2	637.6846	-66.9	3.9

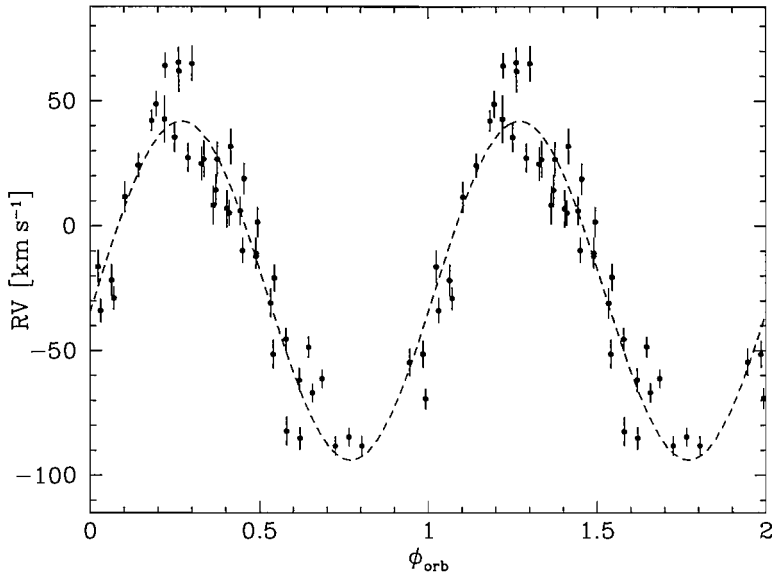

Figure 5.6: Radial velocities measured from a single Gaussian fit to the Hα emission line profiles, folded with the orbital period $P_{orb} = 283.0\,\mathrm{min}$, using Eq. (5.2). The dashed curve is the best sine fit to the radial velocities.

5.3.2 Photometry

In order to analyze the periodicities observed in the light curve of RX J0625 (Fig. 5.3), we have computed from the entire photometric data set both a Scargle (1982) periodogram (as implemented in the `MIDAS` context `TSA`) as well as a periodogram using the Phase Dispersion Method (PDM) of Stellingwerf (1978). Because the lengths of our individual photometric observations are of the order of or shorter than the orbital period, subtracting the nightly mean from the data would introduce erroneous signals in the low-frequency range of the periodograms. Considering that RX J0625 does not exhibit noticeable night-to-night variability, we decided to subtract from the V filter and white light data the mean of all measurements obtained in the corresponding band prior to the computation of the periodograms. The resulting periodograms (Fig. 5.7 and 5.8) contain strong signals concentrated in the frequency ranges $f \lesssim 10\,\mathrm{d}^{-1}$ and $f \simeq 60 - 70\,\mathrm{d}^{-1}$. The nature of the signals detected in these two separate frequency regimes is discussed below.

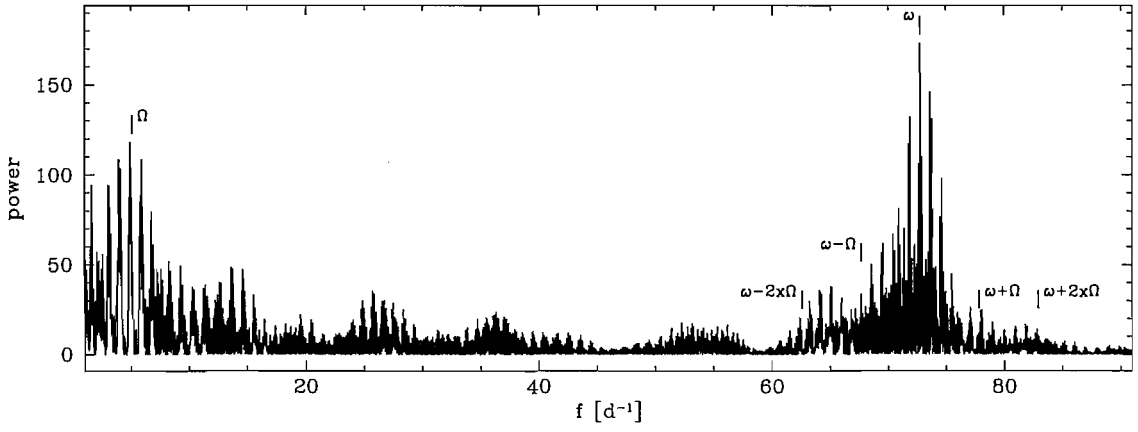

Figure 5.7: Scargle periodogram of the differential CCD photometry shown in Fig. 5.3. ω and Ω are the white dwarf spin and orbital frequency, respectively.

High-frequency signal. Figure 5.8 shows an enlargement around the peak signal contained in the high-frequency range of the periodogram shown in Fig. 5.7. Both period analysis methods consistently detect the maximum power at $72.772 \pm 0.008\,\mathrm{d}^{-1}$, corresponding to a period of 19.788 ± 0.002 min, whose error is given by 1σ width of the Gaussian fit to the frequency peak. In order to test the significance of this signal, we have created a faked data set from a sine wave with a period of 19.788 min, a similar amplitude to the observed short-period variability, and sampled exactly in the same way as the observed data. In addition, we added a 10% error to these synthetic data. The periodograms for this faked data set are plotted in gray in Fig. 5.8, and reproduce very well the entire structure of aliases contained in the periodograms of the observed data. We repeated the same analysis to test the significance of the most prominent alias frequencies (see the black line in Fig. 5.8) resulting in Scargle periodograms that differ significantly from that of the real data. We conclude from this comparison that the frequency of the maximum signal detected in the periodograms is indeed the true period underlying the short-term variability observed in RX J0625.

Coherent variability on time scales of a several minutes to several tens of minutes has been detected in the optical light curves of a number of IPs (e.g. Patterson 1994), and is interpreted as the spin period of the accreting magnetic white dwarf. We conclude from

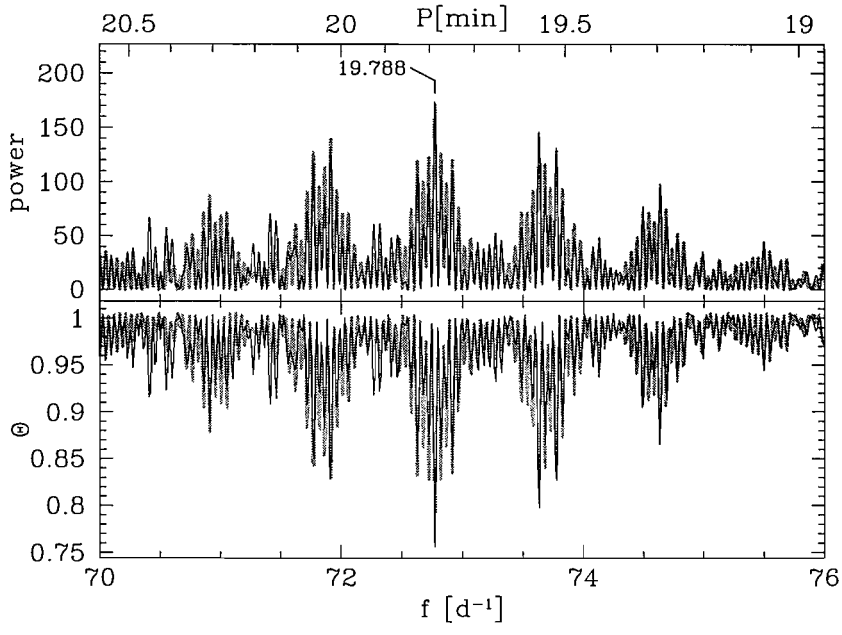

Figure 5.8: Period analysis near the presumed white dwarf spin. Top panel: Scargle periodogram. Bottom panel: phase dispersion periodogram. The black lines are computed from the observed data. The gray lines are computed from a sinusoid assuming a period of $1/\omega = 19.788$ min and identical sampling as in the observed data.

the spectral appearance of RX J0625 and from the detected coherent optical variability that RX J0625 is indeed a new member of the small class of IPs. We suggest that the detected frequency (period) of $72.772\,\mathrm{d}^{-1}$ (19.788 min) is the white dwarf spin frequency ω (period $P_{\mathrm{spin}} = 1/\omega$). From the combined V band and filterless photometry, we derive the following spin ephemeris:

$$\phi_0^{\mathrm{spin}} = \mathrm{HJD}\,2452617.0645(4) + 0.013742(3) \times E \tag{5.1}$$

where $\phi^{\mathrm{spin}} = 0$ is defined as the spin pulse maximum. Errors in the last digit are given in brackets. Figure 5.9(a) shows our photometric data folded with this ephemeris. The quasi-sinusoidal shape of this light curve, which is typical for the spin light curve of IPs (see, e.g., the spin light curve of FO Aqr by de Martino et al. 1994), lends support to our hypothesis that the $72.772\,\mathrm{d}^{-1}$ frequency detected in the power spectrum of RX J0625 is indeed the spin frequency of the white dwarf.

Another hallmark of IPs is the detection of beat frequencies between the white dwarf spin frequency ω and the orbital frequency Ω. These beat frequencies arise from the reprocessing of X-rays which are emitted close to white dwarf, on other structures fixed in the binary frame, e.g. the secondary star. Such sideband signals have been detected in different systems at $\omega - 2\Omega$, $\omega - \Omega$, $\omega + \Omega$, $\omega + 2\Omega$ (see Warner 1986 for an interpretation of these frequencies). In RX J0625, the only unambiguous detection of a sideband signal is $\omega - \Omega$ (see Fig. 5.7). The photometric data folded over this beat period of 21.275 min are shown in Fig. 5.9(b). While we are confident that our identifications of the spin and beat period are correct, we mention as a note of caution that time-resolved X-ray and/or polarimetric data are necessary to unambiguously confirm this interpretation.

Low-frequency signal. The strongest signal in the low-frequency range does not coincide with the orbital frequency derived in Sect. 5.3.1 from the radial velocity variation of Hα, but is found at 4.944 d^{-1}, corresponding to a period of 291.3 min. This period is $\simeq 3\%$ longer than the orbital period. Considering the sampling of our photometric time series, especially the fact that none of our data sets covers significantly more than one binary orbit, the most likely hypothesis is that the detected low-frequency signal is related to the orbital motion of the binary. Further observations would be useful to test in detail whether the low-frequency photometric frequency is indeed identical to the orbital frequency Ω.

5.4 Discussion

As already mentioned in Sect. 5.3.1, the line profiles clearly display a multicomponent structure (Fig. 5.4), which makes the interpretation of the determined radial velocity variations rather ambiguous (Fig. 5.6). To explore the behaviour of the emission lines in more detail, we constructed trailed spectra of Hα, Hβ, He I λ6678, and He II λ4686, which are

shown in Figure 5.10. These diagrams were computed from the continuum-normalized spectra after binning into 15 phase intervals. The He I λ6678 line clearly shows two emission components: a narrow one with a radial velocity semi-amplitude of $\approx 140\,\mathrm{km\,s^{-1}}$ and a wider one with velocity reaching $\sim \pm 500\,\mathrm{km\,s^{-1}}$. Both components are not in phase, the phase offset being ~ 0.15. The trailed spectra shown in Fig. 5.10 were phased according to the following orbital ephemeris

$$\phi_0^{\mathrm{orb}} = \mathrm{HJD}\,2452617.508(5) + 0.1965(1) \times E \tag{5.2}$$

where the instant of zero phase was derived as the time of blue-to-red crossing of the narrow component of He I λ6678.

By analogy with the narrow emission lines observed in many magnetic CVs, this narrow emission line component may have its origin on the irradiated face of the secondary star. In order to test this hypothesis, we performed the following simple calculation. The secondary mass was estimated from the mass-period relation derived by Smith & Dhillon (1998), which gives a value of $M_2 \approx 0.48\,M_\odot$. For the primary mass we adopted $M_1 = 0.8\,M_\odot$ (the average white dwarf mass in long-period CVs determined by Smith & Dhillon 1998), resulting in a mass ratio $q = M_2/M_1 \approx 0.6$. Assuming a disc radius of $0.8\,R_{\mathrm{L}_1}$, where R_{L_1} is the distance from the white dwarf to L_1, then the lack of eclipses in the optical light curve of RX J0625 sets an upper limit on the orbital inclination of $i \lesssim 60^\circ$. The projected velocity of the secondary is given by:

$$K_2 = \frac{2\pi a \sin i}{P_{\mathrm{orb}}(1+q)}\,, \tag{5.3}$$

where a is the binary separation. With the above assumptions, the radial velocity variation of the secondary star can be as large as $K_2 \approx 130\,\mathrm{km\,s^{-1}}$, which is comparable to the value obtained from the trailed spectrogram of the narrow He I λ6678 line. The predicted K_1 velocity is then $\approx 80\,\mathrm{km\,s^{-1}}$, somewhat larger than the semi-amplitude of the radial velocity curve of the broad component of Hα (Fig. 5.10, see also Fig. 5.6), but not inconsistent.

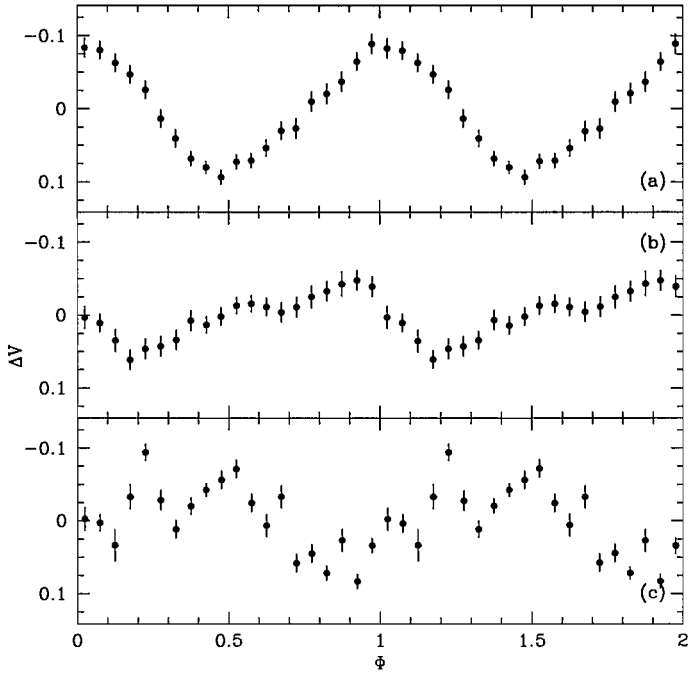

Figure 5.9: The photometric data points from Fig. 5.3 mean-subtracted and folded over: (a) The spin period of 19.788 min, using Eq. (5.1). (b) The beat period of 21.275 min. (c) The orbital period of 283.0 min, using Eq. (5.2).

Taken at face value, the behaviour of the narrow emission line components detected in our (admittedly rather low resolution) phase-resolved spectroscopy are consistent with an origin on the irradiated face of the secondary.

As I mentioned above, the broad component of the He I λ6678 line displays a phase offset of ~ 0.15 with respect to the narrow one, reaching a velocity of $\sim -500\,\mathrm{km\,s^{-1}}$ at its maximum excursion to the blue. The phasing with respect to the narrow component (and assuming that our above interpretation of the origin of the narrow component is correct) indicates that the broad emission is not coming from an axisymmetric structure around the white dwarf. Nevertheless, the high velocity dispersion observed in the broad component clearly points towards an origin close to the white dwarf. The maximum velocity to the blue is reached at phase $\sim 0.4 - 0.5$. A similar high-velocity S-wave has been observed in the IPs EX Hya (Hellier et al. 1989) and V1025 Cen (Hellier et al.

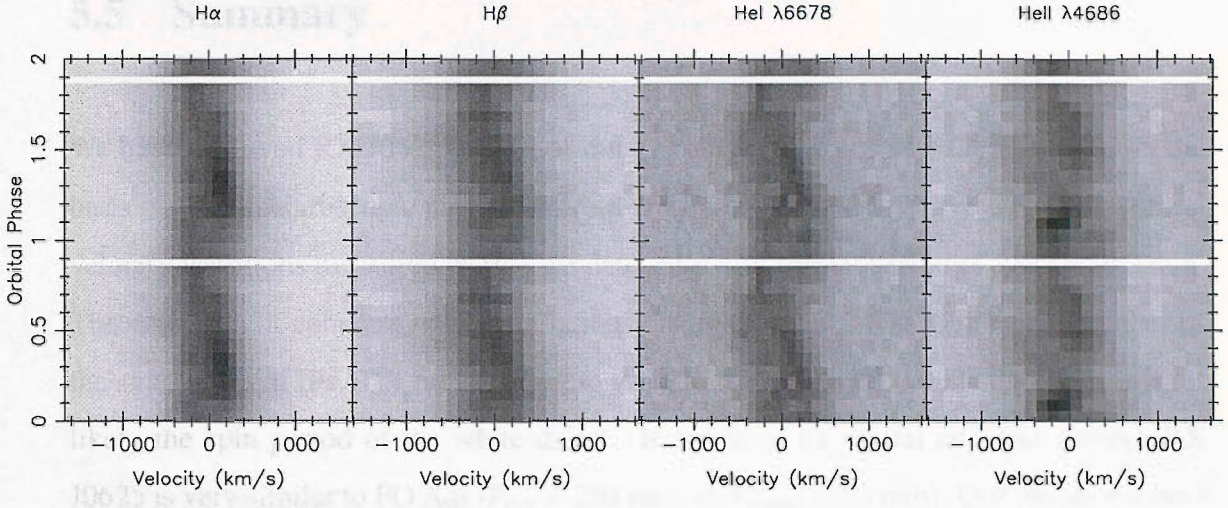

Figure 5.10: Trailed spectrograms of Hα, Hβ, He I λ6678 and He II λ4686, computed from the 45 spectra obtained in December 2002 (Table 5.1). Orbital phases have been computed using Eq. (5.2).

2002). The same components are also characteristic of the SW Sextantis stars, which have been recently proposed to be magnetic systems (Rodríguez-Gil et al. 2001). In all these systems, it is believed that these high-velocity S-waves form in the vicinity of the primary's magnetosphere.

The trailed spectra of He II λ4686 seem to exhibit the same two emission components, with the narrow one also dominating and the same velocity amplitudes as in He I λ6678. Also the trailed spectra of Hα and Hβ clearly show a multicomponent structure, even though their narrow components are less obvious than in He I λ6678. In order to securely identify the different line components with physical emission sites in the binary, it will be necessary to obtain time-resolved spectroscopy spanning several consecutive binary orbits with better spectral resolution.

5.5 Summary

We have observed RX J0625 as part of our ongoing search for new CVs selected on the basis of their spectroscopic properties from the Hamburg Quasar Survey. From the radial velocity variations measured in Hα, we determined an orbital period of 283.0 ± 0.2 min. The detection of coherent optical variations clearly classifies RX J0625 as a member of the small class of IPs. The period of these variations is 19.788 ± 0.002 min which is most likely the spin period of the white dwarf. In terms of its orbital and spin period, RX J0625 is very similar to FO Aqr ($P_{\rm orb} = 291$ min, and $P_{\rm spin} = 21$ min). Our phase-resolved spectroscopy clearly shows that the emission lines are multicomponent, and we identify a narrow component with a radial velocity semi-amplitude of $\simeq 140$ kms, which might originate from the irradiated face of the secondary.

Chapter 6

The Mysterious Nature of HS 2331+3905

6.1 Introduction

HS 2331+3905 (HS 2331 thereafter) was selected as a CV candidate on the basis of its spectral characteristics in the HQS (refer to Sec. 2.4.1 for details of the selection scheme). The insert of Fig 6.1 shows the low resolution HQS spectrum from which HS 2331 was initially selected as a blue object. Note here that the relatively flat appearance of the spectra in Fig. 6.1 is due to the increase in sensitivity of the HQS spectroscopic plates to the red part of the spectral range compared to the blue. The higher resolution HQS scans in the main frame of the same figure were taken at different epochs in order to provide information on the variability of the object. Even though HS 2331 did not show changes in brightness in the HQS observations (a typical behaviour found in many of the CVs contained in the HQS), its spectrum display the strong Balmer emission lines that

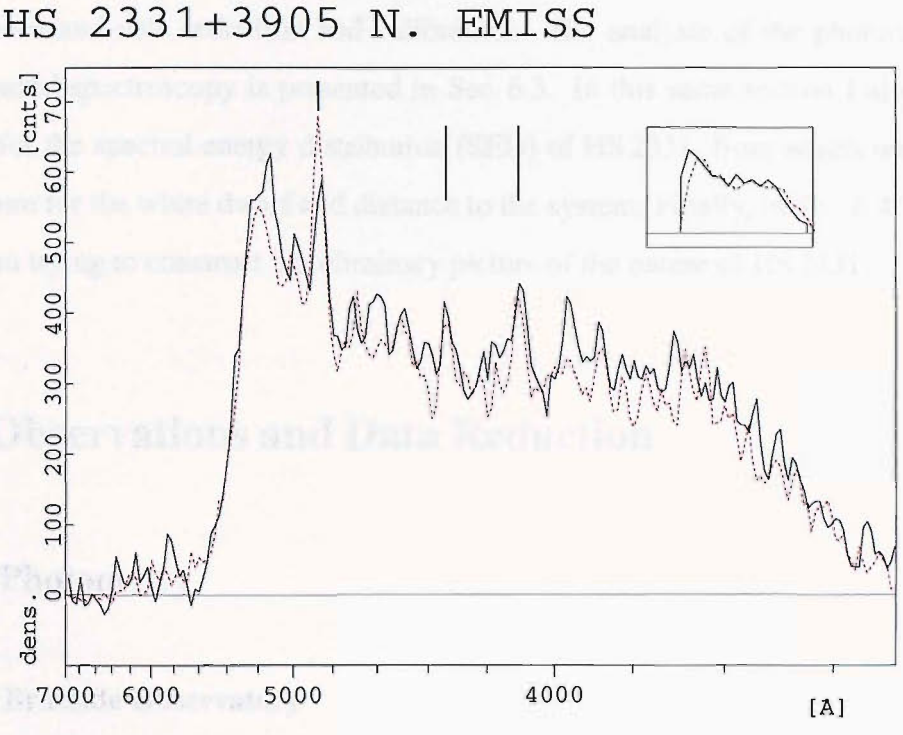

Figure 6.1: HQS density spectra of HS 2331. The two spectra displayed in the figure were obtained at two different epochs in order to probe for variability. The lines mark the position of Hδ λ4102, Hγ λ4341 and Hβ λ4861 from right to left. The small insert shows the low resolution scans of the spectra (15 pixel per spectrum). Note the inverted logarithmic scale of the x-axis.

strongly suggest ongoing accretion in CVs.

HS 2331 was confirmed to be a CV from subsequent spectral observations, which also unveiled a very unusual picture. The large amplitude 3.5 h radial velocity variation obtained from our optical spectroscopy is not the orbital period of the system, as one would normally expect. Instead, extensive CCD photometry strongly suggests that HS 2331 is a short orbital period CV ($P_{\rm orb} = 81.08$ min), containing a cold white dwarf which appears to exhibit ZZ Ceti pulsations.

In this chapter I present the results of the follow-up data of HS 2331 obtained over three years. In Sec. 6.2 I describe the photometric and spectroscopic (ground and space)

observations and data reduction and calibration. The analysis of the photometry and ground-based spectroscopy is presented in Sec. 6.3. In this same section I also present a model for the spectral energy distribution (SED) of HS 2331, from which we derive a temperature for the white dwarf and distance to the system. Finally, in Sec. 6.4, I use our findings in trying to construct a preliminary picture of the nature of HS 2331.

6.2 Observations and Data Reduction

6.2.1 Photometry

6.2.1.1 Braeside Observatory

Differential *R*-band CCD photometry of HS 2331 was obtained at the Braeside Observatory, immediately following the identification of its CV nature (see Sec. 6.2.2.1), in September-October 2000, using a 0.4 m reflector equipped with a SITe 512 CCD camera. HS 2331 was again observed from Braeside in November 2001 and October 2003, on both occasions in white light (Table 6.1).

The Braeside CCD light curves of HS 2331 display periodic variability with an amplitude of $\sim \pm 0.1$ mag which has consistently been detected in all three years covered by our observations. The morphology of the photometric modulation is best described by a double-humped pattern with a period of ~ 80 min. The relative strength of the two humps varies substantially between the individual nights. The 2003 data, a sample of which is shown in the upper panel of Fig. 6.2, reveal narrow dips centred on some of the observed minima between the humps.

6.2.1.2 Kryoneri Observatory

Filterless CCD photometry of HS 2331 was obtained during two nights in October 2002 and during 7 nights in August 2003 at the 1.2 m Kryoneri telescope using a SI-502 516 × 516 CCD camera (Table 6.1).

The October 2002 light curves, obtained with a time resolution of 25 s–30 s were essentially similar to the Braeside observations, displaying a double-humped structure with a period of $\sim$ 80 min. The middle panel of Fig. 6.2 displays a portion of the 10 s Kryoneri light curve. This higher time resolution data, obtained in August 2003, provide stronger evidence for the periodic dips detected in the Braeside observations, and clearly reveal additional short-term variability on a time scale of $\sim$ 5 min.

6.2.1.3 ULTRACAM on the William Herschel Telescope

The highest time resolution and signal-to-noise ratio CCD photometry was obtained on November 10 2003, using the 3-beam ULTRACAM CCD camera (which takes CCD data in three colour channels simultaneously, Dhillon et al. 2002) on the 4 m William Herschel Telescope (WHT) at the Roche de los Muchachos observatory in La Palma. HS 2331 was observed with a 1 s time resolution, using Sloan u, g, and r filters. The ULTRACAM light curves clearly confirm the presence of variability on a time scale of $\sim$ 5 min seen in the Kryoneri data, and, in addition, variability on even shorter time scales. Shown in Fig. 6.2 is the g-band ULTRACAM light curve.

All CCD data were bias-subtracted, dark-current-subtracted and flat-fielded in a standard fashion and instrumental aperture magnitudes for HS 2331 were derived relative to a comparison star.

Table 6.1: Log of Photometric Observations.

Date	UT Time	Data	Exp.(s)	#Frames	Observer[a]
40 cm Braeside Observatory					
2000 Sep 25	04:35 - 12:29	*R*	50	510	RF
2000 Sep 28	05:26 - 10:54	*R*	85	211	RF
2000 Oct 03	02:21 - 12:01	*R*	95	338	RF
2001 Nov 21	04:13 - 08:44	*C*	85	152	RF
2001 Nov 22	02:43 - 08:45	*C*	55	302	RF
2003 Oct 12	02:19 - 11:44	*C*	55	552	RF
2003 Oct 13	02:36 - 11:30	*C*	55	542	RF
2003 Oct 15	03:56 - 11:23	*C*	55	446	RF
1.2 m Kryoneri Observatory					
2002 Oct 15	18:41 - 22:39	*C*	30	340	SAB
2002 Oct 16	17:29 - 22:13	*C*	25	429	SAB
2003 Aug 14	22:56 - 02:52	*C*	10	1029	BG
2003 Aug 15	23:14 - 02:57	*C*	10	1012	BG
2003 Aug 16	23:33 - 03:06	*C*	10	980	BG
2003 Aug 17	23:32 - 03:04	*C*	10	948	BG
2003 Aug 18	22:23 - 03:01	*C*	10	1249	BG
2003 Aug 19	22:09 - 03:04	*C*	10	1311	BG
2003 Aug 20	21:56 - 03:07	*C*	10	1432	BG
4 m WHT/ULTRACAM					
2003 Nov 10	19:23 - 22:00	*u*	1	10013	TR
2003 Nov 10	19:23 - 22:00	*g*	1	10013	TR
2003 Nov 10	19:23 - 22:00	*r*	1	10013	TR

[a] RF: Robert Fried, SAB: Sofía Araujo-Betancor, BG: Boris Gänsicke, TM: Tom Marsh

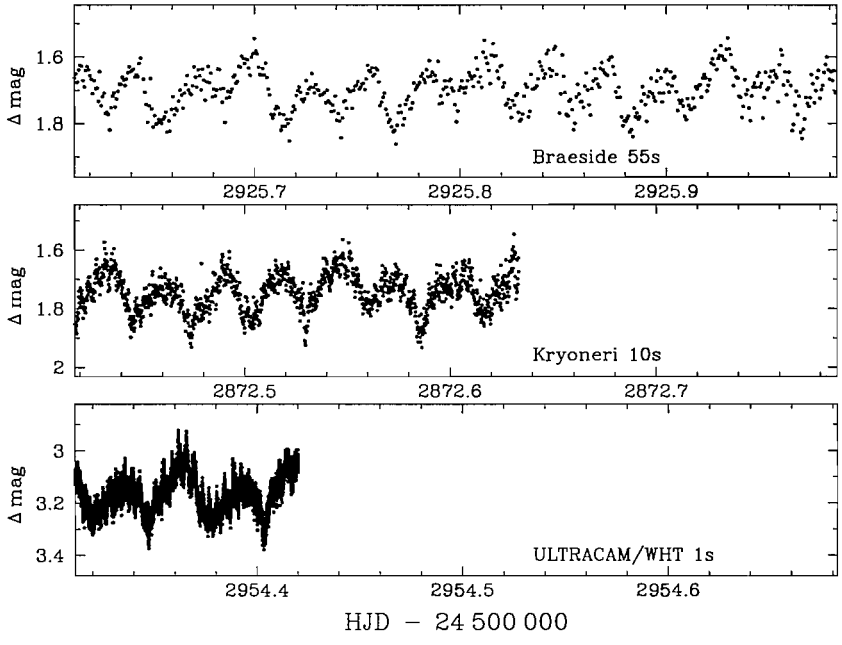

Figure 6.2: Samples of the light curves of HS 2331 obtained from differential CCD photometry at the Braeside Observatory (55 s; top panel), at the Kryoneri Observatory (10 s; middle panel), and at the WHT (1 s; bottom panel).

6.2.2 Optical Spectroscopy

6.2.2.1 2.2 m Calar Alto

HS 2331 was identified as a CV from low-resolution spectroscopy obtained at the Calar Alto 2.2 m telescope on September 20 2000. The CAFOS focal reductor spectrograph was used in conjunction with the standard SITe CCD. A single pair of blue/red identification spectra were obtained with the B-200 and R-200 grating respectively, and through a 2″ slit (see Table 6.2). The wavelength range of the combined spectra extends from 3500 to 10 000 Å at a spectral resolution of approximately 10 Å. The online reduction of the identification spectra using the CAFOS quick look context within MIDAS, immediately revealed the CV nature of HS2331 by the presence of broad double peaked Balmer and He I emission lines in the spectra.

Table 6.2: Log of Spectroscopic Observations.

Date	UT Time	Data	Exp.(s)	#Spectra	Observer[a]
2.2 m Calar Alto/CAFOS					
2000 Sep 20	00:50	B-200	600	1	BTG
2000 Sep 20	01:05	R-200	600	1	BTG
2000 Sep 23	21:14 - 02:39	B-100	600	24	BTG
2000 Sep 24	00:16 - 03:46	B-100	600	16	BTG
2000 Sep 24	03:47 - 04:27	R-100	600	3	BTG
2003 Sep 11	22:16 - 24:02	G-100	600	9	Service
2003 Sep 12	00:14 - 04:19	G-100	600	19	Service
2003 Sep 16	02:27 - 04:35	G-100	600	12	Service
2.5 m INT/IDS					
2002 Aug 27	02:36 - 03:59	R632V	600	9	SAB
2002 Aug 29	00:33 - 01:56	R632V	600	9	SAB
2002 Sep 02	04:16 - 04:47	R632V	600	4	SAB
2002 Sep 03	03:09 - 03:40	R632V	600	4	SAB
HST/STIS					
2002 Oct 24	11:34	G140L	700	1	
2.4 m MDM Hiltner					
2003 Oct 12	07:34 - 08:28	600	420	7	JT
2003 Oct 13	07:44 - 08:31	600	420	6	JT
2003 Oct 14	08:10 - 09:12	600	420	8	JT
2003 Oct 15	02:57 - 11:01	600	420	21	JT
2003 Oct 16	03:51 - 04:53	600	420	8	JT

[a] BG: Boris Gänsicke, SAB: Sofía Araujo-Betancor, JT: John Thorstensen

Time-resolved follow-up spectroscopy of HS2331 was carried out during the same observing run, on September 23 & 24 2000. A total of 43 spectra of 600s each were obtained during the two nights, which were mainly photometric except for very thin cirrus during the last $\sim$ 1.5 hours of the second night (Table 6.2). The B-100 grism was used along with a 1.5″ slit width to obtain 40 spectra with a useful wavelength range of 3500–6300 Å and a spectral resolution of $\sim$ 4 Å. In addition, 3 red spectra were acquired during the second night, using the R-100 grism with a 1.5″ slit width. The red spectra cover a wavelength range of 6000 to 9200 Å at a spectral resolution of $\sim$ 4 Å. Mercury-cadmium, helium-argon and rubidium arcs were taken regularly throughout both nights to provide for the wavelength calibration. Data from the flux standards G191B2B and Zeta Cas were also obtained to correct for the instrument response of the "blue" and "red" spectra respectively. In addition CAFOS requires an acquisition image to be taken in order to properly center the object into the slit. This image, taken with a Johnson V filter was used to rectify our spectra for any slit losses not taken into account in the flux calibration process.

A further set of observations were obtained in September 2003 at the 2.2 m Calar Alto telescope. This time the G-100 grism was used which together with a slit width of 1.2″ provided a wavelength range of 4240–8300 Å and a spectral resolution of $\sim$ 4.1 Å (Table 6.2).

6.2.2.2 2.5 m Isaac Newton Telescope

A total of 26 spectra of 600 s each, spread out over a week, were obtained in August-September 2002 (Table 6.2). We used the Intermediate Dispersion Spectrograph (IDS) on the 2.5 m Isaac Newton Telescope (INT), at the Roche de los Muchachos observatory in La Palma. The IDS was equipped with the R632V grating and the 2048 $\times$ 4100 pixel EEV10 detector. Using a slit width of 1.5″ the setup provided an unvignetted wavelength

range of $\sim 4400\,\text{Å} - 6800\,\text{Å}$ and a spectral resolution of $\sim 2.3\,\text{Å}$. Copper-Argon wavelength calibrations (arcs) were obtained at the beginning and end of each observation block of HS 2331.

6.2.2.3 2.4 m Hiltner telescope

Most recently, John Thorstensen observed HS 2331 from the 2.4 m Hiltner telescope at MDM observatory (Table 6.2). He obtained a total of 50 spectra of 420 s each in October 2003. The modular spectrograph combined with the 600 line mm^{-1} grating and a SITe 2048×2048 CCD detector, yielded a spectral dispersion of $\sim 2.0\,\text{Å pixel}^{-1}$ from 4000 to 7500 Å.

6.2.2.4 Reduction

The reduction technique applied to the last set of data (October 12–16 2003; see Table 6.2) is as explained in Thorstensen et al. (1998). The remaining spectra were reduced in a standard manner using the `Figaro` package within the Starlink software collection. The bias level was subtracted from the calibration and object images using the median from a set of unexposed frames. Dome (for the Calar Alto/CAFOS data) or sky (for the INT/IDS data) flat-field images, taken with the same set up as the object frames, were used to remove pixel to pixel variations. The spectra were then optimally extracted (Horne 1986) and sky line subtracted using Tom Marsh's `Pamela` package. A fourth-order polynomial (a fifth-order for the Sep 2000 CAFOS data; Table 6.2) was fitted to obtain the wavelength-pixel relationship for each of the arc spectrum, given a rms smaller than 0.1 Å in all cases. Each target spectrum was then wavelength-calibrated by interpolating two neighboring arc spectra to ensure an accurate wavelength-pixel scale.

The instrumental response function of the B-100/R-100 spectra (Calar Alto/CAFOS-

September 2000 data) was computed as the ratio of a spline fit to the line-free continuum of the flux standards to flux-calibrated data from Filippenko & Greenstein (1984) and Oke (1990). All B-100/R-100 target spectra were flux-calibrated using this response function, as well as corrected for atmospheric extinction. A grand average spectrum of HS 2331 was created by combining the mean of all "blue" and "red" spectra from the flux-calibrated (and corrected for atmospheric extinction) B-100/R-100 data set. This average spectrum was then scaled to the V-band aperture photometry obtained from the CAFOS acquisition image, $V = 16.4$, to account for possible slit losses. The applied correction of $\simeq 0.2$ mag is comparable to the intrinsic variability of HS 2331, and indicates that the error in our flux calibration is $\leq 20\,\%$.

The combined average of the flux-calibrated "blue" and "red" of HS 2331 shown in Fig. 6.3, displays broad double-peaked Balmer and He I emission lines, suggesting an origin in the accretion disc. The higher series of the Balmer lines are flanked by extremely broad absorption troughs, which are, at first sight, reminiscent of the Stark-broadened absorption lines observed in the high-gravity atmospheres of cool white dwarfs (the width of the absorption lines are too wide to be of accretion disc origin). The red part of the spectrum does not contain any spectral features that could be ascribed to the emission of the secondary star.

6.2.3 *FUV* spectroscopy

FUV spectroscopy of HS 2331 was obtained with the HST/STIS, on October 24, 2002 as part of an ongoing snapshot survey of CVs. The observations were obtained using the G140L grating and the $52'' \times 0.2''$ aperture, providing a spectral resolution of $R \approx 1000$ over the wavelength range $1150 - 1710$ Å. The data were pipeline-processed within IRAF using CALSTIS V2.13b. The calibrated STIS spectrum (Fig. 6.4) contains the mixture of low and high-ionization emission lines often observed in CVs: C III λ1176, Si III λ1206,

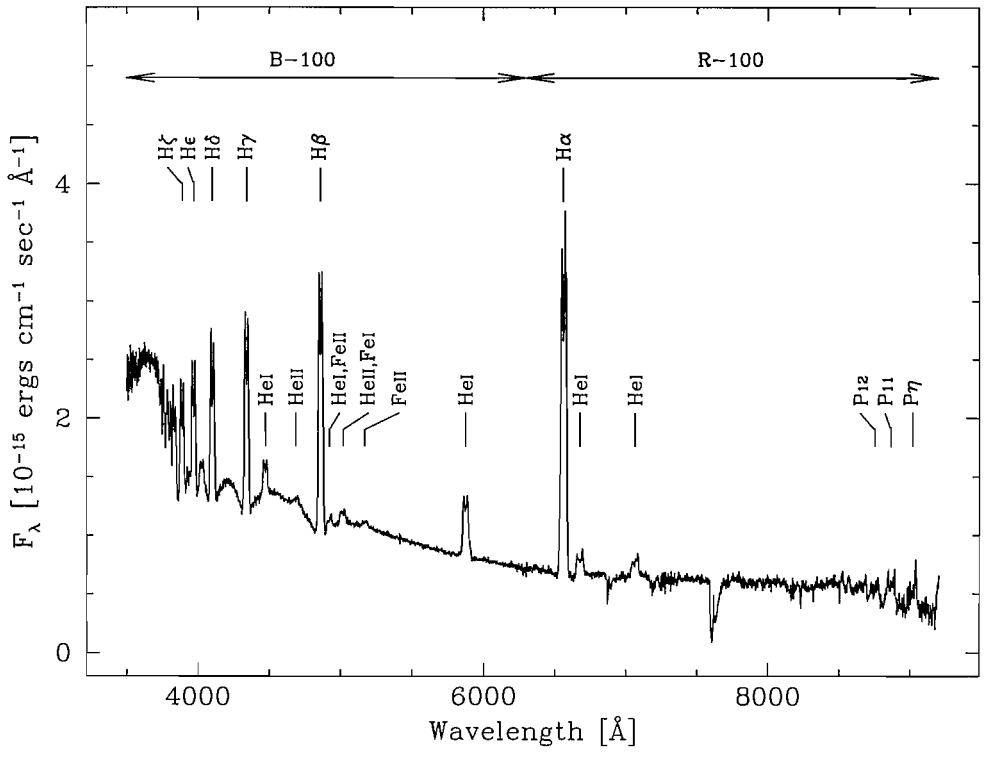

Figure 6.3: Mean- "blue" and "red" flux-calibrated spectra combined together. The arrows define the wavelength range covered by the two gratings, B-100 and R-100 (from the Calar Alto/CAFOS-September 2000 data).

N V λλ1239,43, C II λ1335, a broad complex of Si III near 1300 Å Si IV λλ1394,1403, C IV λλ1548,51 and probably He II λ1640. The emission line flux ratios are within the normal range observed in CVs (Mauche et al. 1997; Gänsicke et al. 2003). Several of the lines contained in the STIS are double-peaked, suggesting again an origin in an accretion disc. The continuum flux underlying the emission lines is slightly increasing towards the red, with a sudden upturn in flux at wavelengths $\lambda \gtrsim 1650$ Å, which we identify as the white dwarf contribution to the *FUV* range of the HS 2331 SED .

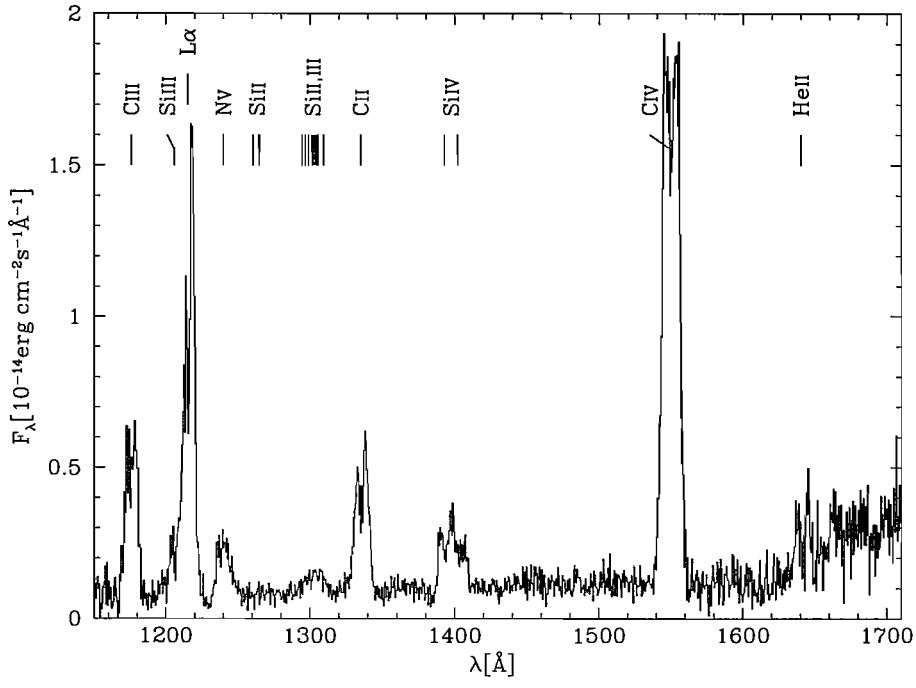

Figure 6.4: HST/STIS spectrum of HS 2331. See text for details.

6.3 Analysis

6.3.1 Photometry

We have computed a Scargle periodogram (Scargle 1982) from the entire CCD photometry of HS 2331, using the MIDAS context TSA. Prior to this period analysis, we have subtracted the nightly mean of each light curve to account for night-to-night variations in the overall brightness of the system and of the different detectors/filters used during the observations. Fig. 6.5 displays the computed periodogram: the strongest peak is located at $35.52\,\mathrm{d}^{-1}$ (40.54 min), a weaker signal is centred on $\sim 17.27\,\mathrm{d}^{-1}$ (83.38 min), and some power is also found at $53.28\,\mathrm{d}^{-1}$ (27.03 min) and $71.04\,\mathrm{d}^{-1}$ (20.27 min). In the high-frequency range there is a strong peak at $1284.72\,\mathrm{d}^{-1}$ (1.12 min) and a weaker one at $256.63\,\mathrm{d}^{-1}$ (5.61 min).

Fig. 6.6 shows a close-up view of the Scargle periodograms around the ~40 min (right

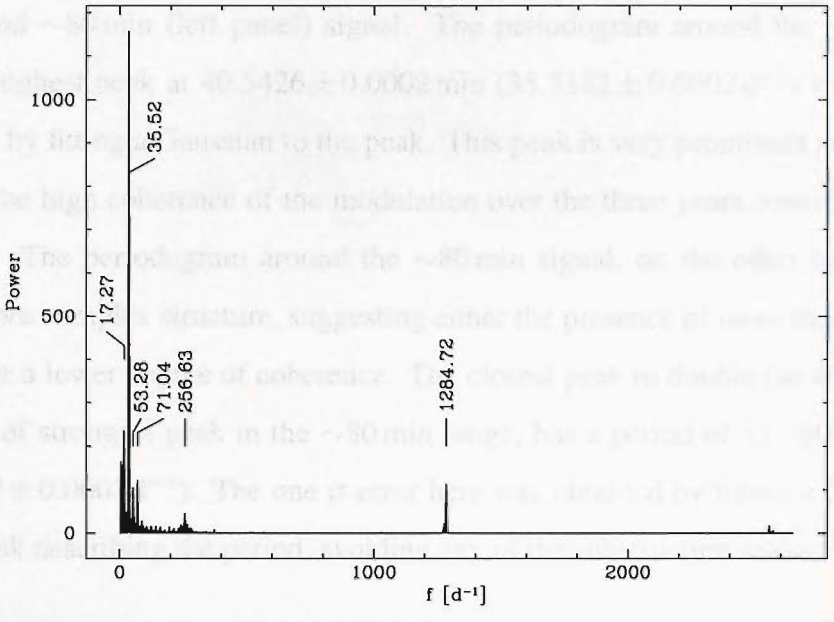

Figure 6.5: Scargle periodogram of the combined CCD photometry of HS 2331. See text for details.

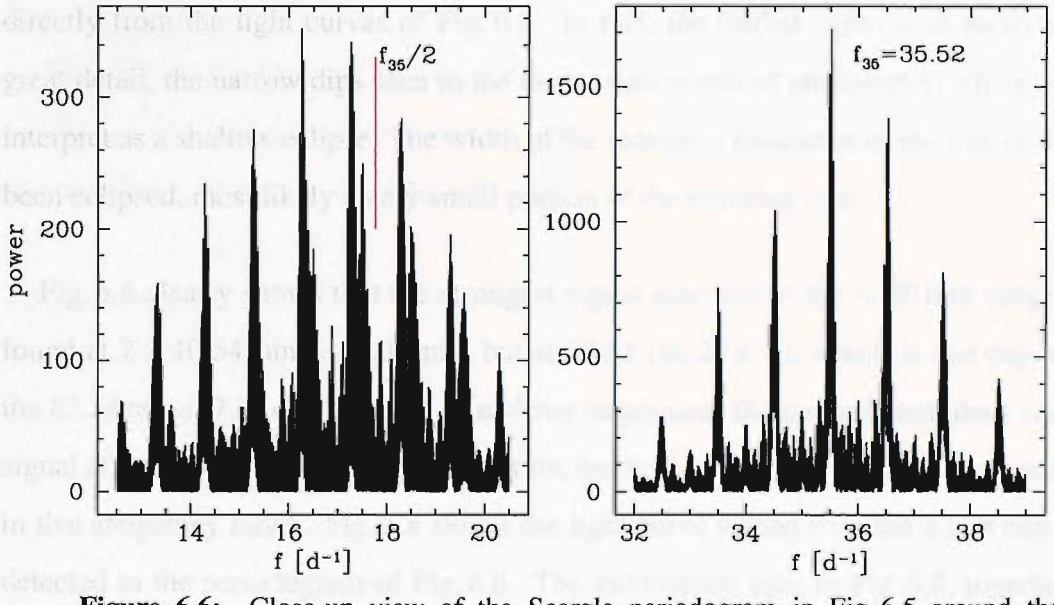

Figure 6.6: Close-up view of the Scargle periodogram in Fig. 6.5 around the ∼40 min signal (right panel; highest peak at 35.52 d^{-1} or 40.54 min), and around the ∼80 min signal (left panel; highest peak is at 16.27 d^{-1} or 88.51 min separated by one day aliases from the second highest peak at 17.27 d^{-1} or 83.38 min). The red line in the left panel marks the location of exactly double the ∼ 40 min period (i.e. 17.76 d^{-1} or 81.08 min).

panel) and ~80 min (left panel) signal. The periodogram around the ~40 min signal has the highest peak at 40.5426 ± 0.0002 min ($35.5182 \pm 0.0002\,d^{-1}$) with one σ error obtained by fitting a Gaussian to the peak. This peak is very prominent and narrow confirming the high coherence of the modulation over the three years covered by the entire data set. The periodogram around the ~80 min signal, on the other hand, displays a much more complex structure, suggesting either the presence of more than one periodicity and/or a lower degree of coherence. The closest peak to double the 40.54 min signal and one of strongest peak in the ~80 min range, has a period of 83.3806 ± 0.0002 min ($17.2702 \pm 0.0002\,d^{-1}$). The one σ error here was obtained by fitting a Gaussian to the finest peak describing the period, avoiding any of the substructure around it.

When the entire data set is folded over a period exactly double the 40.54 min signal, i.e. 81.08 min, (see Fig. 6.7), the result clearly recreates the form of the modulation seen directly from the light curves of Fig. 6.2. In fact, the folded light curve reproduces in great detail, the narrow dips seen in the three years worth of photometry, which we now interpret as a shallow eclipse. The width of the feature is indicative of the size of the area been eclipsed, most likely a very small portion of the emitting area.

Fig. 6.6 clearly shows that the strongest signal detected in the ~ 80 min range is not found at $2 \times 40.54\,\text{min} = 81.08\,\text{min}$, but at 88.51 ($16.27\,d^{-1}$), which is one day alias of the 83.38 min ($17.27\,d^{-1}$) signal. At a closer inspection, the periodogram does contain a signal at exactly $2 \times 40.54\,\text{min} = 81.08\,\text{min}$, but it is weak compared to the other signals in that frequency range. Fig. 6.8 shows the light curve folded over the 83.38 min signal detected in the periodogram of Fig. 6.6. The modulation seen in Fig. 6.8, together with our result from Fig. 6.7, clearly supports our initial interpretation for the more complex structure of the periodogram on the left side in Fig. 6.6, namely the presence of more than one periodicity in that frequency range. The remaining periods detected in the low-frequency range, i.e. $53.28\,d^{-1}$ (27.03 min) and $71.04\,d^{-1}$ (20.27 min), are harmonics of the 81.08 min signal.

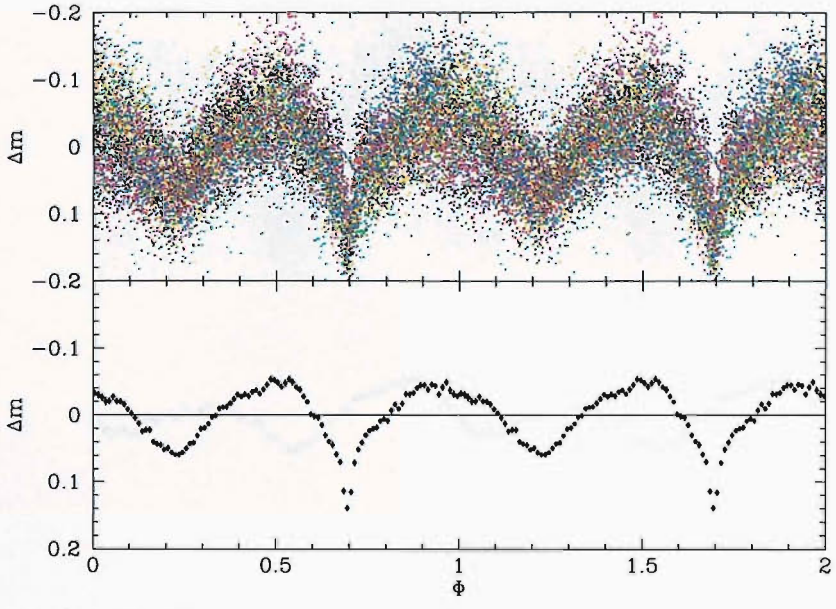

Figure 6.7: HS 2331 entire photometric data set folded over 81.08 min (upper panel) and re-sampled into bins of 100 points (bottom panel). The light curves are repeated over two cycles for clarity.

The shallow but coherent eclipses detected in the folded light curve of Fig. 6.7 (which are also seeing directly, although not as evident, in the light curves of Fig. 6.2), strongly suggest that 81.08 min is the orbital period of the system. We favour this period over the 83.38 min, (the next closest peak in the Scargle periodogram on the left side of Fig. 6.6) because the result of folding the photometric data set over the 83.38 min period is a modulation which is smooth but without the eclipses. If the 81.08 min signal is indeed the orbital period of the system, then the 83.38 min signal is in the right frequency range to represent a superhump period. Systems with such short periods are expecting to have superhumps of periods about 1-2% longer than the orbital period, which is exactly what we observe.

We now concentrate on the high-frequency range of the periodogram of Fig. 6.5 and have a closer look at the strongest peaks at this region: at 1.12 min (1284.72 d^{-1}; right panel of Fig. 6.9) and at 5.61 min (256.63 d^{-1}; left panel of Fig. 6.9). The periodogram around the ∼1 min signal displays a structure similar to that found in ZZ Ceti pulsators

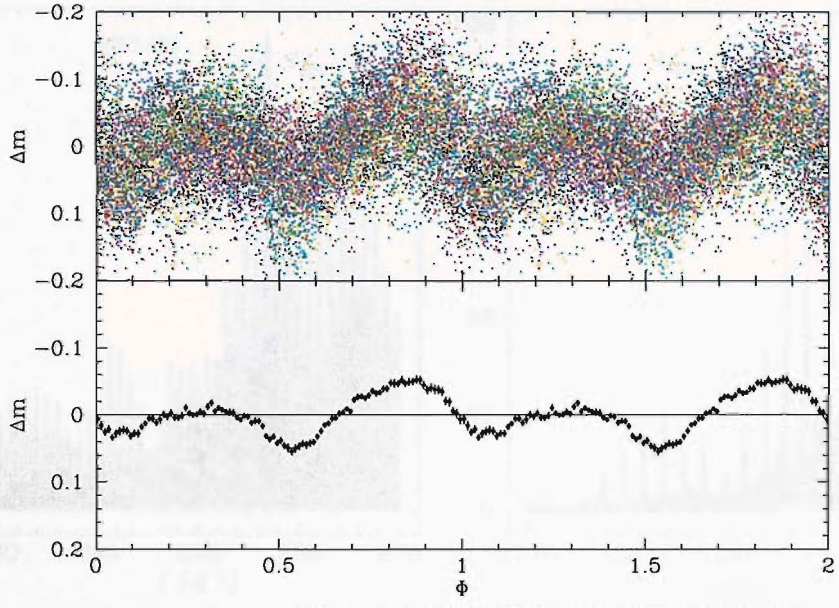

Figure 6.8: HS 2331 entire photometric data set folded over 83.38 min (upper panel) and re-sampled into bins of 100 points (bottom panel). The light curves are repeated over two cycles for clarity.

power spectra with two clearly distinct signals (see van Zyl et al. 2000). ZZ Ceti stars are non-radially pulsating white dwarfs with a hydrogen-rich atmosphere. They are found to vary in a narrow range of effective temperatures, $12\,500 \geq T_{\rm eff} \geq 10\,700$ K, showing multiperiodic variations with amplitudes reaching up to ∼0.3 mag and periods ranging from ∼100 to ∼1200 s. The periodogram of the left hand side panel of figure Fig. 6.9 shows an extremely complex structure indicative of a combination of many frequencies. Indeed, ZZ Ceti pulsators have power spectra similar to the one shown in Fig. 6.9. These complex patterns can be explained by a number of pulsation modes, their harmonics, and various linear combinations of modes (e.g. Kotak et al. 2002).

6.3.2 Spectroscopy

Radial velocities were measured using the "rvel" MOLLY routine which is based on the convolution technique first outlined by Schneider & Young (1980) and developed

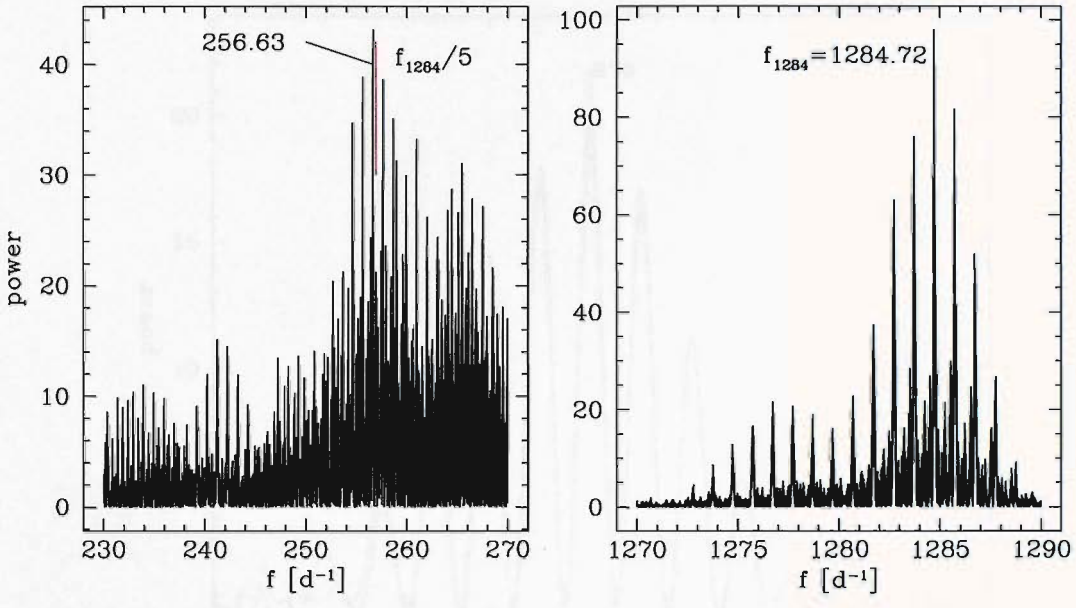

Figure 6.9: Close-up view of the Scargle periodogram in Fig. 6.5 around the 1 min signal (right panel; highest peak at 1284.72 d^{-1} or 1.12 min), and around the 5 min signal (left panel; highest peak at 256.63 d^{-1} or 5.61 min). The red line in the left hand side panel marks the location of exactly five times the 1 min period (i.e. 256.94 d^{-1} or 5.60 min).

by Shafter (1983). The emission line profile is convolved with two Gaussians of equal FWHM (of the order of the wavelength resolution) but opposite signs. The peaks of the Gaussians are separated by a distance chosen in order to measure as far out as possible into the wings, while still retaining an adequate signal to noise level. By doing this we ensure that the measured radial velocities trace the inner part of the accretion disc, which is most likely to be azimuthally symmetric and trace the radial velocity of the white dwarf. The point were the convolution equals zero (the positive and negative contributions cancel out) is taken to be the center of the line.

We first computed radial velocity variations from the first follow-up data set obtained on September 23 & 24 2000, with the B-100 grism at the 2.2 m Calar Alto telescope (see Table 6.2). These data account for a total of 40 spectra taken over two consecutive nights, providing more than 5 h continuous coverage in the first night. Radial velocity

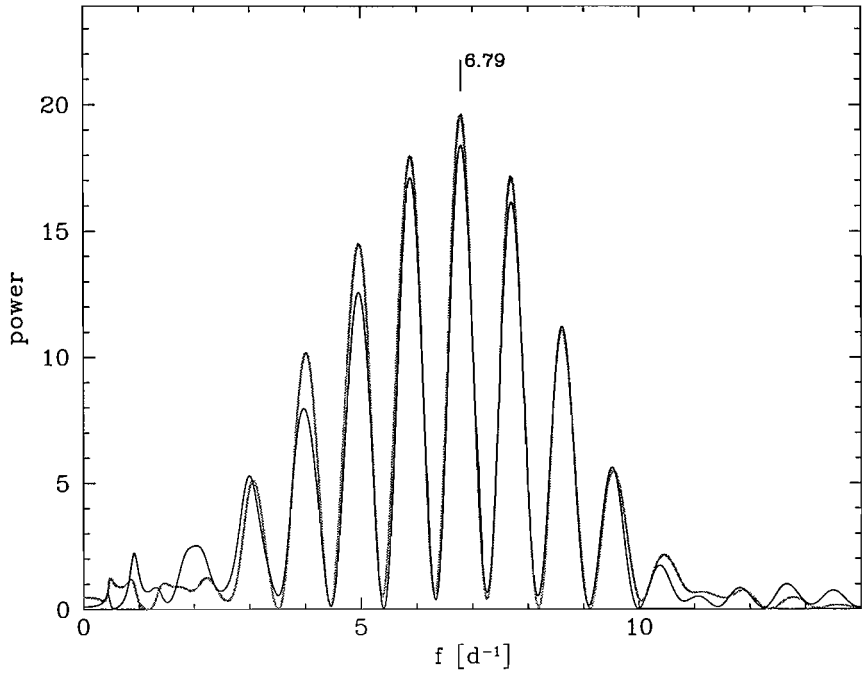

Figure 6.10: Shown in black is the Scargle periodogram of the Hγ radial velocity variations measured from the 40/B-100 spectra obtained in September 2000 (see Table 6.2). Shown in grey is the Scargle periodogram of faked data created with a frequency of $6.79\,\mathrm{d}^{-1}$ (3.53 h) and same sample pattern and similar errors as the real data.

measurements computed from these 40 spectra are, therefore, adequate for the estimation of the orbital period of the system. After rebinning both nights spectra onto a uniform velocity scale we obtained the radial velocity measurements for almost all the Balmer lines included in the B-100 spectral range, He I λ5875 and He I 4471. In all cases the peaks of the two equal Gaussians (FWHM = 260 km/s) were separated by a distance of 2500 km/s. The radial velocity measurements were then subjected to the Scargle period analysis as implemented by the MIDAS context TSA (Scargle 1982). Figure 6.10 shows the periodogram obtained from the radial velocity measurements of Hγ (dark line). A Gaussian was fitted to obtain a highest peak value with one σ error of $6.79 \pm 0.1\ \mathrm{d}^{-1}$ (3.53 ± 0.05 h). Plotted in grey is the computed periodogram of a sinusoid with a period of 3.53 h ($6.79\ \mathrm{d}^{-1}$), similar amplitude and same sampling pattern as the original radial

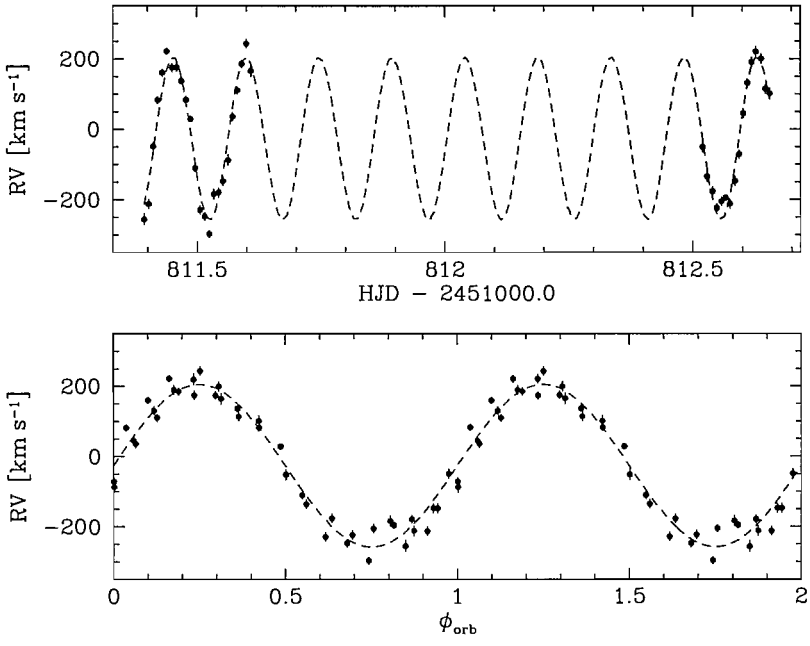

Figure 6.11: *Top*: Unfolded Hγ radial velocities measured from the 40/B-100 spectra obtained during two consecutive nights (see Table 6.2). The best-fit sinusoid with a period of 3.53 h (6.79 d^{-1}) is also shown. *Bottom*: Hγ radial velocity curve and sinusoid (same as above) folded over the found 3.53 h (6.79 d^{-1}) periodicity. All data are plotted twice for continuity. Phase zero has been chosen to be the point at which the velocities cross from blue to red.

velocity measurements. Errors of the same size as those of the original radial velocity data set were added with random signs. The power spectrum of the faked data set clearly confirms our detected period.

The top panel of Figure 6.11 shows the radial velocity curve of Hγ with a best-fit sinusoid of period 3.53 h (6.79 d^{-1}). The bottom panel displays the same data but this time folded on the 3.53 h period (6.79 d^{-1}). The analysis of the rest of the Balmer lines, He I λ5875 and He I λ4471 gave similar results to Hγ. We chose Hγ for the simple reason that Hα was not contained in the B-100 spectra, and Hβ suffers more from contamination of the white dwarf absorption component and from neighbouring He I emission lines than any other line (see Fig. 6.3). It is important to point out that if we did not have the photometry at this point we would have concluded, without a doubt, that 3.53 h was truly

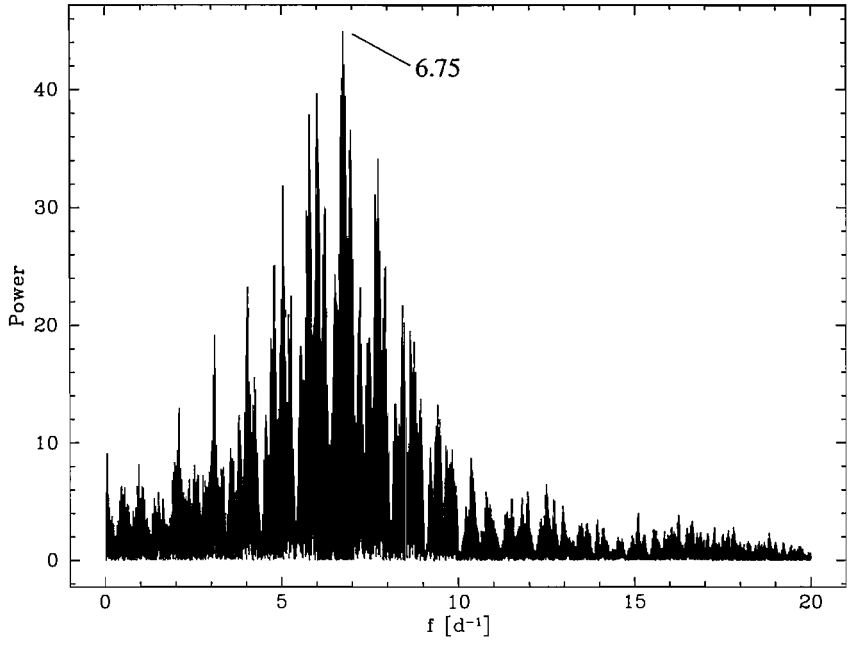

Figure 6.12: Scargle periodogram of the radial velocities of Hγ obtained from the entire spectral data set.

the orbital period of the system. This may have important implications for orbital period determinations in a wider context. It is customary in the field of CVs (and related systems such as LMXBs) to adopt the dominant radial velocity periodicity as the orbital period of the system, especially in cases like HS 2331, where the radial velocity curve is very sinusoidal. The results obtained for HS 2331 are a clear warning that this custom could occasionally lead to wrong interpretations.

When the same analysis is performed on the rest of the spectral data set (excluding the 3/R-100 spectra which do not contained Hγ, and the identification spectrum) we obtained a different result. Fig. 6.12 shows the Scargle periodogram obtained from the Hγ radial velocity variations of the entire data set. The periodogram exhibits a much more complex structure, which one might be tempted to ascribe to the poor sampling of the radial velocity data. The strongest signal is found at $6.76 \pm 0.2\,\mathrm{d}^{-1}$ (3.55 h) consistent within the errors of the frequency found from the B-100 spectral set alone (i.e. $6.79 \pm 0.1\ \mathrm{d}^{-1}$). However, when the radial velocity measurements are folded over this 3.55 h period, all

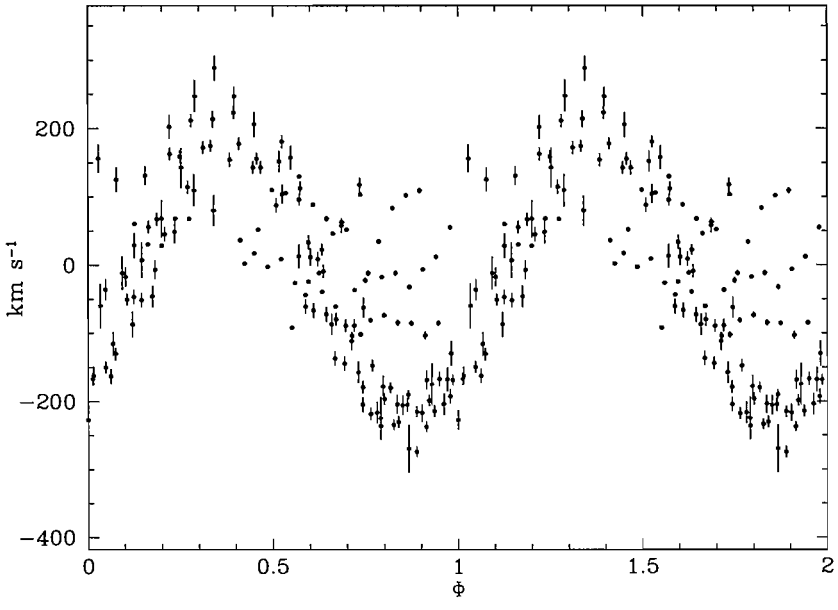

Figure 6.13: Radial velocity curve of the entire spectroscopic data set folded over a period of 3.55 h. The individual data sets are shifted relative to each other.

the individual data sets are shifted relative to each other (see Fig. 6.13). A careful period analysis of the entire radial velocity data set, as well as of the individual sets (2×Calar Alto, INT, MDM), shows that there is no unique period that will result in a satisfactory folded radial velocity curve. We conclude that a persistent large-amplitude radial velocity variation with a period ∼3.5 h is present in HS 2331, however, this variation is not coherent and its period drifts on time scales of days.

Returning to our Calar Alto B-100 observations, which provides the densest sampling of our spectroscopic data sets, we subtract the 6.79 signal detected in the periodogram of Fig. 6.10. The Scargle periodogram of this detrended data set (Fig. 6.14), exhibits a strong signal at 81.08 min, which coincides with the photometric period established in Sec. 6.3.1. Folding the detrended radial velocities over the 81.08 min period results in a sinusoidal radial velocity curve with an amplitude of $\simeq 50\,\mathrm{km\,s^{-1}}$ (Fig. 6.15), which is typical for short-period systems. The consistent detection of the 81.08 min period both in the photometry and in the spectral radial velocity variations lends further support for our hypothesis that this is indeed the orbital period of HS 2331.

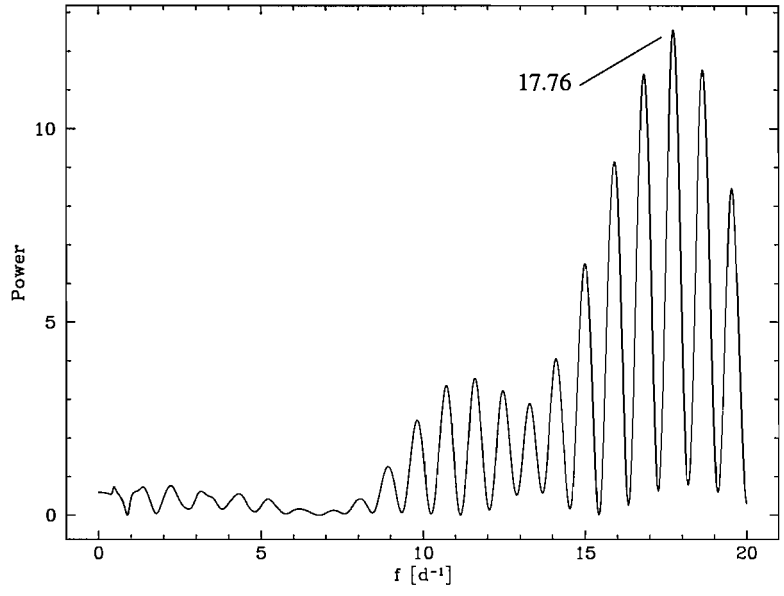

Figure 6.14: Scargle periodogram of the Hγ radial velocities obtained from the B-100 data set alone, after subtracting a 3.53 h sinusoid signal (i.e. the highest peak in Fig. 6.10). The new highest peak is at 17.76 d^{-1} (81.08 min) which is in agreement with the period found in the photometry and the one we favour as the orbital period of the system.

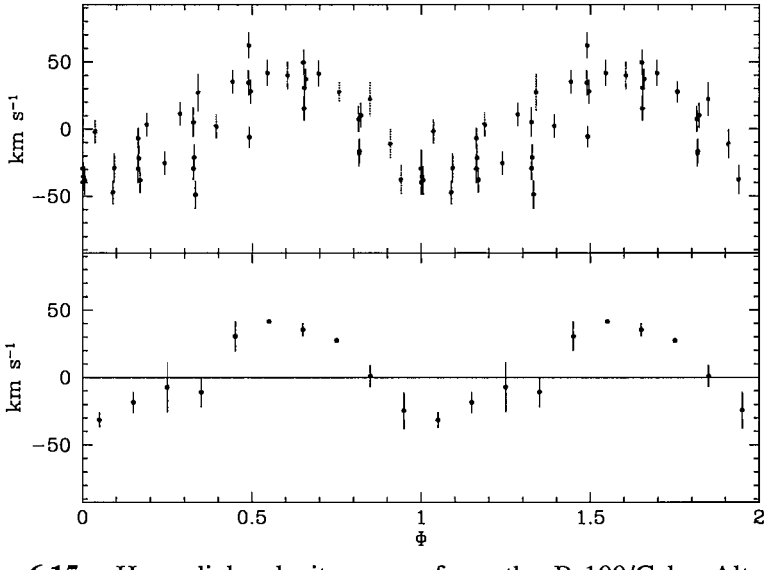

Figure 6.15: Hγ radial velocity curve from the B-100/Calar Alto data set of HS 2331, folded over ∼ 81.08 min after subtraction of the 3.53 h sinusoidal signal (i.e. the highest peak in Fig. 6.10).

6.3.2.1 Modeling of the SED

We have fitted the SED (a combination of *FUV*, optical spectra and 2MASS colours of HS 2331) with a three-component model, combining synthetic white dwarf spectra, the emission of an isothermal and isobaric pure hydrogen slab, and observed templates of late-type stars.

The synthetic spectra for the white dwarf were constructed with fixed surface gravity of $\log g = 8.0$, and different temperatures ($T_{\rm eff}$) and solar abundances, using the TLUSTY and SYNSPEC codes (Hubeny 1988; Hubeny & Lanz 1995). The emission of an isothermal and isobaric slab with a finite depth was computed using the method described by Gänsicke et al. (1997). The free parameters for the generation of the grid of slab models were the temperature and the column density of the slab along the line of sight. The temperature accounts for the ionisation/excitation of the lines and the optically thick blackbody envelope, and the column density determines the ratio in optical depth between continuum and lines. Red spectra templates from M- and L-dwarf stars were collected from Beuermann et al. (1998), Kirkpatrick et al. (1999) and Kirkpatrick et al. (2000) to account for the flux and spectral features of the secondary (see Fig. 1.7 and Fig. 1.8). The L-dwarf type stars were normalized to surface fluxes using the radius and distance given by Dahn et al. (2002) while the M-dwarf set were already normalized in this way.

We started by matching the optical broad absorption lines detected in the optical spectrum with the white dwarf models, which suggested a temperature around 10 000 K. We then varied the temperature of the white dwarf by small amounts to reproduce the sudden upturn seen in the red region of the *FUV* spectra. An 11 000 K white dwarf provides the best overall agreement with the optical and *FUV* observations. The white dwarf model accounts for $\sim 80\%$ of the flux in the optical. If we add a 6500 K isothermal and isobaric slab of surface density $1.81 \times 10^{-2}\,{\rm g\,cm^{-2}}$, column thickness $7 \times 10^{7}\,{\rm cm}$ and pressure $100\,{\rm dyn\,cm^{2}}$, then we need a L2 donor star or later as shown in Fig. 6.16. Our simple

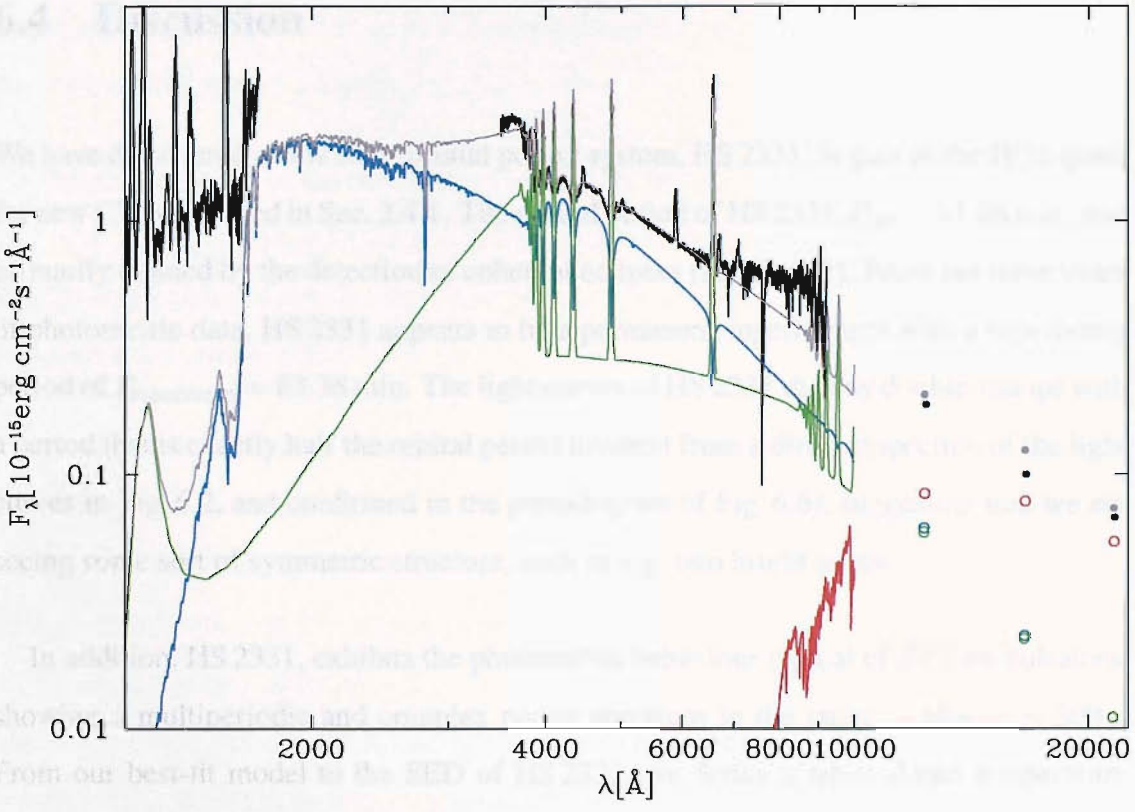

Figure 6.16: Combination of *FUV*, optical spectra and 2MASS colours of HS 2331 (dark line and dark filled circles) plotted with the combination of the three components that best match the data: a model for the white dwarf (blue line and open blue circles), a model for the accretion disc (green line and open green circles) and a template spectrum for the secondary of spectral type L2 (red line and red open circles). The grey line and filled grey circles are the result of adding all three components. Note the logarithmic scale in the x-axis.

isothermal and isobaric slab model for the disc emission contributes about 20% of the total optical flux. The mis-match between the data and the model seen both at *FUV* wavelengths and at the red end of the optical spectrum Fig. 6.16 suggests that our single temperature model for the accretion disc is almost certainly due to Pachen jump in emission. The scaling factor of the white dwarf model gives a distance to the system of 110 ± 20 pc. At that distance, the area of the isothermal slab component is comparable to the Roche lobe of the white dwarf.

6.4 Discussion

We have discovered a new short orbital period system, HS 2331, as part of the HQS quest for new CVs described in Sec. 2.4.1. The orbital period of HS 2331, $P_{\rm orb} = 81.08$ min, was primarily defined by the detection of coherent eclipses (see Fig 6.7). From our three years of photometric data, HS 2331 appears to be a permanent superhumper with a superhump period of $P_{\rm superhump} = 83.38$ min. The light curves of HS 2331 display double-humps with a period that is exactly half the orbital period (evident from a direct inspection of the light curves in Fig. 6.2, and confirmed in the periodogram of Fig. 6.6), suggesting that we are seeing some sort of symmetric structure, such as e.g. two bright spots.

In addition, HS 2331, exhibits the photometric behaviour typical of ZZ Ceti pulsators, showing a multiperiodic and complex power spectrum in the range ~ 60 s to ~ 300 s. From our best-fit model to the SED of HS 2331, we derive a white dwarf temperature of 11 000 K which is well within the instability strip for ZZ Ceti pulsators. If HS 2331 contains a pulsating white dwarf of ZZ Ceti type, then we are witnessing a quite unusual system in this regard. We are only aware of another confirmed CV possessing the same type of white dwarf pulsators, GW Lib (van Zyl et al. 2000). GW Lib is only partially understood, due to the lack of a proper mode identification of the observed pulsation frequencies, and more severely, due to the circumstance that the temperature of its white dwarf, $T_{\rm eff} = 14\,700$ K, is actually significantly outside the instability strip. This only confirms the need to study this type of systems in more detail. Specifically, the process driving the pulsations may work differently in accreting white dwarfs compared to isolated ZZ Ceti stars, due to the presence of large amounts of metals in the envelope. In order to disentangle the multiperiodic signature of the likely white dwarf pulsator in HS 2331, we need to organize a multi-site observing campaign to obtain long, continuous stretches of high time resolution photometry.

Our best model for the red dwarf in HS 2331, assuming it contains an 11 000 white

dwarf as the primary, is that of an L2-spectral type or later, which is what it is expected for short orbital period systems.

The scaling factor of the white dwarf used to fit the SED of HS 2331 implies a distance of 110 ± 20 pc. From the DSS1 and DSS2 images of the HS 2331 field of view we were able to determine the proper motion of the system, $\mu = 0.14'' \mathrm{yr}^{-1}$ which independently suggests a low distance to HS 2331.

All in all, the pieces of the puzzle seems to come together, and we are beginning to understand the nature of HS 2331. There are nevertheless, several points that we still need to address. The fact that the dominant radial velocity variability does not correspond to the orbital period of the system is particularly disconcerting. At present, we have no explanation for this phenomenon, nor for the physical significance of the 3.5 hr radial velocity period. We are not aware of any other system suffering from this problem, but the reason for this may be that periods determined from radial velocity studies are usually adopted unquestioned as reflecting the corresponding orbital periods. HS 2331 teaches us that the habit of interpreting an observed sinusoidal radial velocity variation as a tracer of the orbital period may sometimes be misleading.

I will close this chapter by reiterating the need to follow up HS 2331 in detail to be able to confirm or reject the permanent superhump idea that is our currently favoured explanation for the 83.38 min signal. The ZZ Ceti behaviour also needs further investigation. More specifically, we need to identify the individual signals and their combinations in terms of pulsation modes, which is not an easy or straight forward task to do. Finally, it is critical that we uncover the origin of the 3.5 h incoherent but persistent radial velocity modulation.

Chapter 7

Discussion: Current Status of the Surveys

Most of the work in this thesis is part of a much bigger project whose long-term goal is to establish in detail the properties of the intrinsic CV population of our Galaxy. Of all the CV properties, the orbital period is typically the best determined, and an important aim of the theoretical effort to understand the evolution of CVs is to reproduce the observed orbital period distribution of the known CV population. It is for this reason that our primary aim is to determine the orbital periods of a statistically complete sample of CVs. The properties of this sample can then be used as a major test for the current theories of CV evolution, or as the starting point for the development of alternative theories if the prevailing ones fail the test. This thesis provides some insight into the observational approach towards the building up of an unbiased sample of CVs, which is necessary to derive a statistically complete orbital period distribution.

In Sec. 2.2.1 I considered the severe selection effects involved in the discovery of CVs.

It is clear that X-ray faint systems, CVs with low levels of optical variability, and CVs that are intrinsically faint and/or not particularly blue are most certainly heavily under-represented in the known sample. In order to tackle the problem of selection biases in the current CV population, we, in Southampton, have engaged into a large-scale search for new CVs. The majority of the work presented in this thesis is based on two of the projects which are part of our large-scale search: (1) using the HQS and (2) a combination of ROSAT/2MASS-colour selection scheme. The selection criteria used by these two complementary projects (described in Sec. 2.4) have not been fully exploited before. We should, therefore, be able to find systems which have been overlooked by the previously employed search techniques. As a consequence we should be able to reduce the observational biases of the CV population. While the thesis so far has focussed on a limited number of the systems discovered in the HQS (as well as on the SW Sex star, DW UMa), it is important not to lose sight of the larger goal of the surveys. I will, therefore, take a step back to discuss their current status in the remainder of this chapter.

7.1 HQS

At present, we have discovered a total of 52 new CVs, doubling the number of known CVs in the sky area/magnitude range covered by the HQS (Gänsicke et al. 2000; Nogami et al. 2000; Gänsicke et al. 2002b,c). Another 36 CV candidates are pending confirmation. As described in Sec. 2.4.1, our criterion to select CV candidates from the HQS is based primarily on spectral appearance. This survey should, in principal, provide an efficient means of discovering CVs that were neither detected in X-rays, nor display strong or frequent variability at optical wavelengths. Fig. 7.1 shows the orbital period distribution of those CVs with known periods, 28 systems out of the 52 new CVs.

Our main surprise from our study of the HQS CVs is the large number of new SW Sex

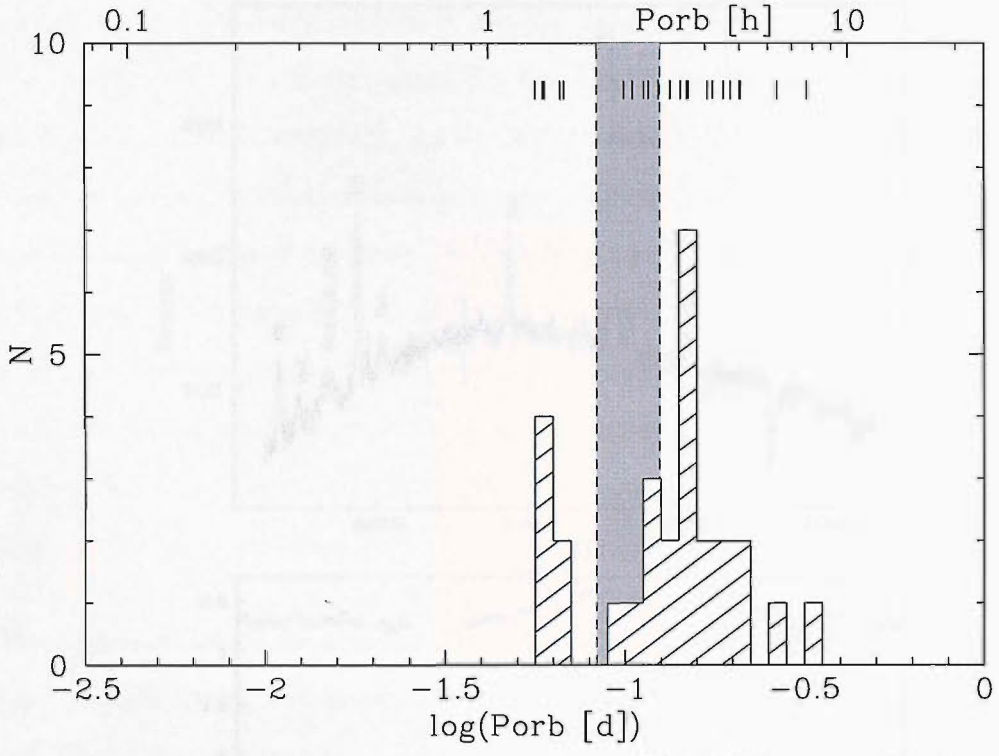

Figure 7.1: Orbital period distribution of the new CVs with known periods discovered in the HQS. The tickmarks indicate the individual periods. Shown in grey is the region in the period distribution corresponding to the period gap.

stars: 5 out of the 28 systems for which the orbital periods have been determined belong to this group (see e.g. HS 0220+0603; Fig. 7.2). All five systems are concentrated above the gap, with periods ranging from 3.2 h to 4 h. All except one, are high inclination systems, exhibiting the V-shaped eclipses and single-peaked Balmer emission lines characteristics of the SW Sex stars. The non-eclipsing system, shows a behaviour similar to the SW Sex star, LS Pegasi (Taylor et al. 1999): Balmer emission lines with broad, asymmetric wings shifted by almost 2000 km/s, displaying, together with He I, the central, phase-dependent absorption typical of SW Sex stars. The discovery of 5 new SW Sex stars represents a substantial growth of this class of objects, bringing the total number of SW Sex systems to about 24. Visual inspection of data (spectroscopy/photometry) for the remaining (confirmed but with unknown orbital period) HQS CVs, strongly indicates that several number of these systems may also be SW Sex stars. Whereas SW Sex stars initially appeared to

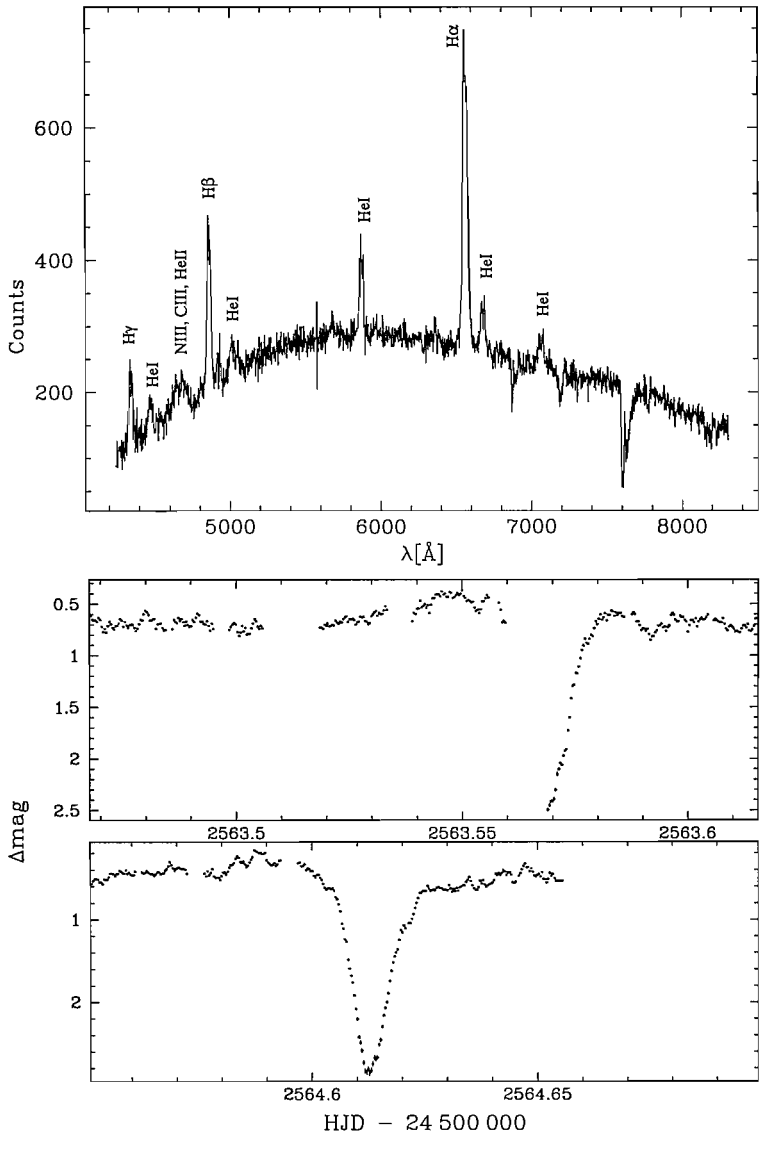

Figure 7.2: *Top panel*: Average of a set of 5 spectra of HS 0220+0603 obtained on December 16 2002, at the 2.2 m Calar Alto telescope, with 600 s time exposure. *Bottom panel*: Light Curve of HS 0220+0603 constructed from 25 s CCD images taken at the 1.2 m Kryoneri telescope. HS 0220+0603 displays the characteristics of SW Sex star: V-shaped eclipses, $P_{\rm orb} \sim 3.6$ h (Rodríguez-Gil; private communication), single-peaked Balmer lines and He I, and high excitation lines (He II λ4686 and C III/N III λλ4640 – 4650).

be the "freaks" among the CVs, they now turn out to be a major CV sub-population. The fact that the majority of these systems have orbital periods concentrated in a very small

region above the period gap, may have important implications to our current understanding of CV evolution. In addition, many SW Sex stars exhibit the low states characteristics of the VY Scl nova-like variables. As already mentioned in Sec. 1.3, these low states are believed to be directly related to the secondary, although at present there is still no firm theoretical basis for this hypothesis. If this hypothesis were true, the low states observed in SW Sex stars and the origin of the period gap are probably connected to a certain extent, making the research on this type of systems essential. With this motive in mind, I have determined a reliable set of the systems parameters of one of the oldest members of the SW Sex class, DW UMa (see Chapter 4; I will come back to this point later in this section).

The dearth of dwarf novae observed in the 3–4 h interval above the gap (the region occupied by the SW Sex systems; see top panel of Fig. 1.5) is also seen among our group of new HQS CVs with known orbital periods. From the 11 objects contained in this range of the distribution of Fig. 7.1, only one has been classified as a dwarf novae. The other objects are a mixture of magnetic systems and nova-like variables, five of which are the SW Sex stars mentioned above. In order to explain the lack of dwarf novae just above the period gap, King (2000) proposed a mass transfer rate cycle for systems concentrated in that region of the orbital period distribution. In their model, the cycle is driven by irradiation of the secondary. To maintain (or assist) the mass transfer rate cycle above the gap, they invoked a consequential angular momentum loss (CAML) mechanism. CAML mechanisms (e.g. disc winds) are themselves a consequence of mass transfer, and only modulate (amplify) the existing mass transfer rate. The dearth of dwarf novae in the range 3–4 h, could then be explained since the most likely objects to be observed – in the orbital period region where the cycle is occurring – are those on the bright part of the cycle, i.e. high-state systems or nova-like variables. Dwarf novae would be those objects in the lowest mass accretion rate regime of the cycle, and therefore would be harder to identify.

King (2000) suggested that the CAML mechanism needed to assist their proposed mass transfer rate cycle, might be associated with the SW Sex phenomenon. To study this interesting idea in more detail we need to collect reliable systems parameters for all systems concentrated in this small region of the orbital period distribution. This has proven to be especially difficult for the SW Sex stars due to their defining characteristics (see Sec. 1.3). In Chapter 4.1 I use one of the sporadic low states exhibited by the SW Sex star, DW UMa, to accurately determine its system parameters. The success of this method is promising, especially for high inclination systems. A large fraction of the SW Sex stars are indeed eclipsing, but this is probably a selection effect: it is easier to spot the SW Sex characteristics in high inclination systems. This means, however, that the fraction of SW Sex stars is probably even larger. In order to exploit the method used in Chapter 4.1 in a systematic way, we should begin by studying the low states in more detail. Particularly, we need to understand whether they are a prevalent feature or just a random occurrence among the SW Sex stars.

The efficiency of using the HQS to identify new CVs is fully discussed in Gänsicke et al. (2002b). In their analysis, the authors use the sample of previously known CVs and CV candidates contained in the HQS sky area. We have carried out this test once more using the known CV population as of September 2003 (Downes et al. 2001; Kube et al. 2002). In doing so, we consider the following effects: (1) the amount of known CVs with spectra outside the dynamical range of the survey at the time of the observations (i.e. $13 \lesssim B \lesssim 18.5$), (2) the uncertainty in the objects coordinates/identification, and (3) the overlap of the prism spectra (which make the identification impossible). We conclude, as Gänsicke et al. (2002b), that about 90% of the known CVs with secure identification and quiescent magnitudes $13 \lesssim B \lesssim 17.5$, were included in the high-resolution HQS database[1]. The number of systems with a high-resolution scan and $17.5 \lesssim B \lesssim 18.5$ drops

[1]Remember that blue objects were originally selected from the low-resolution scan of the HQS. The spectra of those selected were then re-scanned in a high-resolution mode so that a more refined criteria could be employed to find CV candidates (see also Sec. 2.4.1).

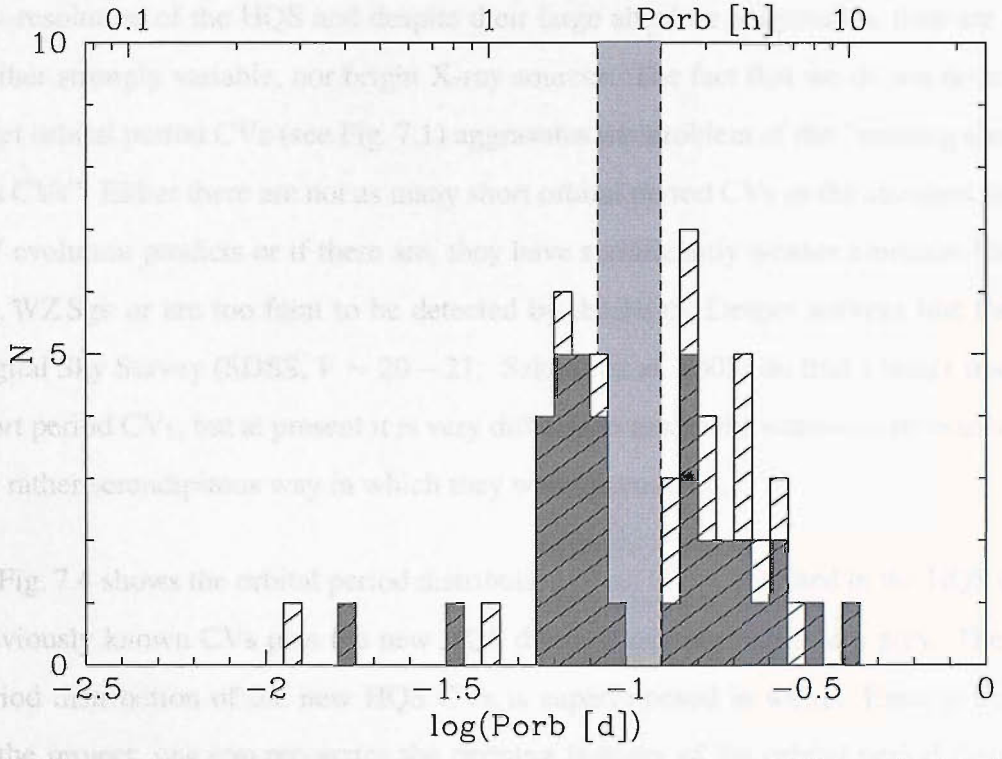

Figure 7.3: Orbital period distribution of the previously known CVs contained in the HQS high-resolution database. Shaded in dark grey are those previously known CVs which were re-discovered using the HQS selection scheme. Shown in light grey is the region in the period distribution corresponding to the period gap.

dramatically. About 62% of the known CVs contained in the high-resolution database, were recovered using the same selection criteria as for the new CVs.

Fig. 7.3 shows the orbital period distribution of all those previously known CVs, with known periods, contained in the high-resolution database of the HQS, a total of 54 systems. Displayed in dark grey are those CVs which were re-discovered using the HQS selection scheme, a total of 38 systems. Inspecting the period distribution of the positively re-identified systems, it turns out that the HQS is especially sensitive to the short period systems. This is because of their characteristic strong Balmer emission lines. Low-inclination nova-like variables, on the other hand, are the most difficult subtype of CVs to discover using our selection scheme. They are indistinguishable from hot stars at the

low-resolution of the HQS and despite their large absolute magnitudes, they are usually neither strongly variable, nor bright X-ray sources. The fact that we do not detect many short orbital period CVs (see Fig. 7.1) aggravates the problem of the "missing short periods CVs". Either there are not as many short orbital period CVs as the standard theory of CV evolution predicts or if there are, they have significantly weaker emission lines than e.g. WZ Sge or are too faint to be detected by the HQS. Deeper surveys like the Sloan Digital Sky Survey (SDSS, $V \sim 20-21$; Szkody et al. 2003) do find a larger fraction of short period CVs, but at present it is very difficult to assess the statistical relevance due to the rather serendipitous way in which they were discovered.

Fig. 7.4 shows the orbital period distribution of *a*ll CVs contained in the HQS (i.e. the previously known CVs plus the new HQS discoveries) shaded in dark grey. The orbital period distribution of the new HQS CVs is superimposed in white. Even at this stage of the project, one can recognize the defining features of the orbital period distribution of the entire present CV population (Fig. 1.5) in the new HQS CV distribution. From the period gap to the scarcity of CVs at long orbital periods ($\gtrsim$6 h) and the minimum period cutoff, the similarities between the distributions of Fig. 7.4 and that of the entire CV population are evident. Even though the number of HQS CVs with determined orbital periods is still too small to draw any solid conclusion, one may be tempted to suggest that the disagreement between the theoretically predicted sample and the observed one has its roots in the models and not in the observational bias of the current CV population. Either way we strongly need this type of studies to solve the puzzle.

7.2 ROSAT/2MASS

CVs can be detected as X-ray emitters due to large amount of potential energy released by the mass transferred from the secondary star onto the white dwarf. Magnetic CVs are

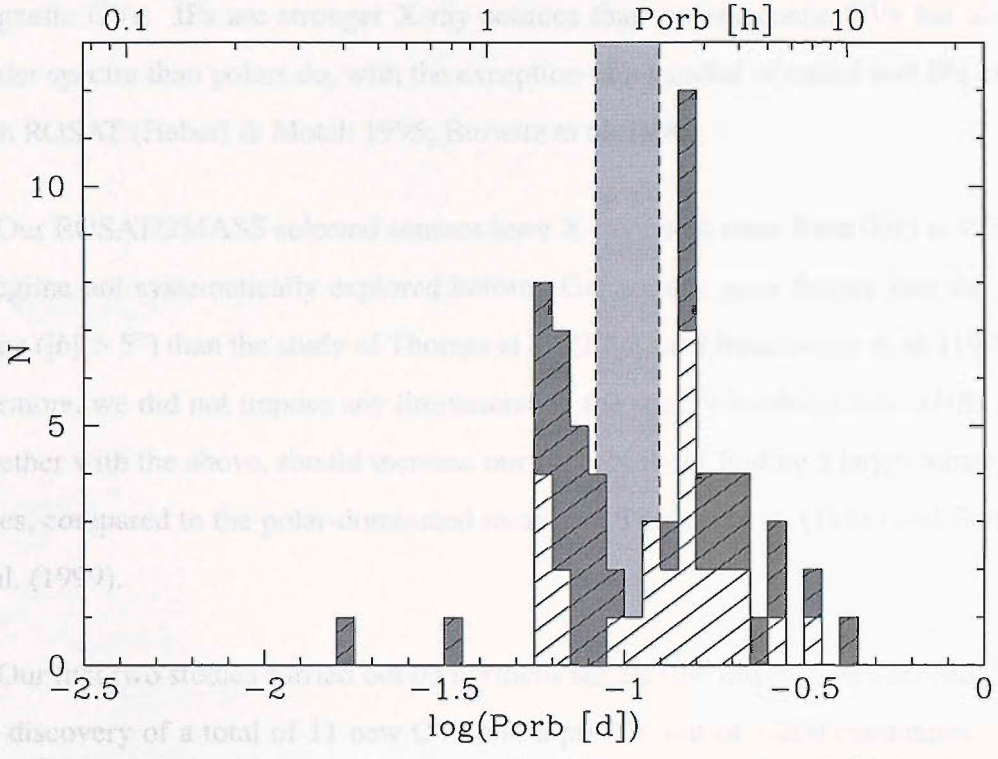

Figure 7.4: Orbital period distribution of *a*ll CVs contained in the HQS (dark grey) with the newly discovered HQS CV population plotted over it (white). Shown in light grey is the region in the period distribution corresponding to the period gap.

particularly strong X-ray sources as the bulk of the energy released is confined to a rather small volume near the magnetic polar caps of the white dwarf. As described in Sec. 2.4.2, we use 2MASS colours to establish a search criteria for CV candidates among objects contained in the ROSAT All Sky Survey.

Thomas et al. (1998) and Beuermann et al. (1999) discovered a total of 27 new CVs among their soft ($HR1 < 1$)[2], high galactic latitude ($|b| > 20°$) X-ray sources (ROSAT sources) with count rates $CR > 0.11\,\mathrm{cts\,s^{-1}}$. All 27 new CV members are magnetic CVs, the majority of which belong to the polar or AM Her class. This is not a surprising result as non-magnetic CVs are not only fainter X-ray sources but have harder spectra than

[2]The hardness ratio $HR1 = (H - S)/(H + S)$ with H and S the count rates in the hard and soft energy intervals of 0.5–2.0 ke V and 0.1–0.4 ke V, respectively

magnetic CVs. IPs are stronger X-ray sources than non-magnetic CVs but also show harder spectra than polars do, with the exception of a handful of called soft IPs identified with ROSAT (Haberl & Motch 1995; Burwitz et al. 1996).

Our ROSAT/2MASS selected sources have X-ray count rates from 0.05 to 0.2 cts s^{-1}, a regime not systematically explored before. Our sample goes deeper into the galactic plane ($|b| > 5°$) than the study of Thomas et al. (1998) and Beuermann et al. (1999). Furthermore, we did not impose any limitations on the spectra hardness ratio ($HR1$) which, together with the above, should increase our probability of finding a larger variety of CV types, compared to the polar-dominated sample of Thomas et al. (1998) and Beuermann et al. (1999).

Our first two studies carried out on northern targets (the last one very recently) lead to the discovery of a total of 11 new CVs and a pre-CV out of ~200 candidates. While a secure classification of the CVs from the ROSAT/2MASS requires additional follow-up observations, our identification spectroscopy, and in some cases also photometry, suggest that despite the much broader selection criteria compared to Beuermann et al. (1999) study, we find a large number of new magnetic CVs. Out of the 11 new CVs, 8 appear to be magnetic (5 polars and 3 IPs) and the other 3 appear to be dwarf novae. Despite the small number involved, it is interesting to note the large fraction of IPs in the ROSAT/2MASS CV sample.

So far we have obtained orbital periods for 8 of the ROSAT/2MASS CVs, of which 4 are above the period gap, one is in the gap, and 3 are below the gap. This result is no surprise compared to the current CV sample in this respect. We should however, treat this result with care as the project is still at a very early stage and there is not a sufficient number of objects to draw any conclusion from it.

Chapter 8

Conclusions

The aim of this thesis is to use observational studies to increase our understanding on how CVs and other interacting binaries evolve, from the moment they are born, to the point when they finally vanish. In practice, this means primarily finding new CVs and measuring their binary parameters, most importantly their orbital periods. The ultimate goal of such a study is to compile a statistically complete sample of CVs which could then be compared with the predictions of the current models of CV evolution. Obviously, the amount of telescope time and man-power needed to accomplish this goal is far beyond the scope of this PhD thesis. Nevertheless, the work I presented here represents a significant step on our way to an improved understanding of CV evolution. In this final chapter I summarize the major outcomes of the work presented in this thesis.

- This thesis provides an observational study of CV evolution. So far we have discovered a total of 63 new CVs using the HQS (52) and ROSAT/2MASS (11).
- Whereas HQS is highly sensitive towards the discovery of short orbital period CVs, we only discovered a very small number of new short period CVs (6). The lack of

such systems among the new HQS CVs suggests that this could be a real feature in the intrinsic galactic CV population, but we need deeper surveys to confirm it. If systems below the gap have high dispersion velocity (implying large distances) we need deeper surveys to confirm the latter hypothesis. The present HQS orbital period distribution reveals the typical features observed in previous distributions: period gap, scarcity of systems at long orbital periods and sudden cutoff at the minimum period. This strongly underlines the need to revise the current theories of CV evolution.

- So far, our ROSAT/2MASS selection scheme has helped to discovered 11 out of ~ 200 candidates, the majority of which are magnetic systems. We have obtained orbital periods for 8 of them of which 4 are above the period gap, one is in the gap, and 3 are below the gap.

- The number of SW Sex systems found in the HQS is striking, 5 out of the 28 CVs with measured orbital periods. Inspection of data from the remaining CVs (those whose orbital period is still unknown) suggest that the membership of the SW Sex stars is about to increase even more. All five new SW Sex stars have orbital periods ranging between 3.2 h to 4 h. This supports the interesting idea that the SW Sex phenomenon plays an important role in the observed dearth of dwarf novae in the period range 3–4 h and/or in CV evolution.

- The study of *FUV* data obtained with the HST/STIS of one the low states of the SW Sex stars, DW UMa, resulted in the accurate determination of its system parameters (see Tables 4.1, 4.2 and 4.3). The success of this method is likely to have a big impact towards the otherwise impossible task of reliably estimating the system parameters of the SW Sex stars. To systematically exploit the low states in other SW Sex stars we need to understand primarily what causes them and how frequently they occur.

- The follow-up observations of the newly discovered HQS IP, RX J0625, resulted in the determination of its orbital and spin periods ($P_{\rm orb} = 283.0\,$min and $P_{\rm spin} = 19.8\,$min).

- The discovery of the new HQS CV, HS 2331, whose dominant radial velocity variability (i.e. $P = 3.5\,$h) does not correspond to the orbital period of the system (i.e. $P_{\rm orb} = 81.0$), is a cause for concern about current methods for orbital period determination. HS 2331 appears to contain a pulsating white dwarf, which makes it (at the time of writing) the second confirmed pulsator among the CV population. The nature of this system is a puzzle which requires more than just data to be solved.

Bibliography

Andronov, N., Pinsonneault, M., & Sills, A. 2003, ApJ, 582, 358

Bailey, J. 1981, MNRAS, 197, 31

Balbus, S. A. & Hawley, J. F. 1991, ApJ, 376, 214

—. 1992, ApJ, 400, 610+

—. 1994, MNRAS, 266, 769

Bertin, E. & Arnouts, S. 1996, A&AS, 117, 393

Bessell, M. S. 1991, AJ, 101, 662

Bessell, M. S. & Brett, J. M. 1988, PASP, 100, 1134

Beuermann, K. 2000, New Astronomy Review, 44, 93

Beuermann, K., Baraffe, I., Kolb, U., & Weichhold, M. 1998, A&A, 339, 518

Beuermann, K., Thomas, H.-C., Reinsch, K., et al. 1999, A&A, 347, 47

Brown, T. M., Ferguson, H. C., & Davidsen, A. F. 1996, ApJ, 472, 327

Buat-Ménard, V., Hameury, J.-M., & Lasota, J.-P. 2001, A&A, 366, 612

Buat-Ménard, V., Hameury, J.-M., & Lasota, J.-P. 2001, A&A, 369, 925

Burwitz, V., Reinsch, K., Beuermann, K., & Thomas, H. C. 1996, A&A, 310, L25

Cannizzo, J. K. 1993, in Accretion disks in compact stellar objects, ed. J. Wheeler, Advanced Series in Astrophysics and Cosmology No. 9 (Singapore: World Scientific), 6–40

Cannizzo, J. K. & Wheeler, J. C. 1984, ApJ, 55, 367

Chanan, G. A., Middleditch, J., & Nelson, J. E. 1976, ApJ, 208, 512

Clemens, J. C., Reid, I. N., Gizis, J. E., & O'Brien, M. S. 1998, ApJ, 496, 352

Crawford, J. A. & Kraft, R. P. 1956, ApJ, 123, 44

Dahn, C. C., Harris, H. C., Vrba, F. J., et al. 2002, AJ, 124, 1170

de Kool, M. 1992, A&A, 261, 188

de Martino, D., Buckley, D. A. H., Mouchet, M., & Mukai, K. 1994, A&A, 284, 125

Dhillon, V., Marsh, T. R., Kelly, J., et al. 2002, in The Physics of Cataclysmic Variables and Related Objects, ed. B. T. Gänsicke, K. Beuermann, & K. Reinsch (ASP Conf. Ser. 261), 672–+

Dhillon, V. S., Jones, D. H. P., & Marsh, T. R. 1994, MNRAS, 266, 859

Downes, R. A., Webbink, R. F., Shara, M. M., et al. 2001, PASP, 113, 764

Eggleton, P. P. 1983, ApJ, 268, 368

Elias, J. H., Frogel, J. A., Matthews, K., & Neugebauer, G. 1982, AJ, 87, 1029

Filippenko, A. & Greenstein, J. L. 1984, PASP, 96, 530

Frank, J., King, A. R., & Raine, D. J. 1992, Accretion power in astrophysics (Cambridge: Cambridge University Press)

Gänsicke, B. T., Szkody, P., de Martino, D., et al. 2003, ApJ, 594, 443

Gänsicke, B. T. 2000, Reviews of Modern Astronomy, 13, 151

Gänsicke, B. T., Beuermann, K., & Reinsch, K., eds. 2002a, The Physics of Cataclysmic Variables and Related Objects (ASP Conf. Ser. 261)

Gänsicke, B. T., Beuermann, K., & Thomas, H. C. 1997, MNRAS, 289, 388

Gänsicke, B. T., Fried, R. E., Hagen, H.-J., et al. 2000, A&A, 356, L79

Gänsicke, B. T., Hagen, H. J., & Engels, D. 2002b, in The Physics of Cataclysmic Variables and Related Objects, ed. B. T. Gänsicke, K. Beuermann, & K. Reinsch (ASP Conf. Ser. 261), 190–199

Gänsicke, B. T., Hagen, H. J., Kube, J., et al. 2002c, in The Physics of Cataclysmic Variables and Related Objects, ed. B. T. Gänsicke, K. Beuermann, & K. Reinsch (ASP Conf. Ser. 261), 623–624

Green, R. F., Ferguson, D. H., Liebert, J., & Schmidt, M. 1982, PASP, 94, 560

Haberl, F. & Motch, C. 1995, A&A, 297, L37+

Hagen, H.-J., Engels, D., & Reimers, D. 1999, A&AS, 134, 483

Hagen, H. J., Groote, D., Engels, D., & Reimers, D. 1995, A&AS, 111, 195

Hameury, J. M., King, A. R., & Lasota, J. P. 1989, MNRAS, 237, 39

Harrop-Allin, M. K. & Warner, B. 1996, MNRAS, 279, 219

Hellier, C. 2001, Cataclysmic variable stars: how and why they vary. (Chichester, UK: Springer-Praxis)

Hellier, C., Mason, K. O., Smale, A. P., et al. 1989, MNRAS, 238, 1107

Hellier, C., Wynn, G. A., & Buckley, D. A. H. 2002, MNRAS, 333, 84

Hessman, F. V. 2000, New Astronomy Review, 44, 155

Hessman, F. V., Gänsicke, B. T., & Mattei, J. A. 2000, A&A, 361, 952

Hoard, D. W., Wachter, S., Clark, L. L., & Bowers, T. P. 2002, ApJ, 565, 511

Horne, K. 1986, PASP, 98, 609

Horne, K. & Marsh, T. R. 1986, MNRAS, 218, 761

Howell, S. B., Nelson, L. A., & Rappaport, S. 2001, ApJ, 550, 897

Howell, S. B., Rappaport, S., & Politano, M. 1997, MNRAS, 287, 929

Hubeny, I. 1988, Comput.,Phys.,Comm., 52, 103

Hubeny, I. & Lanz, T. 1995, ApJ, 439, 875

Hynes, R. I., Charles, P. A., Haswell, C. A., et al. 2001, MNRAS, 324, 180

Iben, I. J. & Livio, M. 1993, PASP, 105, 1373

Jordan, S. 1997, in White Dwarfs, ed. J. Isern, M. Hernanz, & E. García-Berro (Dordrecht: Kluwer), 397–403

King, A. R. 1988, QJRAS, 29, 1

—. 2000, New Astronomy Review, 44, 167

King, A. R. & Cannizzo, J. K. 1998, ApJ, 499, 348

King, A. R., Frank, J., Kolb, U., & Ritter, H. 1995, ApJ Lett., 444, L37

King, A. R. & Kolb, U. 1995, ApJ, 439, 330

King, A. R. & Schenker, K. 2002, in The Physics of Cataclysmic Variables and Related Objects, ed. B. T. Gänsicke, K. Beuermann, & K. Reinsch (ASP Conf. Ser. 261), 233–241

Kirkpatrick, J. D., Reid, I. N., Liebert, J., et al. 1999, ApJ, 519, 802

—. 2000, AJ, 120, 447

Knigge, C., Long, K. S., Blair, W. P., & Wade, R. A. 1997, ApJ, 476, 291

Knigge, C., Long, K. S., Hoard, D. W., Szkody, P., & Dhillon, V. S. 2000, ApJ Lett., 539, L49

Kolb, U. 1993, A&A, 271, 149

Kolb, U. & Baraffe, I. 1999, MNRAS, 309, 1034

Kolb, U., King, A. R., & Ritter, H. 1998, MNRAS, 298, L29

Kolb, U., Rappaport, S., Schenker, K., & Howell, S. 2001, ApJ, 563, 958

Kolb, U. & Ritter, H. 1992, A&A, 254, 213

Kolb, U. & Stehle, R. 1996, MNRAS, 282, 1454

Kopal, Z. 1959, Close binary systems (The International Astrophysics Series, London: Chapman & Hall, 1959)

Kotak, R., van Kerkwijk, M. H., & Clemens, J. C. 2002, A&A, 388, 219

Kraft, R. P., Mathews, J., & Greenstein, J. L. 1962, ApJ, 136, 312

Krzeminski, W. & Kraft, R. P. 1964, ApJ, 140, 921

Kube, J., Gänsicke, B., & Hoffmann, B. 2002, in The Physics of Cataclysmic Variables and Related Objects, ed. B. T. Gänsicke, K. Beuermann, & K. Reinsch (ASP Conf. Ser. 261), 678–679

Kutter, G. S. & Sparks, W. M. 1980, ApJ, 239, 988

Lasota, J.-P. 2001, New Astronomy Review, 45, 449

Leggett, S. K. 1992, ApJS, 82, 351

Lin, D. N. C., Faulkner, J., & Papaloizou, J. 1985, MNRAS, 212, 105

Livio, M. 1982, A&A, 112, 190

Livio, M. & Pringle, J. E. 1994, ApJ, 427, 956

Livio, M. & Soker, N. 1988, ApJ, 329, 764

Long, C. 2000, STIS Time-Tag Timing (STIS Technical White Paper 00-175; Baltimore: STScI)

Ludwig, K., Meyer-Hofmeister, E., & Ritter, H. 1994, A&A, 290, 473

Marsh, T. R. 1989, PASP, 101, 1032

Marsh, T. R. & Dhillon, V. S. 1997, MNRAS, 292, 385

Mauche, C. W., Lee, Y. P., & Kallman, T. R. 1997, ApJ, 477, 832

McDermott, P. N. & Taam, R. E. 1989, ApJ, 342, 1019

Meyer, F. & Meyer-Hofmeister, E. 1979, A&A, 78, 167

—. 1981, A&A, 104, L10

—. 1983, A&A, 121, 29

—. 1984, A&A, 132, 143

Nogami, D., Engels, D., Gänsicke, B. T., et al. 2000, A&A, 364, 701

Oke, J. B. 1990, AJ, 99, 1621

Osaki, Y. 1974, PASJ, 26, 429

—. 1996, PASP, 108, 39

Paczynski, B. 1965, Acta Astronomica, 15, 89

—. 1981, Acta Astronomica, 31, 1

Paczynski, B. & Sienkiewicz, R. 1981, ApJ Lett., 248, L27

—. 1983, ApJ, 268, 825

Panei, J. A., Althaus, L. G., & Benvenuto, O. G. 2000, A&A, 353, 970

Patterson, J. 1984, ApJS, 54, 443

—. 1994, PASP, 106, 209

—. 1998, PASP, 110, 1132

Patterson, J., Richman, H., Kemp, J., & Mukai, K. 1998, PASP, 110, 403

Pinsonneault, M. H., Andronov, N., & Sills, A. 2002, in The Physics of Cataclysmic Variables and Related Objects, ed. B. T. Gänsicke, K. Beuermann, & K. Reinsch (ASP Conf. Ser. 261), 208–216

Plavec, M. & Kratochvil, P. 1964, Bulletin of the Astronomical Institutes of Czechoslovakia, 15, 165

Politano, M. 1996, ApJ, 465, 338

Pratt, G. W., Hassall, B. J. M., Naylor, T., & Wood, J. H. 1999, MNRAS, 307, 413

Prialnik, D. & Kovetz, A. 1995, ApJ, 445, 789

Prialnik, D., Livio, M., Shaviv, G., & Kovetz, A. 1982, ApJ, 257, 312

Prialnik, D. & Shara, M. M. 1986, ApJ, 311, 172

Pringle, J. E. & Wade, R. A., eds. 1985, Interacting binary stars

Rappaport, S., Joss, P. C., & Verbunt, F. 1983, ApJ, 275, 713

Rappaport, S., Joss, P. C., & Webbink, R. F. 1982, ApJ, 254, 616

Ringwald, F. A. 1996, in Cataclysmic Variables and Related Objects, ed. A. Evans & J. H. Wood, IAU Coll. No. 158 (Dordrecht: Kluwer), 89–92

Ritter, H. 1985, A&A, 145, 227

Ritter, H. & Kolb, U. 2003, VizieR Online Data Catalog, 5113, 0

Rodríguez-Gil, P., Casares, J., Martínez-Pais, I. G., Hakala, P., & Steeghs, D. 2001, ApJ Lett., 548, L49

Rutten, R. G. M. & Dhillon, V. S. 1994, A&A, 288, 773

Scargle, J. D. 1982, ApJ, 263, 835

Schenker, K. & King, A. R. 2002, in The Physics of Cataclysmic Variables and Related Objects, ed. B. T. Gänsicke, K. Beuermann, & K. Reinsch (ASP Conf. Ser. 261), 242–251

Schenker, K., King, A. R., Kolb, U., Wynn, G. A., & Zhang, Z. 2002, MNRAS, 337, 1105

Schenker, K., Kolb, U., & Ritter, H. 1998, MNRAS, 297, 633

Schneider, D. P. & Young, P. 1980, ApJ, 238, 946

Schreiber, M. R. & Gänsicke, B. T. 2003, A&A, 406, 305

Schreiber, M. R., Gänsicke, B. T., & Cannizzo, J. 2000, A&A, 362, 268

Schreiber, M. R., Gänsicke, B. T., & Mattei, J. A. 2002, A&A, 384, L6

Schwarzenberg-Czerny, A. 1989, MNRAS, 241, 153

Shafter, A. W. 1983, ApJ, 267, 222

—. 1992, ApJ, 394, 268

Shafter, A. W., Hessman, F. V., & Zhang, E.-H. 1988, ApJ, 327, 248

Shakura, N. I. & Sunyaev, R. A. 1973, A&A, 24, 337

Shara, M. M. 1989, PASP, 101, 5

Shara, M. M., Livio, M., Moffat, A. F. J., & Orio, M. 1986, ApJ, 311, 163

Shaviv, G. 1987, Ap&SS, 130, 303

Shaviv, G. & Starrfield, S. 1987, ApJ Lett., 321, L51

Sills, A., Pinsonneault, M. H., & Terndrup, D. M. 2000, ApJ, 534, 335

Sion, E. M. 1999, PASP, 111, 532

Smak, J. 1983, ApJ, 272, 234

—. 2000, New Astronomy Review, 44, 171

Smith, D. A. & Dhillon, V. S. 1998, MNRAS, 301, 767

Smith, D. A., Dhillon, V. S., & Marsh, T. R. 1998, MNRAS, 296, 465

—. 2002, MNRAS, submitted

Soker, N., Livio, M., & Harpaz, A. 1984, MNRAS, 210, 189

Spruit, H. C. & Ritter, H. 1983, A&A, 124, 267

Spruit, H. C. & Taam, R. E. 2001, ApJ, 548, 900

Starrfield, S., Sparks, W. M., & Truran, J. W. 1985, ApJ, 291, 136

Stellingwerf, R. F. 1978, ApJ, 224, 953

Stepanian, J. A., Chavushyan, V. H., Carrasco, L., Tovmassian, H. M., & Erastova, L. K. 1999, PASP, 111, 1099

Szkody, P., Anderson, S. F., Agüeros, M., et al. 2002, AJ, 123, 430

Szkody, P., Fraser, O., Silvestri, N., et al. 2003, AJ, 126, 1499

Taam, R. E. & Bodenheimer, P. 1989, ApJ, 337, 849

Taam, R. E. & Spruit, H. C. 1989, ApJ, 345, 972

Taylor, C. J., Thorstensen, J. R., & Patterson, J. 1999, PASP, 111, 184

Thomas, H. C., Beuermann, K., Reinsch, K., et al. 1998, A&A, 335, 467

Thorstensen, J. R., Ringwald, F. A., Wade, R. A., Schmidt, G. D., & Norsworthy, J. E. 1991, AJ, 102, 272

Thorstensen, J. R., Taylor, C. J., & Kemp, J. 1998, PASP, 110, 1405

van Paradijs, J., Augusteijn, T., & Stehle, R. 1996, A&A, 312, 93

van Zyl, L., Warner, B., O'Donoghue, D., et al. 2000, Baltic Astronomy, 9, 231

Verbunt, F. & Zwaan, C. 1981, A&A, 100, L7

Warner, B. 1986, MNRAS, 219, 347

—. 1987, MNRAS, 227, 23

—. 1995, Cataclysmic Variable Stars (Cambridge: Cambridge University Press)

Webbink, R. F. 1985, Interacting Binary Stars, ed. J. E. Pringle & R. A. Wade (Cambridge: Cambridge University Press), 39

Wei, J. Y., Xu, D. W., Dong, X. Y., & Hu, J. Y. 1999, A&AS, 139, 575

Wickramasinghe, D. T. & Ferrario, L. 2000, PASP, 112, 873

Wielen, R., Dettbarn, C., Fuchs, B., Jahreiß, H., & Radons, G. 1992, in IAU Symp. 149: The Stellar Populations of Galaxies, 81–92

Wood, J. H., Irwin, M. J., & Pringle, J. E. 1985, MNRAS, 214, 475